Politecnico di Torino

Corso di Laurea Magistrale in Ingegneria Energetica e Nucleare

EMC3-EIRENE simulations of the ASDEX-Upgrade tokamak in support of experiments with a toroidally localised liquid Sn module

Relatore:
Prof. Fabio SUBBA

Candidato:
Alessandro Costa

Corelatori:
Ing. Giuseppe Francesco NALLO

Anno accademico 2023/2024

Abstract

Nuclear fusion is the fundamental nuclear reaction that powers stars, and it is currently being considered as a potential method for energy production. Harnessing nuclear fusion poses a global challenge due to the difficulty of replicating the ideal conditions for these reactions on Earth. These conditions are partially reproduced inside machines called Tokamaks through the use of a localized magnetic system, where the fusion fuel (plasma heated to approximately 100 million degrees Kelvin) is magnetically confined.

The power production levels achieved in the confined area, combined with the limited surface area of the Plasma Facing Components (PFCs), make managing the thermal load on the wall very challenging, threatening the integrity of the materials used. This phenomenon is referred to as the power exhaust problem and is one of the fundamental challenges in designing a future fusion reactor. The primary component for the power exhaust problem is the divertor, a solid-state component commonly located at the bottom of the plasma chamber. It is specifically designed to handle the flow of particles and thermal energy ejected from the confined plasma and to maintain the structure's integrity, as well as managing impurities generated by the interactions between incoming particles and PFCs.

The complexity of this system necessitates plasma simulations, a powerful tool not only useful in the absence of diagnostics but also for interpreting experimental results, as well as for conducting predictive optimization for the experiments aimed at future applications. This thesis, in particular, focuses on simulating the behavior of plasma in pure deuterium within the ASDEX Upgrade (AUG) experimental reactor, aiming to establish a foundation for future studies incorporating impurities. For this goal, the 3D modeling system EMC3-EIRENE was utilized, integrating EMC3 (fluid model) for describing plasma transport and EIRENE (kinetic model) for describing neutral transport processes, providing enhanced localized phenomena representation, with an accurate 3D description of charge and neutral particles behaviour. To structure the simulation, it was necessary to supplement experimental data obtained from the IPP database (Max Planck Institute for Plasma Physics, Garching, Germany), responsible for the data collection of experiments conducted by AUG, with data from similar case study simulations.

The thesis was thus conceived as a foundational study for future 3D simulations that will include impurities, especially in case studies where alternative divertor configurations are proposed. A potential application for this study is the simulation of a scenario in which a self-healing liquid metal divertor (LMD) module is localized in a well-defined toroidal position of the ASDEX machine. This concept is driven by the anticipated need to manage increased thermal loads in upcoming reactors like EU-DEMO. The interaction between the plasma and the surface of this model generates a protective cloud of evaporated particles above the divertor, aiding in the dissipation of transmitted power through radiation emission. Such a configuration would result in an asymmetric characterization of the system, making 3D EMC3-EIRENE modeling the most suitable approach for representing localized phenomena.

The results of the pure deuterium simulation coincide with the theoretical expectations, with lower plasma density and temperature near the divertor compared to the central region.

Contents

1 Introduction on Fusion Energy

In recent years, the problem of energy supply has become increasingly important in the global geopolitical panorama. The continuous increase in population and the need to increase personal well-being forces the system to continuously exploit resources, which leads to an unbridled emission of polluting materials, contrasting the required sustainability objectives. The production of energy from nuclear sources appears to be a fundamental player for a coherent and realistic ecological transition path, finding its maximum expression at an industrial level in nuclear fission. The reactors are based on the exploitation of nuclear reactions, guaranteeing an enormous release of energy, in the form of kinetic energy of the reaction products. The main consequence is the subsequent heating of the surrounding environment: the heat is transmitted by a cooling fluid to the thermal cycle, which reaches the turbine and allows the production of electricity. The main reactions so far investigated and exploited to produce energy are nuclear fission and fusion, which can be summarized in a generic way according to the formulation:

$$r_1 + r_2 \rightarrow p_1 + p_2 + n \cdot \nu + Q \tag{1}$$

Equation 1: General nuclear reaction

With r_1 and r_2 the reactants, p_1 and p_2 the products, ν the generic particle involved, different according to the reaction. Q is the mass difference between products and reactants and defined as:

$$Q = (E_{B.p1} + E_{B.p2}) - (E_{B.r1} + E_{B.r2}) \tag{2}$$

$$E_B = (M_{components} - M_{nucleus}) \cdot c^2 \qquad c = speed\,of\,light \tag{3}$$

Equation 3: Mass difference & Binding energy formulation

The term E_B is called *Nuclear Binding Energy*, defined as the energy required to separate an atomic nucleus completely into its constituent protons and neutrons, or, equivalently, the energy that would be liberated by combining individual protons and neutrons into a single nucleus. According to this principle, it's possible to define the mass of components as:

$$M_{components} = Z \cdot m_{prot.} + (A - Z) \cdot m_{neutr.} \tag{4}$$

Equation 4: Mass definition

In Fig(1) is reported the binding energy curve as a function of the number of nucleons into the nucleus:

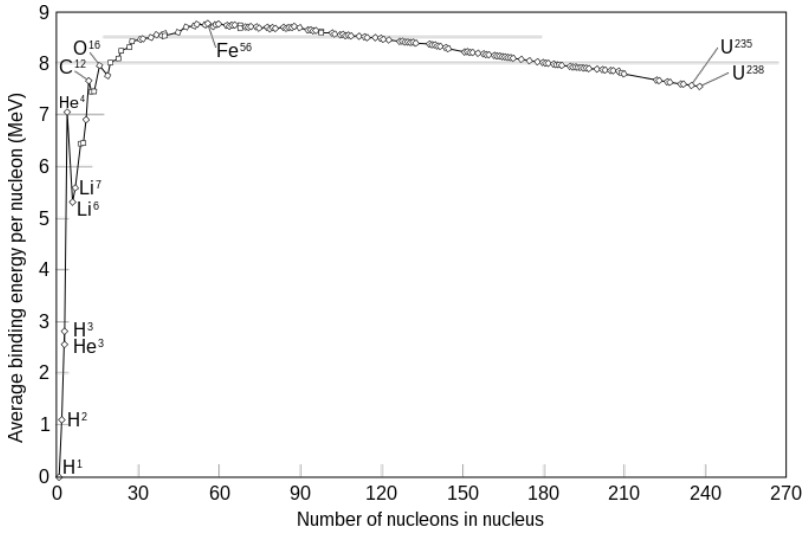

Figure 1: Average binding energy per nucleon [MeV] against number of nucleons in nucleus

1.1 Reaction rates for different thermonuclear fusion reactions

Thermonuclear fusion reactions require the presence of plasma, i.e. an ionized gas consisting of a set of ions and electrons in which the total charge is neutral and the temperature is kept to 15KeV (around 100 million degrees).
Fusion reactions are associated with the left branch of the curve presented in Fig.(1), where the atomic species involved have a small atomic mass and the reference interaction involves the collision between two light atoms and subsequent release of energy (exothermic reaction). Following this logic, the fusion reactions are multiple and differ according to the nature of the constituent elements of the plasma and the probability that the reaction can be triggered at different conditions.

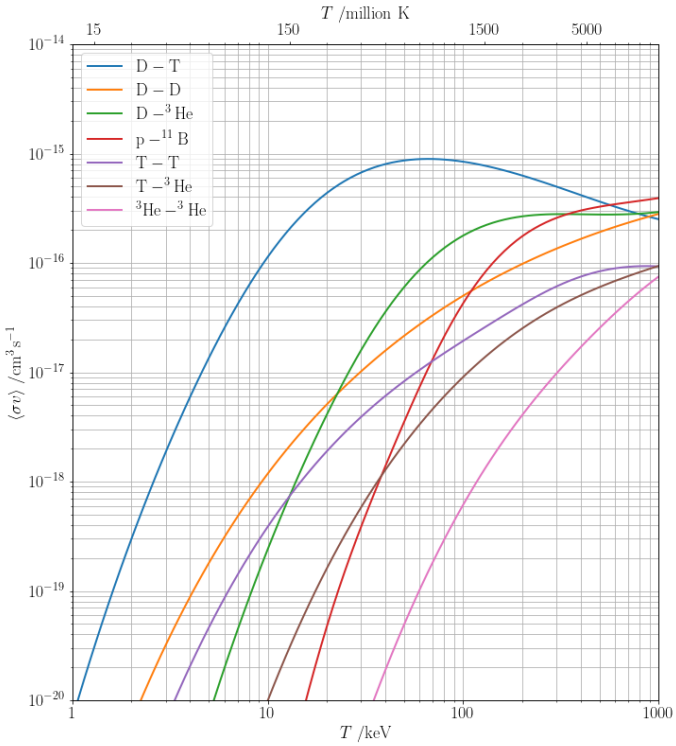

Figure 2: Average reaction rate based on temperature.

σ is called cross-section and measures the probability for the reaction to occur as a function of the collision energy, given by the relative velocities of the two nuclei. Before the collision, the colliding particles move with a distribution of relative velocities $f(v)$. The average reaction rate can be calculated as:

$$< \sigma v >= \int_0^\infty \sigma(v) v f(v) dv \tag{5}$$

Equation 5: Average reaction rate formulation

If the plasma is thermalized, the distribution can present a Gaussian or a Maxwell-Boltzmann distribution. Considering the latter configuration, the reference for $f(v)$ can be:

$$f(v) = f_{MB}(v) = 4\pi v^2 \left(\frac{\mu}{2\pi k_B T}\right)^{3/2} exp\left(-\frac{\mu v^2}{2k_B T}\right) \qquad \mu = \frac{m_1 m_2}{m_1 + m_2} \tag{6}$$

Equation 6: Maxwell-Boltzmann distribution

Fig(2) outlines the average reaction rates $< \sigma v >$ for each type of fusion reaction based on temperature, showing that D-T is the most favorable of all, with the fusion cross section at the relevant plasma temperature larger than the other possible reactions. It consists in the collision between the deuterium and tritium atoms giving rise to one α particle, one free neutrons and 17.6MeV of energy:

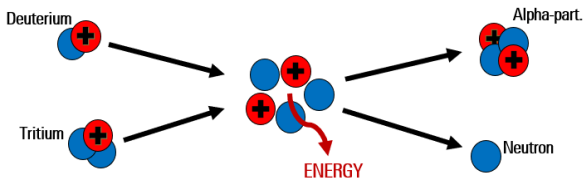

Figure 3: Deuterium-Tritium reaction.

$$ {}^{2}_{1}H + {}^{3}_{1}H \rightarrow \alpha + (n + 14.1MeV) + ({}^{4}_{2}He + 3.5MeV) \tag{7} $$

Equation 7: Deuterium-Tritium reaction

From the reaction rate it is possible to calculate the volumetric fusion power P_{fus} as:

$$ P_{fus} = n_D n_T < \sigma v_{D,T} > E_{fus} \quad [W/m^3] \tag{8} $$

Equation 8: Fusion power equation

With n_D and n_T the densities of the species D and T into the plasma chamber. $E_{fus} = 17.6MeV$ is the energy liberated per D-T reaction.

1.2 Characteristics of plasmas and Lawson Criterion

The ideal plasma consists of a 50-50 mixture of deuterium and tritium ions - no impurities and ashes considered - bathed in equal amounts of free electrons. It follows that the total density of the mixture consists of the sum of the respective densities of the free charges present and can be evaluated as: $n_{tot} = n_e + n_D + n_T$, whith the assumption $n_T = n_D = n_e/2$ and a value of the order of magnitude around $n \approx 10^{20} m^{-3}$. For the sake of simplicity, the following nomenclature will be used: $n = n_e = n_i$, with $n_i = n_D + n_T$. As defined in Eq(8), the plasma can contain impurities such as α particles or materials derived from erosion by interaction between the plasma and the containment walls of the chamber, which tend to dilute the fuel concentration in the reference volume. Furthermore, α particles and neutrons constitute important energy channels for the maintenance of the reaction and for a possible energy production: The total energy is divided among the products of the reaction, as well as the power produced.
The neutron component E_n is related to neutron kinetics and is the major contributor,

$$E_{fus} = E_\alpha + E_n \quad E_\alpha \approx 3.5MeV, \quad E_n \approx 14.1MeV \tag{9}$$

$$P_{fus} = P_\alpha + P_n \tag{10}$$

Equation 10: Energy and Power balance

accounting for about 80% of the total fusion energy. Since the charge is neutral, its trajectory is not influenced by magnetic fields, therefore the neutrons tend to propagate until they reach the *First Wall*, where they deposit their kinetic energy and increase its temperature. Through a cooling circuit the heat is then extracted and the heated fluid is directed towards a turbine to produce energy.
The α component consists of the remaining 20% of the total energy, it will be used to maintain the ideal thermal conditions for fusion reactions to take place since the energy related E_α is very high compared to the background plasma (15 keV). Hence the α energy needs to be transferred to the plasma in order to sustain the plasma against thermal conduction (losses). Given the high temperatures, the plasma must be confined within a defined volume. The presence of the plasma and its state of confinement depends on the energy balance between the power loss and the internal energy content supplied to reach the ideal temperatures, this relationship is defined by the *Energy confinement time*:

$$\tau_E = \frac{E_{int.}}{P_{Loss}} \tag{11}$$

Equation 11: Energy confinement time

Thermal energy must be added at the same rate the plasma loses energy in order to maintain the fusion conditions. This energy can be supplied by the fusion reactions themselves, depending on the reaction type, or by supplying additional heating through a variety of methods. it is clear that this ratio indicates the speed with which the system loses its energy: the greater the power losses, the lower τ_E and therefore the confinement period of the plasma. Supposing the plasma matter as a perfect gas, the (ionic or electronic) pressure p and internal energy density E_{int} stored in each m^3 are defined as:

$$E_{int} = \frac{3nkT}{2} \tag{12}$$

$$p = nkT \tag{13}$$

Equation 13: Internal energy and Plasma pressure

Whith E_{int} and p both depending by the density n and the plasma temperature T, k_B the Boltzmann constant.
In order to guarantee a plasma condition as close as possible to the stationary one, the plasma temperature must be kept constant, therefore the net energy balance between sources and losses must be zero:
With η defined as efficiency: it expresses the ability of the machine to raise energy from

$$P_{net} = \eta \cdot (P_{gen} - Losses) \simeq 0 \tag{14}$$

Equation 14: Basic plasma energy balance formulation

fusion reactions and depends on its construction characteristics. $P_{gen.}$ is the rate of power generated from fusion reactions collected into the plasma. With the term *Losses* means that part of power lost through the radiative channel $P_{loss.rad.}$ and the transport of particles away from the core $P_{loss.conduct.}$.
Following what explained with the Eq.(11), Eq.(12), and assuming:

- Principle of quasi-neutrality $n_e \simeq n_i$;
- Total absence of impurities;
- All species at the same temperature;
- 50-50 mixture of D and T;

It is possible to prove the *Lawson criteria*, according to which net power between produced and lost energy must be above a defined limit to ensure ignition and self-sustainability [4]. Considering this principle and basing on the observations made at the beginning of the chapter it is possible to define the energy balance in Eq.(14) as:

$$P_{heating} = n_D n_T < \sigma v_{D,T} > E_\alpha = \frac{n^2}{4} < \sigma v_{D,T} > E_\alpha \tag{15}$$

Equation 15: Heating power

$$P_{loss} = \frac{3nT}{\tau_E} \tag{16}$$

Equation 16: Power losses as function of τ_E

Combining Eq.(15) and Eq.(16) with the energy balance of Eq.(14) will be:

$$n\tau_E \geq \frac{12T}{E_\alpha < \sigma v_{D,T} >}$$

Rearranging the equation, the combination of n, T and τ_E is called *triple product*:

$$nT\tau_E \geq \frac{12T^2}{E_\alpha < \sigma v_{D,T} >} \tag{17}$$

Equation 17: Lawson criterion formulation

1.3 Tokamak Configuration - Powerexhaust Problem

Since plasma is a state of matter in which the internal energy of the gas is very high, atoms commonly occur in an ionized state, where ions and electrons roam freely and independently of each other. This condition implies that charged particles can be influenced by a directed magnetic field, changing their trajectory of motion. this concept constitutes the cardinal principle for the confinement of the plasma in a future reactor and is called *Magnetic Confinement*. Therefore the plasma is confined within a toroidal-shaped volume by a system of suitably directed and intertwined magnetic fields, so as to keep the plasma column away from the first layer of the protective walls.
This configuration is called *Tokamak*, a Russian acronym of **Toroidal'naya kamera s magnitnymi katushkami** and means toroidal chamber with magnetic coils.
Magnetic confinement fields are generated by a system of superconducting magnets, maintained at low temperatures by a cooling circuit, where the fluid is kept around 4.5 degrees Kelvin. The magnetic field generation system stays around the plasma vacuum vessel and is divided according to where the magnets are positioned:

- Central solenoid (CS): it works at varying current condition, from which a variable magnetic field is generated. Fuel particles are accelerated by the variable magnetic field, increasing the probability of collision with each other (ohmic heating). Moreover, the time dependence of the generated magnetic field gives rise to the plasma current I_P, the period of discharge depends strictly by the capability of the CS to maintain this current during the burn time;

- Toroidal field coils (TF): they works at constant current condition and generate a toroidal current. These magnets do not occur continuously but are arranged in a discrete configuration along the toroidal direction, individually assuming a characteristic D-shape;

- Poloidal field coils (PF): they works at varying current condition and shape the plasma properly to assume a good configuration, improving the stability. These magnets assume a ring shape and are situated outside of the toroidal field magnet structure;

The superposition of these magnetic fields gives an helical shape of the total magnetic field lines, which keep the plasma confined. The temporal variability of the magnetic fields does not allow the system to maintain a constant configuration, the reactor therefore works in a pulsed manner and the plasma manifests itself every time the *discharge* induced by the magnetic fields takes place. Therefore, the period of existence of the plasma strictly depends on how long the discharge lasts. The figure Fig.(4) shows the configuration of the magnetic fields relating to the Tokamak.

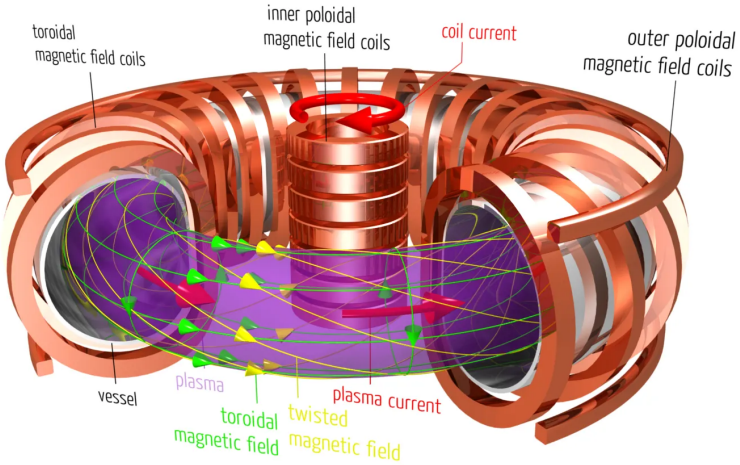

Figure 4: Tokamak prototype - magnetic field configuration

The components in direct contact with the plasma are defined as *Plasma Facing Components* (PFCs) and are used both to check the state of the plasma and to shield the background operating and monitoring systems (including coils) from neutron flux and excessively high temperatures, preserving their integrity. The PFCs are organized in modules, which allows to increase the maintainability, replacing each module when damages occur. The most important PFCs are:

- Blanket: in addition to protect the steel structure and the other systems from heat and stray neutrons, it converts the kinetic energy of neutrons - deposited at each collision with the blanket lattice - into thermal energy. Thermal energy will be extracted from a complex cooling loop, directed to a turbine built for power generation. In future, this component will assume the *Breeding Blanket* configuration, allowing to produce tritium starting by the Lithium in the structure and the neutrons from the core. The blanket covers about 80% of the plasma chamber, excluding the portion at the bottom. There are many possible configurations for the blanket, but the common idea for the constituent materials is to use beryllium as the surface material, arranged in tiles around the plasma chamber, followed by layers of breeding material and cooling loops;

- Divertor: extracts heat from the incoming particles and manages ashes produced by fusion reactions, keeps the plasma pure by eliminating - with the help of localized pumping systems - excessive quantities of α-particles and particles eroded by PFCs. It covers the lower part of the plasma chamber, about 20% of the total. The divertor is the key component for controlling the quality and energy transferred between different areas of the plasma. Usually it is made by a surface layer of tungsten tiles, followed by a high heat transfer material (Heat sink material) and the cooling pipes, ending with a steel structure;

The management of thermal loads and contact with stray particles are some of the main problems that PFCs have to face. Fig.(5) shows a summary diagram to give an idea of the proportions of the machine and the positions of the components.

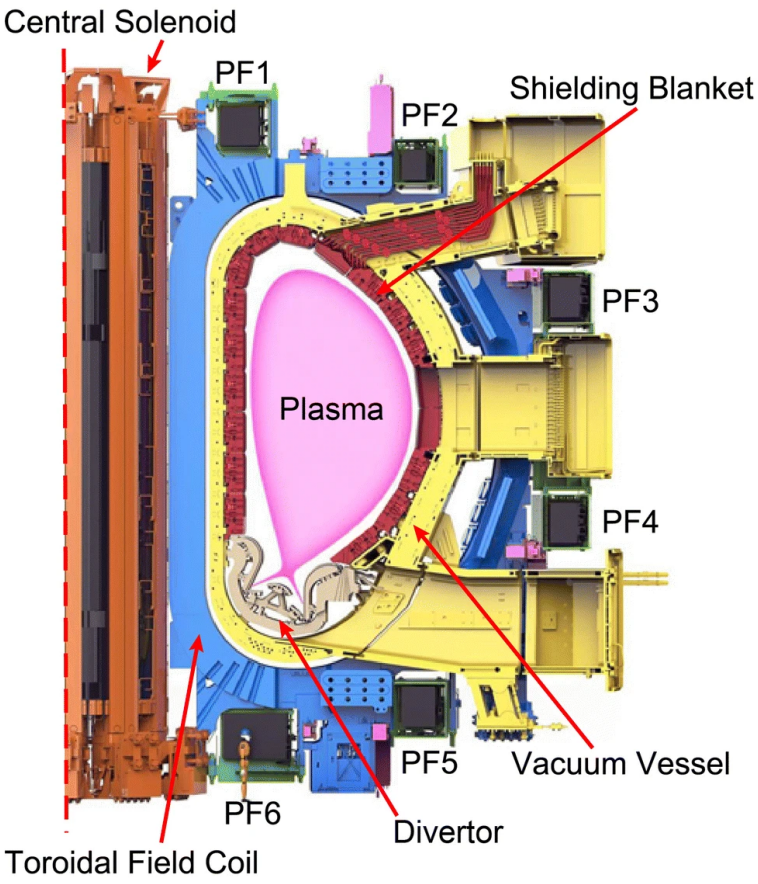

Figure 5: Tokamak section - PFCs and Magnets configuration

2 Problem description: Plasma-Divertor Dynamics and ASDEX Upgrade Overview

Given the shape of the structure and the size of the total magnetic field, some field lines are not closed but remain open and directed towards well-defined areas of the PFCs. In particular, the structure of the field lines is studied in such a way that the open lines tend to converge towards the divertor plates, so as to be able to direct the transport of charged particles exactly where expected.

2.1 Definition of the Different Plasma Regions and Power Balancing

The plasma is divided into two main macro regions, which are the core and the SOL: the *Core* is the largest region and where most of the fusion reactions take place. This region is characterized by a massive presence of closed magnetic surfaces that strongly limit the transport of charged particles across the field lines, developing strong radial gradients. In this region the most important transport phenomena occur along the closed lines - approximable as isolines - where the gradients are very small and physical conditions hardly change at all. Charged particles can escape from the core through collisions with other particles and enter the *Scrape-Off Layer* (SOL), i.e. a thin region delimited by the last closed magnetic surface called (*Separatrix*). The ions and electrons traveling in this region mostly follow the imposed direction along the open field lines, reaching the divertor. Transport in the Scrape-Off Layer exhibits distinct characteristics compared to transport in the confined plasma region. This difference arises from the presence of open field lines in the SOL. Due to the high collisionality in this region, the influence of neo-classical effects becomes negligible. As a result, charged particles primarily follow the direction of the magnetic field B, leading to a significant predominance of parallel transport over radial transport. Specifically, the parallel velocity component $v_{\parallel}$ is much larger, typically on the order of 10^4, compared to the perpendicular velocity component $v_{\perp}$ ($\simeq 1m/s$).
This discrepancy in velocities helps explain the substantial disparity between the radial and poloidal dimensions of the SOL. The *Strike-Point* will turn out to be an area with a high deposition of particles and therefore with a high thermal load. Hence, the heat and particle loads depends strongly by the dependence of the charged particles wondering around the magnetic lines next to the Separatrix.

This profile of magnetic surfaces is formed by adding a coil under the toroidal structure, in this way the *X-point* is created in the poloidal section. This configuration is called *Single Null Configuration* and represents the reference scheme for the magnetic confinement of this type of machine. Many variants of this idea have been proposed in the years to come with the aim of decreasing the thermal loads to which the divertor is subjected: by increasing the wetted area, the number of strike points or introducing an additional layer of different material. Neutral particles, on the other hand, unless they are ionized in the plasma, tend to disperse isotropically and reach the blanket.
Concluding, the SOL is separated from the core by the separatrix, in this region the diffusion is stronger along the direction parallel to the field lines than the radial one. Strong gradients

develop along the SOL direction and velocities along parallel direction reach the sound speed, vastly higher than in radial direction.
In Fig.(6) the configuration relating to the magnetic fields and the subdivision of the plasma portions is shown.

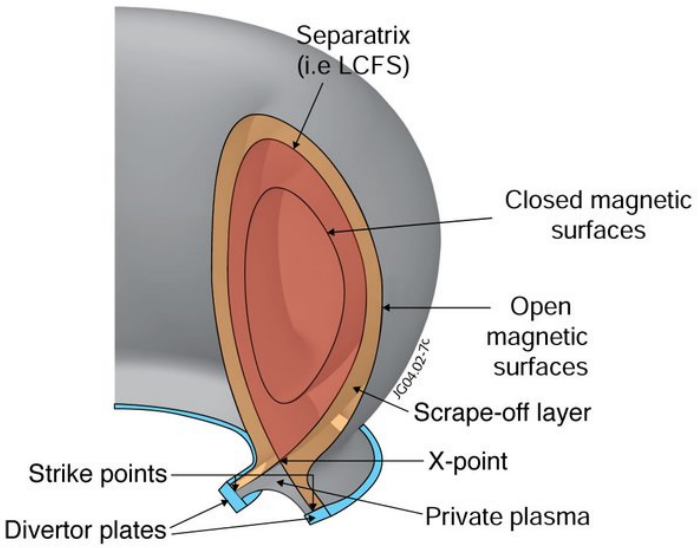

Figure 6: Tokamak section - Magnetic filed lines configuration

In Eq.(18) is reported the *Power width* formulation proposed by R.J.Goldston in [8], this parameter it's useful to calculate the power deposited on the divertor target along the radial direction, according to the decreasing exponential law expressed in Eq.(19):

$$\lambda_q = 5671 \cdot P_{SOL}^{1/8} \frac{(1+\kappa^2)^{5/8} a^{17/8} B^{1/4}}{I_P^{9/8} R} \left(\frac{2\overline{A}}{\overline{Z}^2 (1+\overline{Z})} \right)^{7/16} \left(\frac{Z_{eff}+4}{5} \right)^{1/8} \tag{18}$$

Equation 18: Power width - Goldston formulation

With a the minus radius, R the major radius, I_P the plasma current, P_{SOL} the power entering into the SOL from the core, B the resulting magnetic field, $\overline{A}$ and $\overline{Z}$ the atomic mass and the atomic number, Z_{eff} the effective nuclear charge and κ a constant parameter. The larger is λ_q the wider the diffusion area of the power entering the SOL will be, softening the thermal loads for the divertor. The power width is inversely proportional to the plasma current, which increases with the reactor power.

$$q = q_0 \cdot e^{-\frac{y(\theta)}{\lambda_q}} \left[\vec{B}, \hat{n} \right] \tag{19}$$

Equation 19: Heat flux exponential decay in the radial direction

With q_0 the heat flux for a zero poloidal angle $\theta = 0$, $y(\theta)$ is the distance from the separatrix

as a function of the poloidal angle, $\left[\vec{B}, \hat{n}\right]$ the scalar product between the incident magnetic field on the target and the the surface normal of the divertor (the incident heat flux can be smoothed if the wetted area is extended by tilting the plates at different angles). This formula is correct only when the poloidal angle is such that the distance between the first wall and the separatrix is sufficient not to consider the perpendicular flow $q_\perp$ as the dominant term, for which $q = q_\perp + q_{//}$ with $q_\perp = 0$. If proximity to the wall is significant, the heat flux is equal to its perpendicular component $q = q_\perp$.
Fig.(7) shows a qualitative representation of how the trend of the thermal flow to the wall could be depending on the poloidal angle.

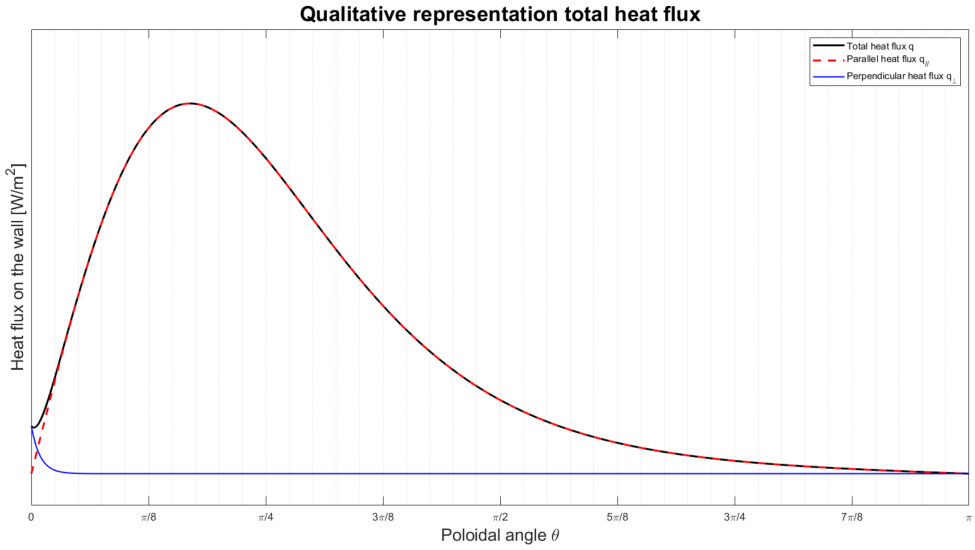

Figure 7: Qualitative trend of the heat flux

Taking into consideration Eq.(14) on energy balance it is possible to define:

$$P_\alpha + P_{heating} = P_{rad} + P_{SOL} \tag{20}$$

Equation 20: Power balance between Core and SOL

Eq.(20) describes the power balance from the core POV, where the heat sources are defined on the left and the dissipation phenomena on the right. P_α is the power associated to the α-particles and $P_{heating}$ the power delivered to the plasma to maintain the correct conditions shown in Eq.(17). $P_{heating}$ can be provided through a series of different techniques as the *Neutral Beam Injection* (NBI), the *Electron Cyclotron Resonance Heating* (ECRH), the *Ion Cyclotron Resonance Heating* (ICRH) and the Ohmic power induced by the plasma current. P_{SOL} is the power lost from the core and sent to the SOL, destined to converge downwards in the divertor plates, it can be conceptually split into two energy transport channels: radiation $P_{rad,SOL}$ (isotropical) and advection/convection $P_{adv,SOL}$ (directed towards the divertor). P_{rad} is the radiated power from the core, it doesn't follow any direction but behaves isotropically. In Fig.(8) is shown the power distribution:

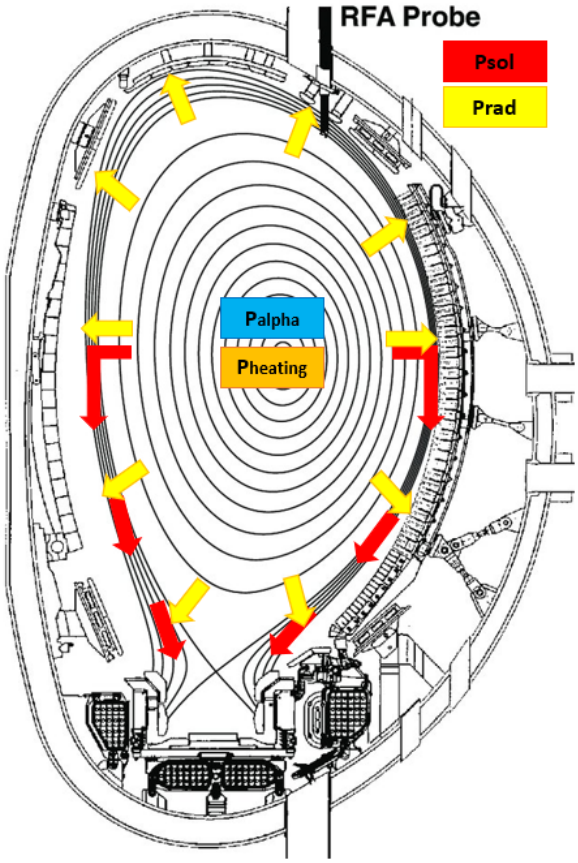

Figure 8: Qualitative trend of the heat flux

2.2 Plasma-Wall Interaction Phenomena and Description of Governing Equations

Given the strong thermal and particle load to which the divertor is subjected, various phenomena of interaction with the solid material can occur - *Sputtering* first of all - changing the nature of the plasma and consequently the possibilities for the reactions to take place. It is important to remember that in the nucleus the particles are completely ionized (no possibility of having neutrals such D^0, T^0, H^0, He^0), while in the SOL the temperatures are lower and the particles can also appear without charges. In addition, erosive phenomena can introduce charged or neutral particles of the divertor material (W^0,W^+, up to W^{+7}), contributing to increase radiation phenomena and therefore energy loss.

The term *Erosion* means the disintegration, after particle collisions with the target, of part of the PFCs material and the consequent rejection into the plasma. In particular, the concept of *Physical sputtering* is fundamental. Physical sputteringg is a physical process that involves the removal of atoms or molecules from a solid surface due to collisions with high-energy particles, such as ions or neutral atoms coming from the plasma. The kinetic energy transferred during the collision is sufficient to overcome the atomic or molecular binding forces on the surface of the material, causing atoms or molecules to be ejected from

the surface. The energy transferred during this collision is given by:

$$\gamma = \frac{4 m_r m_p}{(m_r + m_p)^2} \tag{21}$$

Equation 21: Energy fraction in a sputtering interaction

In this context, m_r represents the mass of the particle that gets reflected, and m_p stands for the mass of the projectile. Usually, the plasma is composed of deuterium with a mass of 2 atomic mass units (u), while the target is made of tin, which has a mass of $183.84u$. Consequently, when deuterium collides with tin, a maximum energy fraction of $\gamma_{D/T} = 0.043$ is transferred. The minimum energy required by the projectile to dislodge an atom, often referred to as the *threshold energy*, can be calculated as follows:

$$E_{thr} = \frac{E_{B,surf}}{\gamma(1-\gamma)} \tag{22}$$

Equation 22: Threshold energy formulation for in sputtering interaction

Here, $E_{B,surf}$ represents the *Surface Binding Energy* (binding energy related only to the atoms on the surface). The sputtering yield can be computed for different energy levels of the deuterium ion using the formulation Eq.(23) proposed in [15]:

$$Y(E_k) = 6.4 \cdot 10^{-3} \cdot m_r \gamma^{2.5} E_k^{0.25} \left(1 - \frac{E_{thr}}{E_k}\right)^{3.5} \tag{23}$$

Equation 23: Sputtering Yield formulation

With E_k the kinetic energy of the projectile particle (in eV). Considering the phenomenon of sputtering for the portions of a common configuration divertor, the surface binding energy is $E_{B,surf} = 11.75eV$. As a result, the calculated threshold energy is $E_{thr} = 288.19eV$ and, in the case where impurities are absent, the sputtering yield follows the trend shown in Fig.(9):

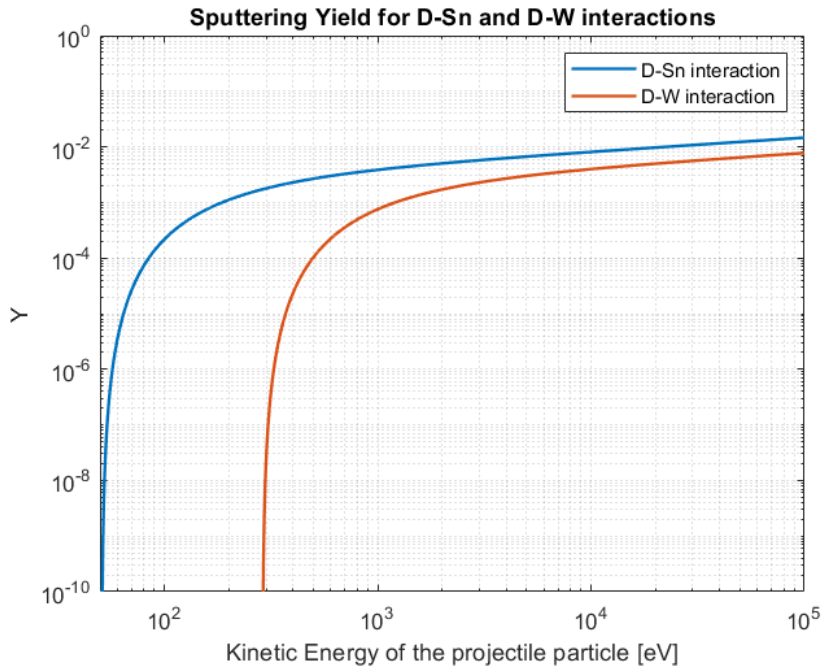

Figure 9: Sputtering Yield according to different kinetic energies of the projectile particle - Cases in which a D particle hits a tin or a tungsten surface. No impurities considered.

The figure represents the trend for sputtering (not considering the presence of impurities) due to both the deuterium-tungsten interaction and the deuterium-liquid tin interaction, related to the Liquid Metal Divertor configuration, a concept that will be described in 2.5.3. The tin trend was extracted by using the equations Eq.(21), (22) and Eq.(23), considering an atomic weight of $m_r = 118.71u$ and surface binding energy of $E_{B,surf} = 3.1eV$ ([16]). It is possible to notice that the minimum threshold of kinetic energy required for sputtering to occur tends to be higher as the atomic mass increases. Indeed, for solid tungsten, the minimum threshold is $288.19eV$. Following this trend, the higher the atomic number of the constituting element of the target, the larger the kinetic energy of the projectile necessary to extract the particle from the wall. Certainly, the higher the atomic mass (Z) of the extracted element, the greater the energy losses due to radiation emissions resulting from the plasma-element interactions. Eroded particles can also be redeposited if certain conditions are met.

In Fig.(10) and in the following list, are summarized the radiation phenomena and the main perturbation reactions of the plasma.

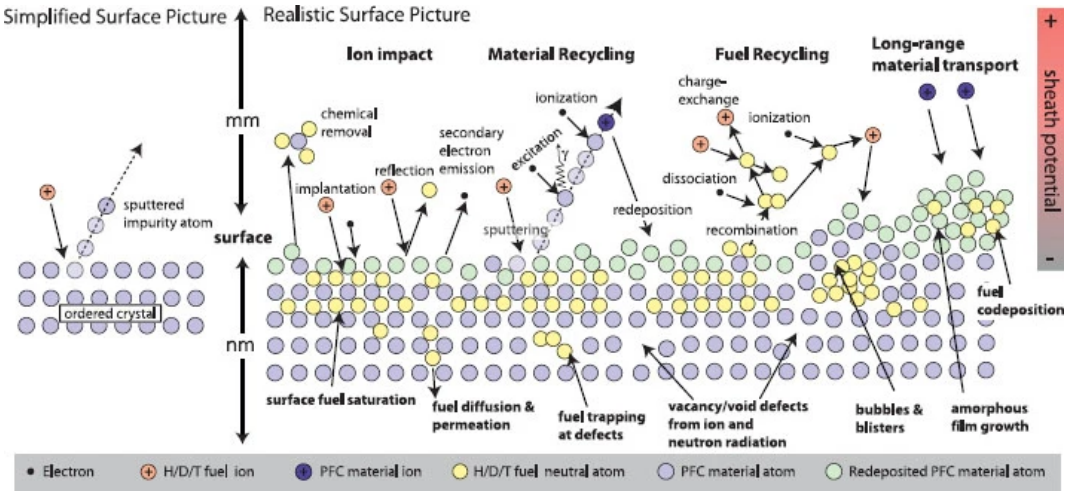

Figure 10: Scheme of possible phenomena due to plasma-wall interactions

- *Recombination*: plasma ions and electrons impact on the divertor target at sound speed. They are kept to the wall until this one reaches the saturation. Once the wall becomes saturated, ions and electrons are recombined to obtain a neutralized particle, which is emitted with the same thermal energy of the wall:

$$e^- + D^+_{hot} \rightarrow D^0_{cold} \tag{24}$$

Equation 24: Recombination formula

it is useful to write the phenomenon just described in mathematical form, considering it as a source/sink for the following balances:

$$S^P_{i,rec} = - < \sigma v >_{rec} n_e n_i \tag{25}$$

$$\vec{S}^M_{i,rec} = - < \sigma v >_{rec} n_e n_i m_i \overline{u_0} \tag{26}$$

$$S^E_{i,rec} = - < \sigma v >_{rec} n_e n_i \frac{3T_i}{2} \tag{27}$$

Equation 27: Recombination sink/sources for 22) particle balance, 23) momentum balance, 24) energy balance

The minus before the formulation means that this phenomena is a sink for ions population;

- *Ionization*: when a neutral particles detaches from the wall and come closer to the core region the temperatures increase, improving the atomic energy and facilitating the probabilities of changing electron configuration after a perturbation. Free electrons can perturb the atomic state transferring part of their energy to the atom, which reaches the threshold necessary to lose an electron becoming a charge particle:

$$e^- + D^0 \rightarrow D^+ + 2e^- \tag{28}$$

Equation 28: Ionization formula

With the sources:

$$S^P_{i,iz} =< \sigma v >_{iz} n_e n_o \tag{29}$$

$$\vec{S}^M_{i,iz} =< \sigma v >_{iz} n_e n_o m_i \overline{u_0} \tag{30}$$

$$S^E_{i,iz} = - < \sigma v >_{iz} n_e n_0 \frac{3T_0}{2} \quad S^E_{e,iz} = - < \sigma v >_{iz} n_e n_0 E_{iz} \tag{31}$$

Equation 31: Ionization sink/sources for 26) particle balance, 27) momentum balance, 28) energy balance

The plus before the momentum source term means that the plasma (ions and electrons) acquires the momentum of the neutral. From the energy POV, the ions gain the energy of the neutral, but electrons lose the energy associated to the ionization energy necessary to create the charge particle. Ionization and recombination can be seen as opposite mechanisms, they occur at different position of the SOL, according to the local temperatures. It can be stated that neutrals cannot travel too far from the wall before being ionized, and ions cannot collide with the wall without being converted to neutral sooner or later;

- *Charge-exchange*: In this case, neutral cold particle coming from the target (fuel recycling phenomenon) collides with a hot charge particle from the core, this perturbation leads to an exchange of charge where the neutrals is the hot particle and the ion is the cold one.

$$D^0_{cold} + D^+_{hot} \rightarrow D^+_{cold} + D^0_{hot} \tag{32}$$

Equation 32: Charge-exchange formula

With the sources:

$$\vec{S}^M_{i,cx} =< \sigma v >_{cx} n_i n_o m_i (\vec{u_0} - \vec{u_i})) \tag{33}$$

$$S^E_{i,cx} = - < \sigma v >_{cx} n_i n_0 \frac{3(T_0 - T_i)}{2} \tag{34}$$

Equation 34: Charge-exchange sink/sources for 30) momentum balance, 31) energy balance

For this phenomenon there is no particle balance since the number of ions and neutrals is the same before and after the collision. Moreover, the momentum term is expressed

with the relative velocity of the reaction $\vec{u_0} - \vec{u_i}$, just as the energy exchange is expressed as the internal energy difference $3(T_0 - T_i)/2$;

The sputtering improves the presence of impurities in the plasma, which induces radiation phenomena inside the SOL - such as *Bremsstrahlung* or *Line radiation* - increasing the power lost by radiation $P_{rad,SOL}$.

- Bremsstrahlung: it is an electromagnetic radiation based on the variation of the kinetic energy of a charged particle such as the electron, due to a change of trajectory induced by a more massive particle such as an atomic nucleus. When the charge particle is deflected, it try to satisfy the principle of conservation of energy by emitting a radiation of energy equal to the change in kinetic energy. The source term related to this radiation can be written as:

$$S^E_{e,BRM} = 5.35 \cdot 10^3 Z_{eff} (n_{20})^2 (T_k)^{1/2} \tag{35}$$

Equation 35: Bremsstrahlung source term

With:

$$Z_{eff} = \sum_j \frac{Z_j^2 n_j}{n_e}$$

Where Z_j is the atomic number of the j-th species in the plasma, n_e is the electron number (density) and n_j is the j-particle number (density), both related to a single reaction. $Z_{eff} = 1$ is an indicator of the amount of impurities in the plasma, for a pure D-T plasma $Z_{eff} = 1$. n_{20} is the electron density expressed in $10^{20} m^{-3}$ and T_k is the temperature expressed in Kelvin.
Bremsstrahlung is directly proportional to the effective charge, the larger Z_{eff}, the bigger the quantitive of energy radiated. Considering the proportional relationship $S^E_{e,BRM} \propto T^{1/2}$, it's possible decleare that the bremsstrahlung is more important in the core plasma, where temperatures are higher than in the SOL. This kind of radiation is also proportional to the effective charge $S^E_{e,BRM} \propto Z_{eff}$, the less pure the plasma, the more radiation it emits;

- Line radiation: in this phenomenon, a free electron can perturb the electronic state of an atom, transferring energy to the atomic electrons and bringing them to an excited state, the subsequent de-excitation (return to ground level) will lead to irradiation and a consequent loss of energy. The formulation is:

$$S^E_{e,LINE.} = n_e n_0 L^D_{Z,LINE.} + \sum_{j=1}^{N_{impur.}} n_{Z,j} n_e L^j_{Z,LINE.} \tag{36}$$

Equation 36: Line radiation source term

Obviously, line radiation is associated to the excitation/de-excitation process, therefore, this kind of radiation cannot occur if ions are fully stripped of electrons. This principle imposes that at high temperatures - where it is easier to have completely ionized species and the presence of electrons in the atom is reduced - the phenomenon of linear radiation is minimal, or completely null. An important consideration related to the atomic number Z is that in the core plasma light impurities (low Z) are fully stripped of electrons, so no line radiation in this zone of the chamber; differently, heavy impurities (high Z) are never fully stripped and line radiation occur, the higher Z, the larger the radiation emitted;

The total radiation function for the species j is called *Cooling function* and is the sum of the linear radiation function, the radiation function for bremsstrahlung and the radiation function for radiation phenomena due to ionization:

$$L^j_{Z,cool} = L^j_{Z,BRM.} + L^j_{Z,LINE.} + L^j_{Z,IZ.} \tag{37}$$

Equation 37: Total radiation function expression

In Fig.(11) is shown the cooling function as a function of temperature:

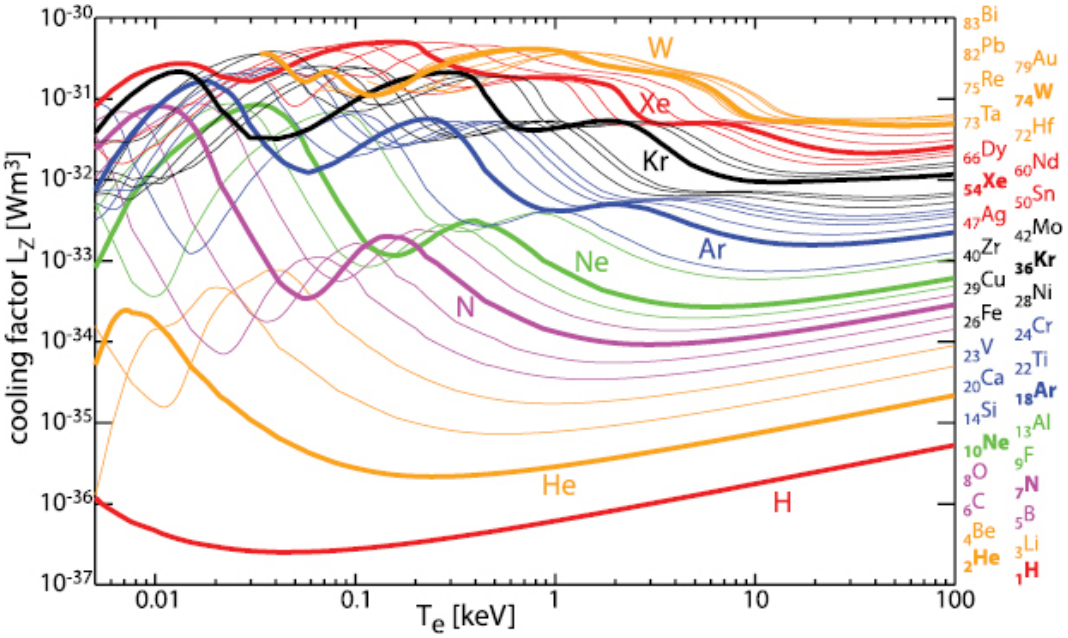

Figure 11: Cooling function representation

When temperature is low, the dominant contributor is the line radiation, with a very oscillating and chaotic trend. When temperature is high, the linear radiation loses importance and the global trend follows the proportionality ($S^E_{e,BRM} \propto T^{1/2}$).

For SOL plasma, the fluid model is adopted: the plasma in the SOL is characterized by a much lower density compared to the confined region, making fluid models more computationally efficient. Additionally, the SOL is dominated by collisional transport processes, while kinetic effects become negligible, hence charge particles mainly folow the parallel direction along the magnetic open field lines.
In order to establish the collisionality it's useful to take into account the *Knudsen number*, it is a dimensionless parameter used in the field of fluid dynamics and gas dynamics to characterize the flow regime of a gas. It is defined as the ratio of the molecular mean free path λ to a characteristic length scale of the flow $L_{\parallel}$ (represented by the half the target - to - target distance, so the upstream-target distance):

$$Kn = \frac{\lambda}{L_{\parallel}} \tag{38}$$

Equation 38: Knudsen number definition

When the Knudsen number is small ($Kn \ll 1$), the gas flow is considered to be in the continuum regime, where collisions between molecules dominate and the gas can be described by classical fluid dynamics equations. In this regime, the gas behaves like a fluid with well-defined pressure, density, and velocity fields.
On the other hand, when the Knudsen number is large ($Kn \gg 1$), the gas flow is in the rarefied regime. In this regime, the mean free path becomes comparable to or larger than the characteristic length scale, and molecular collisions become less frequent. The behavior of the gas deviates from the predictions of classical fluid dynamics, and phenomena such as slip flow and molecular diffusion become significant.
In the case of SOL plasma, the collisionality is generally high (Knudsen number low), thus the fluid model can be adopted as a reference model.
Fluid models are able to adequately capture macroscopic transport phenomena, such as diffusion and convection, relevant in the SOL. Furthermore, using fluid models simplifies the analysis and interpretation of results, allowing for a more intuitive understanding of the physical phenomena in the SOL. Therefore the *Braginskii fluid equations* are used, extracted by expanding the Fokker-Planck equation around a Maxwellian distribution. For the generic species s:

$$\frac{\partial f_s}{\partial t} + \bar{\mathbf{v}} \cdot \nabla f_s + \frac{Z_s e}{m_s}(\mathbf{E} + \mathbf{v} \times \mathbf{B}) \cdot \nabla_v f_s = \left(\frac{\partial f_s}{\partial t}\right)_{coll.} + Sources \tag{39}$$

Equation 39: Fokker-Planck equation for generic species s

By taking moments of Eq.(39) it's possible to obtain Braginskii fluid equations. It is important to underline that the set of equations presented below has been written for illustrative purposes, taking into consideration only the D^+ ions and the electrons. For the

complete description of SOL plasma it is necessary to include the equations for the other atomic species (T^+,He^+,He^{++}) and impurities.

The system should also foresee the presence of neutrals, not foreseen by the Braginskii equations, which describe only the ionized species. Therefore, a separate set of equations must also be considered for the neutral species. Source/sink terms listed in eq(25) through eq(36) are are included to comply with conservation laws.

Continuity equation (particle conservation):

$$\frac{\partial}{\partial t}(n_i) + \nabla(n_i \vec{u}_i) = S^P_{iz} + S^P_{rec} \tag{40}$$

$$n_e = n_i \tag{41}$$

Equation 41: Continuity equation for ions and electrons

For electrons the equality with ions expressed in Eq.(41) holds for the principle of quasi-neutrality.

Momentum conservation equation:

$$\left(\frac{\partial}{\partial t} + \vec{u}_i \cdot \nabla\right) m_i n_i \vec{u}_i = -\nabla p_i - \nabla \cdot \vec{\pi}_i + e n_i (\vec{E} + \vec{u}_i \times \vec{B}) + \vec{R}_i + \vec{S}^M_i \tag{42}$$

$$\left(\frac{\partial}{\partial t} + \vec{u}_e \cdot \nabla\right) m_e n_e \vec{u}_e = -\nabla p_e - \nabla \cdot \vec{\pi}_e + e n_e (\vec{E} + \vec{u}_e \times \vec{B}) + \vec{R}_e + \vec{S}^M_e \tag{43}$$

Equation 43: Continuity conservation equation for ions and electrons

Where:

- $\nabla \cdot \vec{\pi}$ is the divergence of the stress tensor associated to ions, responsible for viscous stress. Negligible for electrons;
- $e n_{i/e}(\vec{E} + \vec{u}_{i/e} \times \vec{B})$ the electro-magnetic force;
- $\vec{R}$ the rate of change of momentum due to collisions, it is based on the ion-electron friction force and on the parallel and perpendicular thermal forces. Considering the reciprocal exchange of momentum between electrons and ions $\vec{R}_e = -\vec{R}i$;
- $\vec{S}^M$ is the rate of momentum due to atomic process, given by the sum of the recombination, charge-exchange and ionization source/sink terms $\vec{S}^M = \vec{S}^M_{cx} + \vec{S}^M_{iz} + \vec{S}^M_{rec}$. This term is more relevant for ions balance, from an electronic POV is negligible;

Energy conservation equation:

$$\left(\frac{\partial}{\partial t}+\vec{u}_i\cdot\nabla\right)\left(\frac{3}{2}n_iT_i\right)+p_i\nabla\cdot\vec{u}_i=-\nabla\cdot\vec{q}_i+\nabla\cdot(\vec{\pi}_i\vec{u}_i)+en_i\vec{E}\vec{u}_i-\vec{R}_i\vec{u}_i+Q_{ei}+S_i^E \tag{44}$$

$$\left(\frac{\partial}{\partial t}+\vec{u}_e\cdot\nabla\right)\left(\frac{3}{2}n_eT_e\right)+p_e\nabla\cdot\vec{u}_e=-\nabla\cdot\vec{q}_e+\nabla\cdot(\vec{\pi}_e\vec{u}_e)+en_e\vec{E}\vec{u}_e-\vec{R}_e\vec{u}_e-Q_{ei}+S_e^E \tag{45}$$

Equation 45: Energy conservation equation for ions and electrons

Where:

- $p\nabla\cdot\vec{u}$ is the compression work;
- $\nabla\cdot\vec{q}$ is the conduction term. The term $\vec{q}$ represents the heat flux in plasma and shows an anisotropic heat conductivity:

$$\vec{q}_i=-X_\parallel^i\nabla_\parallel T_i-X_\perp^iT_i+X_\wedge^i\frac{\overline{B}}{B}\times\nabla_\perp T_i$$

$$\vec{q}_e=-X_\parallel^e\nabla_\parallel T_e-X_\perp^eT_e+X_\wedge^e\frac{\overline{B}}{B}\times\nabla_\perp T_e-0.71\frac{T_e}{e}j_\parallel-\frac{3}{2}\frac{T_e}{ew_e\tau_eB}\vec{B}\times\vec{j}_\perp$$

  With $X_\parallel=K_0T^{5/2}$ as the parallel heat conductivity ($K_{0,i}\simeq 60$ for ions, $K_{0,e}\simeq 2000$ for electrons), $X_\perp$ as the perpendicular heat conductivity and $X_\wedge$ as the conductivity along the direction perpendicular to both the magnetic field and the direction of the temperature gradien. The fourth and fifth terms on the right-hand of $\vec{q}_e$ equation are the convective component of the electron heat flux density, driven by motion of the electrons relative to the ions;
- $\nabla\cdot(\vec{\pi}\vec{u})$ is the viscous dissipation;
- $\vec{R}\vec{u}$ is the ohmic heating;
- Q_{ei} is the heating due to collisions between electrons and ions and is called *ion-electron energy exchange*, it is positive for ions and negative for electrons, depending by which charge gain energy after the collision:

$$Q_{ei}=3\frac{m_e}{m_i}n_e\nu_{ei}(T_e-T_i)$$

- $\vec{S}^E$ is the energy source, where:

$$\vec{S}_i^E=\vec{S}_{i,cx}^E+\vec{S}_{i,iz}^E+\vec{S}_{i,rec}^E$$

$$\vec{S}_e^E = \vec{S}_{e,cool}^E$$

With $\vec{S}_i^E$ the sum of the souces due to atomic process and $\vec{S}_e^E$ the sum of radiation phenomena (line radiation, ionization, bremsstrahlung) as described in Eq.(37), including both plasma particles and impurities;

In order to better follow the physics present in the SOL and facilitate the search for the solution, various simplifications and boundary conditions have been imposed, taking into account the simplification imposed by the *Two-point model*. In summary, the Two-point model is a simplified theoretical framework used to describe the basic behavior and control of the plasma in a tokamak. It focuses on two key locations: the core (defined as *Upstream point*), where the plasma temperature is highest, and the edge (also called *Target point*), where the plasma interacts with the tokamak walls. In particular, this model establishes a relationship between these two points to analyze the plasma behaviour, as well as to define an additional area close the target named *Sheath edge*. This area separates the target from the SOL plasma and has an extremely reduced thickness, where just ions can enter (at the sound speed) and the principle of quasi-neutrality is not valid anymore ($n_i \neq n_e$).
The assumptions and boundary conditions useful for solving the equation set are shown below:

- Principle of quasi-neutrality not valid;
- Conversion of the 3D problem to a 1D problem, following the direction of the magnetic field (parallel direction, projection on $\tilde{e}_\parallel$);
- Imposition of the steady-state condition by removing the time-dependent variable and time derivative;
- Viscosity and viscous dissipation neglected;
- Ambipolar flow ($u_i = u_e$);
- Charge particles at the same temperature ($T_i = T_e$);
- *Bohm criterium*, the particle velocity at the target is the sound speed:

$$u_{\parallel,Target} = -c_s = -\sqrt{\frac{k_B \cdot (T_e + T_i)}{m_i}} \tag{46}$$

Equation 46: Bohm criterium - 1st Bound.condition

The sound speed is defined as a function of the ion and electron temperature over the particle mass (in this case is represented only the ion mass since $m_i \gg m_e$)

- Considering $x_\parallel$ the direction perpendicular to the target and parallel to the transport direction, with the origin at the target, the density far from the wall can be evaluated as:

$$n(x_{\parallel} = L_{\parallel}) = n_{upstream} \tag{47}$$

Equation 47: Density evaluation far from the target - 2nd Bound.condition

Where $n_{upstream}$ can be measured or calculated just relating to the average core plasma density.

- The parallel heat flux $q_{\parallel}$ far from the wall:

$$q_{\parallel}(x_{\parallel=L_{\parallel}}) = q_{\parallel,upstream} \tag{48}$$

Equation 48: Heat flux evaluation far from the target - 3rd Bound.condition

With:

$$q_{\parallel,upstr.} = \frac{P_{SOL,outboard}}{2\pi R_{upstr.} \left(\frac{B_\theta}{B}\right)_{upstr.}}$$

Where $P_{SOL,outboard}$ is the portion of power in the SOL going to the outboard target divertor.

- The heat conduction - considering the temperature along the parallel direction $T_{\parallel}$ - can be calculated as:

$$q_{\parallel,cond.} = -K_{0,e} T_{\parallel}^{5/2} \frac{dT}{dx_{\parallel}} \tag{49}$$

And the target temperature:

$$T(x_{\parallel} = 0) = \frac{q_{\parallel,targ.}}{\gamma_{se} \Gamma_{se}} \tag{50}$$

Equation 50: Heat conduction evaluation - 4th Bound.condition

With $\gamma_{se} \simeq 7$ the sheath heat transmission factor and Γ_{se} the particle flux at the sheat edge defined as $\Gamma_{se} \simeq n_{targ.} c_s$;

At the end, three governing conservation equations are found, including the balance of power, momentum and particle density between the core and the edge:

$$2 n_t T_t = n_u T_u \tag{51}$$

$$T_u^{\frac{7}{2}} = T_t^{\frac{7}{2}} + \frac{7}{2} \frac{q_{\parallel} L_{\parallel}}{K_{0,e}} \tag{52}$$

$$q_{\parallel} = \gamma_{se} \Gamma_{se} T_t \tag{53}$$

Equation 53: Two-point model simplified conservation equation set

2.3 Detachment Regime

All the phenomena described are an important part of what is defined as *Detachment regime*. Plasma detachment from a divertor target is defined as the state in which large gradients in total plasma pressure (static + dynamic) are observed parallel to the magnetic field with consequent reductions in the plasma power and ion fluxes to the limiting surfaces [2]. The gradients also develop from a thermal POV, the thermal load tends to decrease significantly near the target divertor, with an increasingly encouraged irradiation due to the impurities near the target. This leads the temperatures at the sheath edge below few eV, a very favourable condition to maintain the integrity of the component.
In the detachment regime the parallel gradients are very important: the ion flux, the deposited power and the plasma temperature decrease significantly compared to the central core condition, leading to a comfortable situation where nuclear reactions can take place in the core and the thermal conditions and the particle loads are small enough near the divertor to allow it to function properly. Obviously, the amount of impurities needs to be controlled and limited, a too massive presence of impurities leads to too high a power loss, such that the lawson criterion risks not being respected and the reactions stop, shutting down the reactor.

Therefore, plasma detachment can be more quantitatively defined as a significant loss term in the continuity equation for energy, momentum and particle flux parallel to the magnetic field lines from the SOL to the divertor target. While dissipation of energy is the primary goal for detached divertors, the dissipation of pressure upstream of the target is also important in order to reduce the ion flux and associated ionization energy of recombination within the material surface. Finally plasma recombination within the divertor plasma may also aid in reducing target particle and associated energy fluxes. The classical Two-point model is not able to describe properly the detachment since quantities are assumed to be conserved along the mangetic field lines from the upstream to the target. It is necessary to consider some dissipative terms in order to express the energy and momentum losses which characterize this kind of regime, hence the modified Two-point model is taken into account.

$$T_t = \frac{q_\parallel^2}{n_u^2}\left(\frac{2K_{0,e}}{7q_\parallel L_\parallel}\right)^{4/7}\frac{2m_i}{\gamma^2 e^2}\frac{(1-f_{pow})^2}{(1-f_{mom})^2\cdot(1-f_{conv})^{4/7}} \tag{54}$$

$$n_t = \frac{n_u^3}{q_\parallel^2}\left(\frac{7q_\parallel L_\parallel}{2K_{0,e}}\right)^{6/7}\frac{\gamma^2 e^3}{4m_i}\frac{(1-f_{mom})^3\cdot(1-f_{conv})^{6/7}}{(1-f_{pow})^2} \tag{55}$$

$$\Gamma_t = \frac{n_u^2}{q_\parallel}\left(\frac{7q_\parallel L_\parallel}{2K_{0,e}}\right)^{4/7}\frac{\gamma e^2}{2m_i}\frac{(1-f_{mom})^2\cdot(1-f_{conv})^{4/7}}{(1-f_{pow})} \tag{56}$$

Equation 56: Two-point model simplified conservation equation set

Where f_{pow} is the fraction of parallel heat flux dissipated in the SOL between the two points of the model, f_{mom} is the fraction of dissipation of total plasma pressure, and f_{conv} the fraction of heat flux carries by parallel convection.
These three parameters indicate the extent to which dissipative phenomena affect transport

phenomena between the core and the edge.

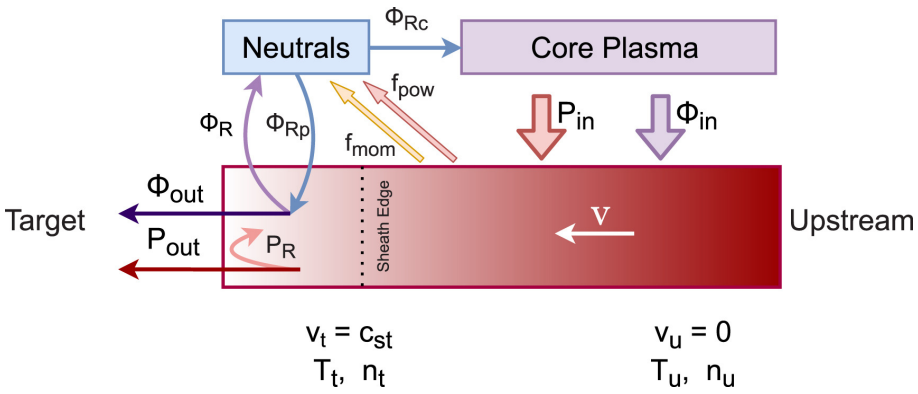

Figure 12: Modified Two-point model scheme.

2.4 Plasma confinement: L-mode and H-mode

The plasma in a fusion reactor can exist in two distinct operational states, *L-mode (Low Energy Confinement)* and *H-mode (High Energy Confinement)*, characterized by different plasma properties such as temperature, density, and energy confinement, which directly influence the efficiency of nuclear fusion. In a L-mode, the plasma inside the tokamak is relatively cold and diffuse, which means that density and temperature are low. In this state, the plasma is relatively unstable and can be easily disrupted by small perturbations, this results in a low level of confinement, so the plasma is not well-contained in the magnetic field and tends to leak out. Hence, the L-mode is characterized by relatively large amounts of turbulence, which allows energy to escape the confined plasma. This configuration is typically used in the early stages of a fusion experiment, when scientists are still tuning the parameters of the device and testing different configurations. It is also used as a baseline for comparison with other operating modes, such as the H-mode.
It's known that the fusion triple product indicates that both temperature and energy confinement time of the fusion fuel must be sufficiently high for fusion ignition. Achieving high core plasma temperatures for fusion necessitates additional heating beyond Ohmic heating, hence auxiliary heating techniques such as *Neutral-beam injection (NBI)*, *Electron Cyclotron Resonance Heating (ECRH)* and *Ion Cyclotron Resonance Heating (ICRH)*. However, it has been observed that the energy confinement time scales inversely with applied power and the turbolence characterizing . The L-mode, characterized by large amount of turbulence, allows energy to escape from the confined plasma and defines energy confinement time τ_E (as empirically described by the ITER89-P scaling expression [3]):

$$\tau_E = 0.038 M^{0.5} I_P^{0.85} \epsilon^{0.3} R^{1.5} \kappa^{0.5} n^{0.1} B^{0.2} P^{-0.5} \tag{57}$$

With M the hydrogen isotopic mass number, I_P the plasma current in MA, ϵ the inverse aspect ratio, R the major radius in m, κ the plasma elongation, n the line-averaged plasma density in $1e19$ $part./m^3$, B the toroidal magnetic field in T, P the total heating power in MW.
When the applied heating power surpasses a certain threshold, the plasma undergoes a

spontaneous transition into a higher-confinement state, where the energy confinement time roughly doubles in magnitude. However, it still exhibits an inverse dependence on heating power. This enhanced confinement regime is known as the H-mode. The better condition is confirmed by the energy confinement time, which can be up to 2-times higher than the one of a plasma operating in L-mode [1] (two operational branches exist for a given setting, the space in between is not accessible):

$$\tau_E = 0.0562 M^{0.19} I_P^{0.93} \epsilon^{0.58} R^{1.97} \kappa^{0.78} n^{0.41} B^{0.15} P^{-0.69} \tag{58}$$

In an H-mode, the plasma is much hotter and denser and passing from the L-mode to the H-mode means that energy, particle, impurity and momentum transport improve simultaneously. Obviously, due to its improved confinement properties, H-mode quickly became the desired operating regime for most future tokamak reactor designs.However, H-mode plasmas are also characterized by magnetohydrodynamics (MHD) instabilities, specifically *Edge Localized Modes (ELMs)*. ELMs manifest as fast and periodic relaxations of the transport barrier, causing the expulsion of particles and power from the core to the edge plasma and eventually to the tokamak wall.
To make the transition from the low-confinement plasma regime into the high-confinement plasma regime is necessary supply additional power to the plasma, elevateing also its temperature. The shift from low to high confinement regimes, known as the L-H transition, was initially observed in the ASDEX tokamak in 1982 on the ASDEX tokamak by Friedrich Wagner [7], and represent a crucial step of the fusion research. Beyond the L-H transition power threshold P_{L-H} the enhancements in density and temperature occur, leading to improved particle and energy confinement, are localized at the edge of the tokamak. Steep gradients in density and temperature emerge, attributed to the formation of an edge transport barrier. Fig.(13) illustrates the qualitative behavior of radial plasma pressure profiles in L-mode and H-mode.

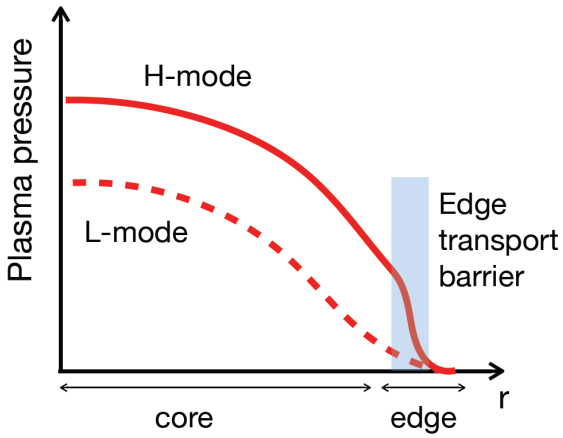

Figure 13: Radial plasma profiles in L-mode and H-mode.

Plasmas in both L-Mode and H-Mode exhibit distinct characteristics concerning turbulence, control, power thresholds, energy efficiency, and confinement durations. H-mode

mantains:

- Low turbulence, so high stability;
- High power threshold;
- More efficiency from an energetic POV;
- Longer confinement time with respect to the L-Mode case, up to 30 seconds;
- Creation of a region characterized by a high gradient of density and temperature;

2.5 ASDEX Upgrade description

This thesis is focused on simulating the behavior of plasma in pure deuterium with respect to the ASDEX Upgrade machine (AUG). ASDEX Upgrade (Axially Symmetric Divertor Experiment Upgrade) is a fusion research device, specifically a tokamak, located at the Max Planck Institute for Plasma Physics in Garching, Germany. It is an upgraded version of the ASDEX (Axially Symmetric Divertor Experiment) tokamak, and started to operate since 1991[13].It is part of that set of experimental reactors designed to study the physics of plasmas and to develop the technology necessary for a future fusion power plant. The ability to operate with different magnetic field configurations allows researchers to explore different plasma regimes, making the plant a major contributor to research into plasma and the possible regimes that future reactors will have to support.
ASDEX Upgrade uses a combination of materials in different parts of the tokamak, depending on their specific requirements. The first wall of the plasma-facing components are made of tungsten, which has a high melting point and is resistant to erosion and radiation damage, making it well-suited for this application. Specificaly, in the divertor, tungsten tiles are arranged in a specific pattern to control the flow of plasma and reduce the heat load on the divertor components.
Other components in the tokamak, such as the vacuum vessel and the magnets, are made of different materials, such as the vacuum vessel that encloses the plasma, which is made of stainless steel.
ASDEX Upgrade has also been used to study the behavior of other materials under fusion-relevant conditions, such as carbon-fiber composites and beryllium. In particular, carbon-fiber composites are being investigated for use in future fusion reactors due to their high strength and low thermal expansion coefficient, while beryllium is being studied for use as a neutron multiplier in fusion fuel blankets.
Overall, the materials used in ASDEX Upgrade are carefully chosen to withstand the extreme conditions inside the tokamak and to provide the best possible performance and safety.
ASDEX Upgrade is, compared to other international tokamaks, a midsize tokamak experiment. The plasma is controlled through a system of 12 vertical field coils and kept in its elliptical shape with an X-point above the bottom divertor. Tab(1) gets an overview of the global technical parameters:

Technical Data	**Value**
Total height of the system	$9\,m$
Total radius over all	$5\,m$
Weight of the system	$800\,t$
Number of toroidal field coils	16
Number of poloidal field coils	12
Maximum magnetic field	$3.1\,T$
Plasma current	$0.4 - 1.6\,MA$
Pulse duration	$< 10\,s$
Plasma heating	$\simeq 27MW$
Ohmical heating	$1MW$
Neutral beam injection heating	$20MW$ (with D)
Ion-Cyclotron heating	$6MW\,(30MHz - 120MHz)$
Electron-Cyclotron heating	$2 \times 3MW\,(140GHZ)$
	$2 \times 2.5MW\,(105GHZ)$
Energy confinement time	up to $0.2\,s$

Table 1: AUG technical data

Control computers calculate through a large number of measurement coils the actual values from the plasma position and plasma shape and correct the currents in the field coils in order to achieve the desired values. The typical values are reported in Tab.(2):

Typical plasma parameters	**Value**
Major plasma radius R_0	$1.65\,m$
Minor horizontal plasma radius a	$0.5\,m$
Minor vertical plasma radius b	$0.8\,m$
Ellipticity b/a	1.8
Plasma types	Deut., Hydrog., Helium
Maximum magnetic field	$3.1\,T$
Plasma volume	$14\,m^3$
Plasma mass	$3\,mg$
Plasma density	$2 \cdot 10^{20}\,part./m^3$
Electrondensity	$10^{20}\,m^{-3}$
Plasma Temperature	$60 - 100$ million degree

Table 2: AUG plasma parameters

The data presented in the tables Tab.(1) and Tab.(2) are provided by the Max Planck Institute for Plasma Physics through their documentation channels, as reported in [13], [14]. Fig.(14) represents the complete structure of the experimental reactor, scaled to human dimensions.

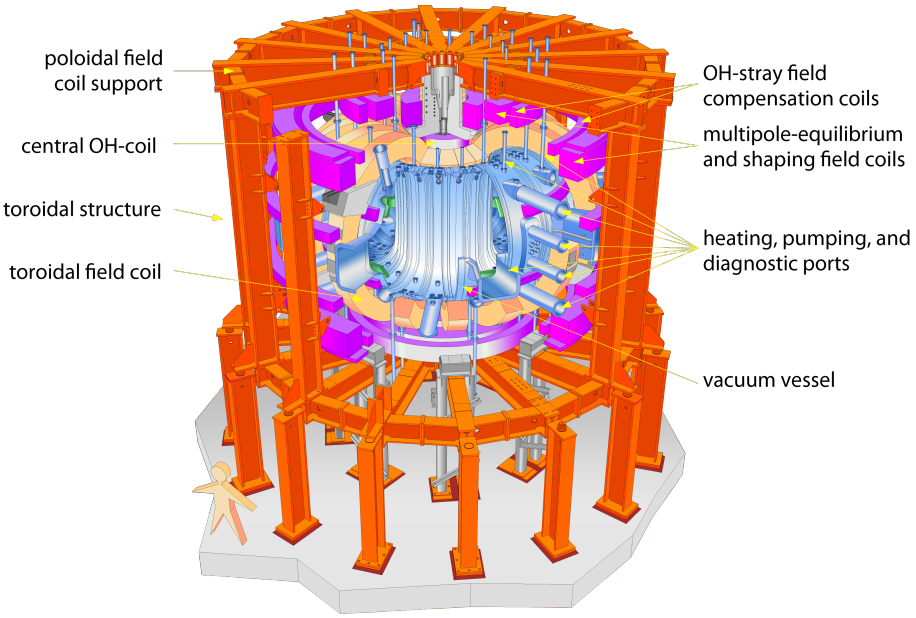

Figure 14: Complete depiction of the ASDEX Upgrade structure. Original source: Max Planck Institute for Plasma Physics website.

Fig.(16) shows an internal view of the structure, depicting the internal chamber housing the plasma formed during the experiments. It is worth noting how the structure is modulated across its entire surface, ensuring a degree of interchangeability among the components to preserve their integrity and enable a precise study of plasma-wall interactions.

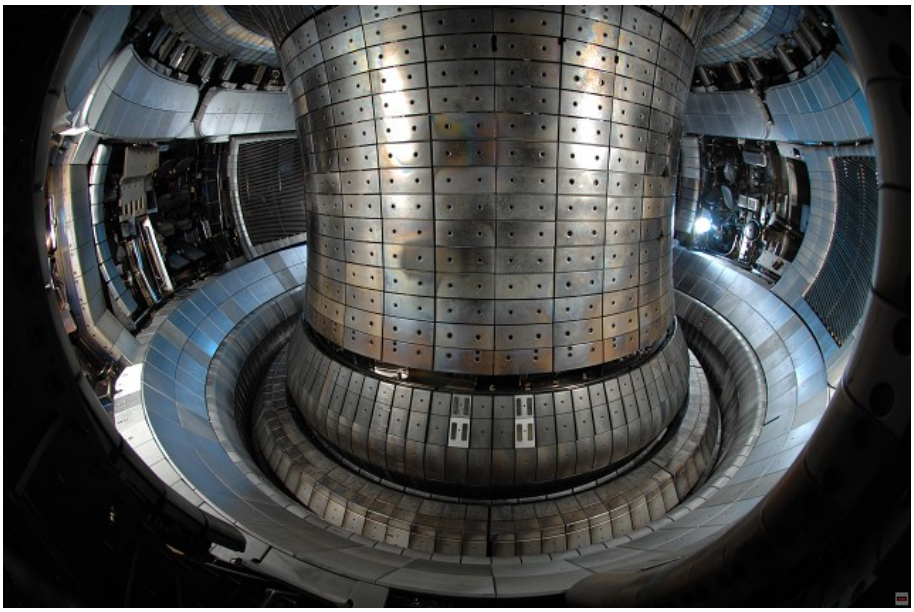

Figure 15: Complete depiction of the internal chamber housing the plasma. Original source: Max Planck Institute for Plasma Physics website.

2.5.1 Magnetic coils and plasma shaping

The image below illustrates the positioning of the magnets within the poloidal section, depicting the central solenoid, the toroidal magnet of the same section, and the auxiliary magnets for the vertical magnetic field. The confining magnetic field is essentially generated by 16 large copper magnet coils wrapped around the ring-shaped plasma vessel, along with 17 auxiliary coils.

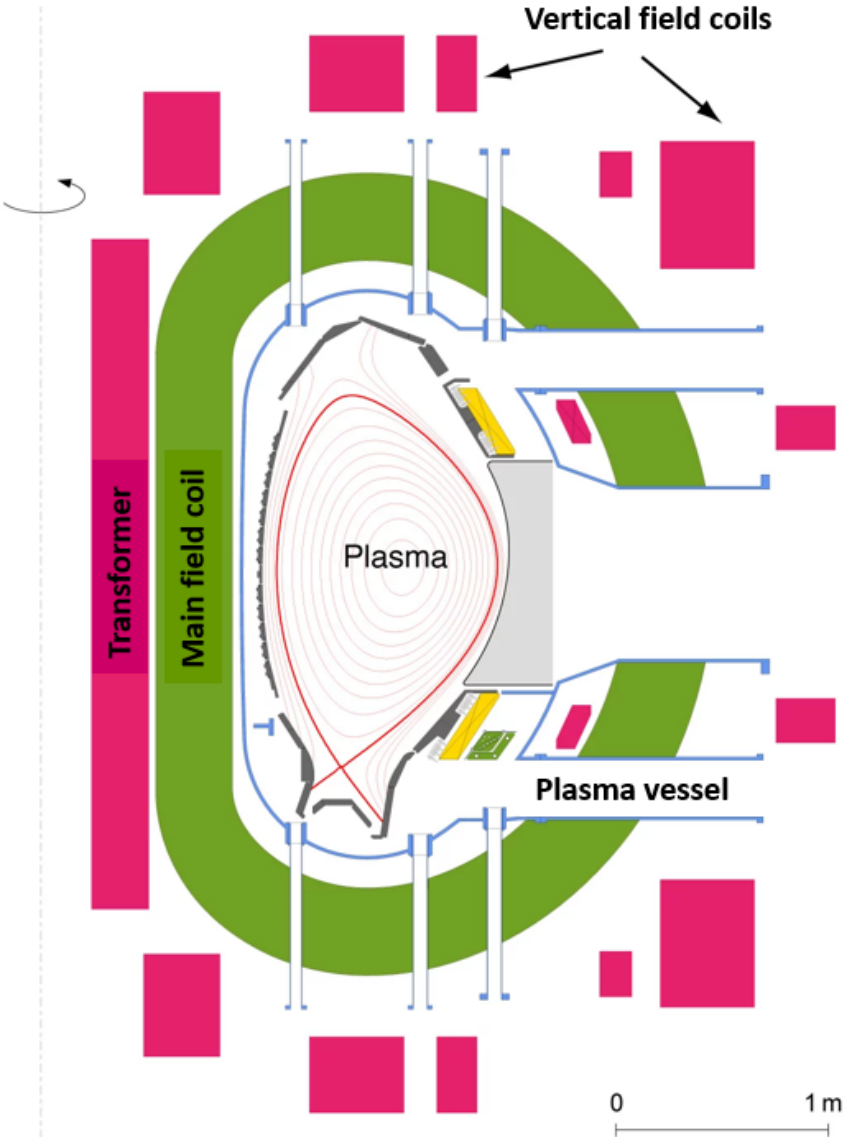

Figure 16: Depiction of field coils disposition in ASDEX Upgrade. Poloidal section.

Most modern fusion devices utilize normally conducting magnet coils made of copper. For instance, the main-field coils of ASDEX Upgrade, which are $2.5m$ in height, are constructed using copper rails approximately the width of a hand. To facilitate cooling, they are equipped with channels for the circulation of cooling water. The windings are insulated with fiberglass bands and encased in synthetic resin to connect them together and provide

the coil with the required mechanical strength. Consequently, the coil can withstand the significant forces that arise between the coils once the coil current is activated.
The future goal is to operate a fusion power plant with superconducting coils. This entails using niobium-titanium superconductors capable of generating a magnetic field of $13\,T$ (on the coil, approximately $5.7\,T$ on the magnetic field axis). In contrast to copper coils, superconducting coils, when cooled to low temperatures, consume virtually no energy once activated; the coil current flows with minimal losses.
Through the flowing current, the magnets create a magnetic field around the plasma inside the tokamak, which helps confine and stabilize the plasma, thanks to the presence of magnetic surfaces. This is crucial to prevent the plasma from coming into contact with the walls of the container, ensuring that it doesn't cool down or dissipate energy before reaching the conditions necessary for nuclear fusion, preserving also the integrity of the plasma facing components. Hence, magnets are used to shape and manipulate the plasma within the tokamak, ensuring that it is adequately contained and uniformly heated to achieve the conditions for fusion. The magnetic coil system is complex and takes into account the need to superimpose different magnetic field configurations to form a total field capable of adequately confining the plasma. The plasma column is thus deformed, with the deformation process being mediated through the use of toroidal coils (located step by step along the toroid), poloidal coils (positioned more externally and continuous along the length of the toroid), and auxiliary coils (primarily used to stabilize the plasma column). In Fig.(17), a simplified diagram illustrates how the deformation of the plasma column occurs through the presence of localized magnetic coils:

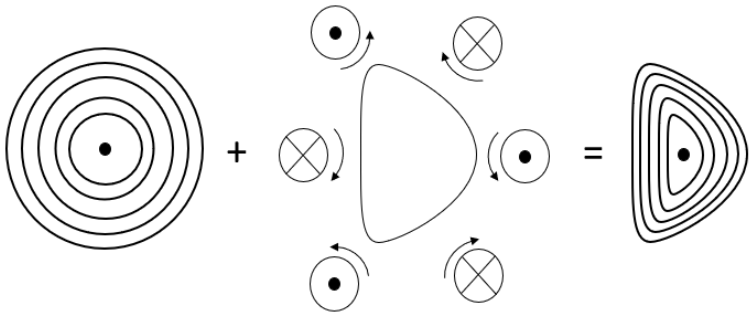

Figure 17: Plasma shaping semplificative example. Note how the magnetic surfaces are deformed due to interaction with nearby coils.

The magnets work also to prevent plasma instabilities that could hinder the maintenance of the necessary conditions for nuclear fusion. The creation of magnetic surfaces, and consequently magnetic filed lines, help to direct high-energy particles out of the plasma towards the divertor, contributing to preventing excessive temperature ramp-up on the other parts of the wall. So preventing damages from the high temperature of the plasma.

2.5.2 Plasma heating systems

To achieve the necessary initial conditions to initiate fusion reactions, the tokamak needs to deliver a certain amount of power to the core. The introduction of power happens through various heating methods in the ASDEX Upgrade tokamak. It helps achieve the high temperatures required for fusion reactions, maintain plasma stability, increase energy density, and create favorable conditions for these reactions. Each heating technique plays a specific role in this process. It is important to note that these techniques can be used simultaneously, as it is not always possible to achieve the desired conditions solely through a single system:

- Ohmic heating (P_{OH}). This is the primary heating technique used at the beginning of a discharge in the tokamak. It is based on the principle of the Joule effect, where an electric current passes through the plasma, and the electrical resistance within the plasma heats the material. In the tokamak, the current is applied in a controlled manner through the plasma using magnetic coils and causes the plasma to initially heat up. The values reported in Fig.(21) are the results of the plasma current and the voltage related $I_P \cdot U_{loop}$;

- Neutral Beam Injection heating (P_{NBI}). This technique involves injecting high-energy neutral particles into the plasma. Neutral particles are not charged and can penetrate the plasma without being deflected by the magnetic field. Inside the plasma, these neutral particles become ionized and transfer their kinetic energy to charged particles, raising the plasma temperature.
  In the NBI system, neutral particles, typically hydrogen or deuterium, are first ionized to create positively charged ions (in ths system, the ion source produces not only atomic H^+ (D^+) ions, but also molecular H_2^+ and H_3^+ (D_2^+ and D_3^+) ions. The positively charged ions are then accelerated to very high energies using an accelerator system, such as electrostatic or magnetic accelerators, imparting kinetic energy to the ions. After acceleration, the high-energy ions pass through a gas target, which is typically filled with neutral gas. During this interaction, the accelerated ions capture electrons from the neutral gas, becoming neutral again. It's important to note that as they dissociate upon neutralization the resulting neutral hydrogen atoms carry only one half or one third of the full energy, respectively to H^+, H_2^+ and H_3^+. Consequently, the final neutral beam has three energy components of $E_0 = U_{ex} \cdot e$, $E_0/2$ and $E_0/3$, where U_{ex} is the acceleration voltage and e is the elementary charge. These high-energy neutral particles are injected into the plasma, travelling through the magnetic field lines and penetrating the plasma without being significantly deflected. The consequent collisions with plasma ions help to transfer energy, thus heating the plasma
  The NBI system on ASDEX Upgrade consists of two nearly identical systems, known as injector 1 and injector 2, each one equipped with four neutral beam sources. In the case of deuterium, each source is capable of delivering a neutral beam power of $2.5MW$. Therefore, the combined installed neutral beam power is $20MW$ for deuterium, while it is slightly lower at $13MW$ for protium. The two injectors are positioned exactly opposite to each other relative to the center of the system. Specifically, they are located in sectors 7 and 15, as shown in Fig.(18).

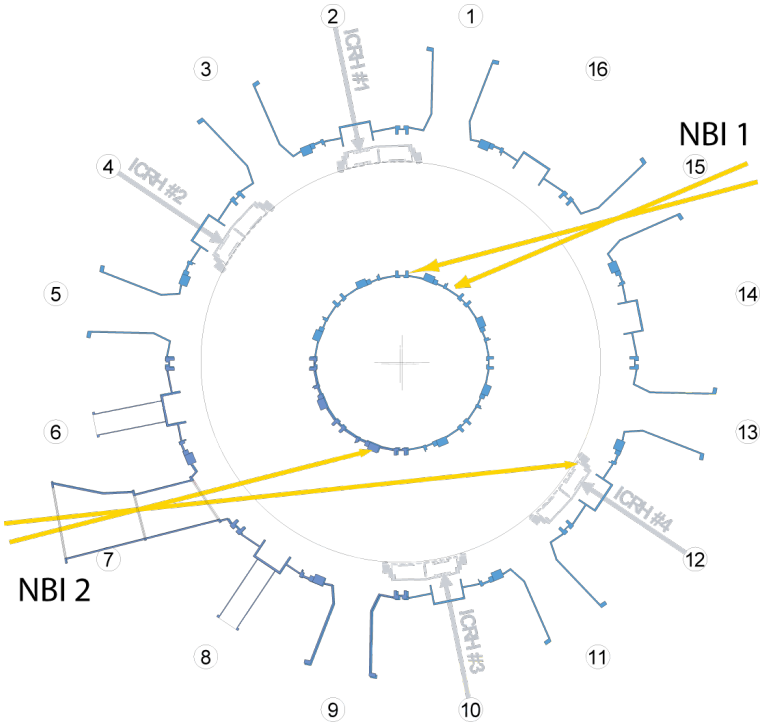

Figure 18: ASDEX Upgrade plasma heating systems depiction for NBI and ICRH systems.

Reionization losses of the neutral beam power result from the collisional ionization of fast neutrals with the background neutral hydrogen gas near the plasma. This phenomenon occurs in close proximity to the plasma, where the generated fast ions are redirected within the magnetic fringe field of the plasma device. These ions may collide with certain surfaces of the neutral injection system near the entrance aperture, potentially causing significant damage. Reionization can take place in two main locations: within the transmission line connecting the neutral beam injection box and the vacuum vessel of the plasma device (referred to as the duct) and within the scrape-off layer of the plasma. The reionization losses P_{r} rise with gas density n as:

$$P_{\mathrm{r}} = P_0[1 - \exp(-nL\sigma_{01})] \tag{59}$$

Where P_0 is the neutral beam power generated in the neutralizer, L the reionization path length and σ_{01} the cross section for the collisional ionization reaction $\mathrm{H}^0_{\mathrm{fast}} + \mathrm{D} \longrightarrow \mathrm{H}^+_{\mathrm{fast}} + \ldots$;

- Electron Cyclotron Resonance heating (P_{ECR}). It relies on the interaction between high-frequency electromagnetic waves, typically in the microwave or millimeter-wave range, and the electrons in the plasma. This interaction can transfer energy to the electrons, effectively heating the plasma.
  In a magnetic field, charged particles, such as electrons, move in helical paths. The frequency at which these particles gyrate around the magnetic field lines is known as the cyclotron frequency. When the frequency of the injected electromagnetic waves matches the electron cyclotron frequency, resonance occurs. At this point, the injected

high-frequency electromagnetic waves are absorbed by the electrons and as a result, the electrons gain energy from the waves. Obviously, the transferred energy increases the temperature of the electrons in the plasma.
Currently, ASDEX Upgrade operates with 8 gyrotrons in routine operation. These gyrotrons are step-tunable and capable of working at both 105 and $140GHz$ frequencies. They offer output powers of up to $1MW$ at $140GHz$, while the output power is slightly reduced at $105GHz$. The maximum pulse length achievable with these gyrotrons is $10s$, which corresponds to the maximum flat top pulse length of the tokamak;

- Ion Cyclotron Resonance heating (P_{ICR}). Unlike electron cyclotron resonance heating, which heats the electrons in the plasma, ICRH is designed to heat the ions within the plasma. The concept is basically the same as described for the electrons, the most important consideration relies in the fact that the wavelengths considered now are different from electron case.
ICRH systems are designed to launch electromagnetic waves, typically in the radiofrequency range, whose frequency matches the ion cyclotron frequency of the desired ions within the plasma. A very particular thing is that ICRH is selective in terms of which ions it heats. In fact, the resonant absorption occurs primarily for the ions that have a cyclotron frequency close to the frequency of the injected waves, but different ions have different ion cyclotron frequencies due to their mass and charge. As a result, ICRH can be tuned to selectively heat specific ion species within the plasma. Four generators were installed and each generator is connected, via transmission lines, an impedance matching network, and a vacuum insulated feeding line to an antenna. The generators cover a frequency range of 30 to $120MHz$. This allows, among others, H minority heating at $2T$, He_3 minority heating at $3T$ and second harmonic H heating at the highest field. In Fig.(19) is shown the model of a ICR antenna, used to heat the plasma during the discharges:

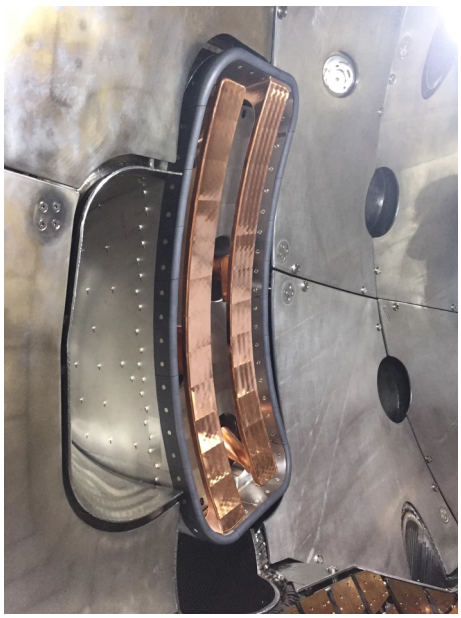

Figure 19: ASDEX Upgrade ICRH antenna.

In Fig.(20), the power transfer systems for ASDEX Upgrade are schematically depicted from a top-down perspective.

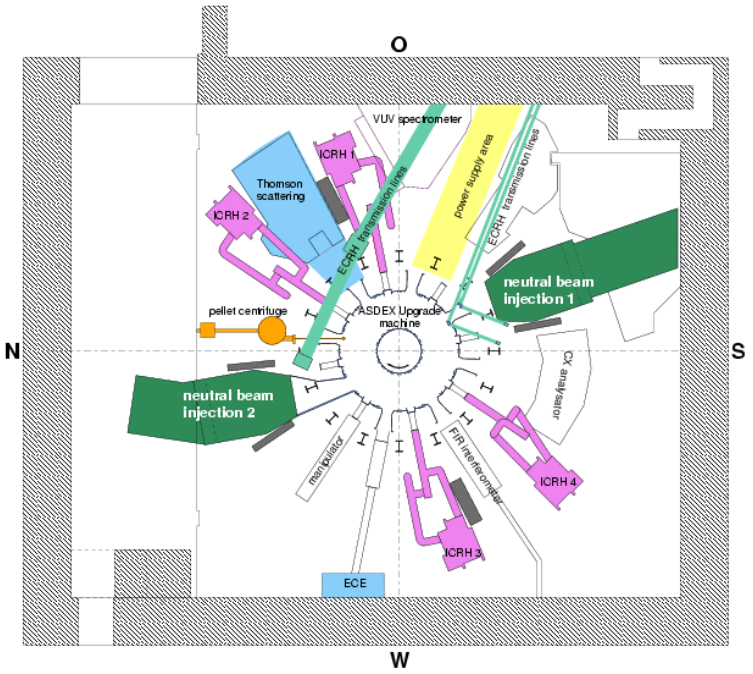

Figure 20: ASDEX Upgrade plasma heating systems depiction.

The power supply to the plasma is determined through the various listed systems and must adhere to what is specified by Eq.(14). To ensure the correct conditions, the power radiated and lost must be compensated for properly by the power transmitted by the various systems. In Fig.(21), the trends of power related to the plasma supply systems and the radiated power from the plasma are shown.

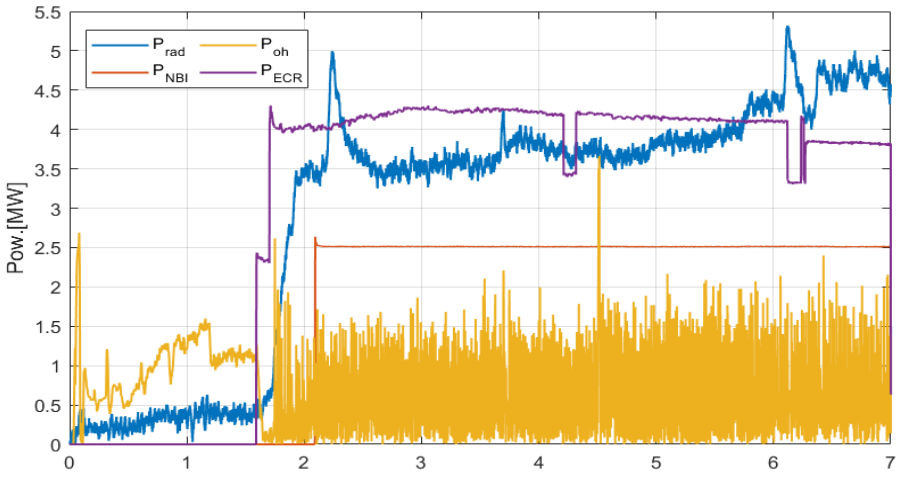

Figure 21: ASDEX Upgrade plasma power trends.

Plasma can experience various instabilities such as MHD (Magnetohydrodynamic) instabilities, like kink modes, tearing modes, and disruptions. These instabilities can cause fluctuations in the plasma current and pressure, which, in turn, affect the ohmic heating power, resulting in that oscillatory trend. Also variations in the plasma density and temperature can lead to fluctuations in the resistivity of the plasma, which inluencing the ohmic heating power.

2.5.3 Divertor and LMD configuration: Future applications

Since 2014 a new version of divertor has been used, known as DIM-III, where tungsten-plated carbon tiles in the lower divertor region has been replaced by solid tungsten tiles of the DIM-II. Nowadays, the divertor in AUG consists of 128 tiles, including the 2 in the DIM, each with dimensions of $229mm \times 75mm \times 15mm$ and made of solid tungsten. Always in 2014, a divertor manipulator has been installed, to replace parts of the lower divertor in between two plasma discharges. In this thesis, reference is made to a classic configuration known as the *Lower Single Null* divertor configuration (LSN), even though, in recent years, there has been consideration of an approach that includes an upper divertor (*Double Null configuration*) with the aim of mitigating the power exhaust problem.
The anticipated requirement to manage higher thermal loads than those encountered in current experimental reactors has prompted the development of alternative divertor configurations. These configurations aim to more effectively manage the deposited energy load by incorporating extra layers of material or by extending the area exposed to particle flow. One of the most promising and extensively studied configurations for future applications is the Liquid Metal Divertor (LMD).
LMDs offer innovative solutions to several challenges faced by fusion reactors, notably in enhancing the durability and efficiency of plasma-facing components. The unique attribute of LMDs lies in their ability to circumvent the typical thermo-mechanical failures—such as erosion, macro-cracking, melting, and embrittlement—commonly associated with solid divertors. This is achieved through a dual cooling mechanism that fundamentally changes how heat from the plasma is managed.
At the heart of this system is the process whereby the liquid metal, upon absorbing heat from the plasma, enters a phase of evaporation. This phase change plays a pivotal role in temperature regulation, as the evaporated particles interact with the plasma's ions and electrons, effectively reducing its overall temperature. Following this, the vapor recondenses, returning to a liquid state and flowing back into a specifically designed reservoir. This reservoir, integral to each cassette within the divertor, ensures a consistent supply of liquid metal, which is then heated to maintain its fluidity.
The cycle of evaporation and condensation introduces two critical cooling mechanisms to the LMD system: evaporative cooling and vapor shielding. These mechanisms create a protective particle cloud at the divertor's interface, which serves not only as a thermal buffer but also as a self-regenerating shield, theoretically negating any net erosion of the divertor surface.
An ingenious aspect of the LMD design is its passive liquid metal replenishment system, which leverages capillary action. This system is adept at counterbalancing the magnetic JxB forces (generated by the interactions between the current and magnetic field) that could

otherwise draw metallic components into the reactor's core plasma, potentially disrupting its operation. A paramount challenge in the deployment of LMDs is ensuring that liquid metal particles, whether as droplets or vapor, do not infiltrate the core plasma, leading to contamination. Unrecondensed particles could migrate to the Scrape-Off Layer (SOL) and the core, potentially inducing significant radiation and risking the reactor's shutdown. This issue, termed plasma contamination, is especially concerning with high-Z impurities, which could remain partially ionized and dissipate energy via both line radiation and Bremsstrahlung.
Equally critical is preventing plasma dilution, which occurs when the accumulation of impurity ions diminishes the concentration of main plasma ions, a condition necessary to maintain plasma quasi-neutrality. Dilution, primarily associated with low-Z impurities like helium ashes, hinges on the concentration of these impurities within the plasma.
Balancing the intricate dynamics of dilution and contamination represents a significant engineering and operational challenge within the LMD framework. Lithium and Tin are among the liquid metals under consideration for their favorable properties in addressing these challenges, marking a promising direction in the evolution of fusion reactor technology.

The key challenge with liquid metal lies in maintaining its stability and preventing splattering. This can be achieved by employing a *Capillary Porous Structure (CPS)*.
CPS utilizes significant surface tension to stabilize and facilitate the flow of the liquid metal through the porous mesh. These tension forces also serve as a capillary pump for replenishing the liquid metal, enabling comprehensive coverage of the PFC while minimizing the risk of splashing and droplet formation. This approach provides the capability to refresh the surface. The thickness of the liquid metal film coating the porous matrix remains subject to investigation, considering liquid metal properties, operational conditions, and mesh topography. From a general perspective, various materials are currently being considered as the primary substrate material due to their corrosion resistance and compatibility with liquid metal. It is crucial to emphasize that the underlying substrate may be exposed to plasma due to the breakdown of the liquid layer. It's important to note that while the CPS concept shows promise in terms of its relative ease of implementation and testing, there is still limited understanding of its power handling capabilities, especially during transient events, and its role in vapor shielding. Presently, heat conduction to the substrate alone is insufficient for power dissipation, and hybrid systems (like CPS) incorporating conduction, evaporative cooling, and plasma radiation are required. The decision regarding which liquid metal to use was narrowed down to tin and lithium: Both of them present a low melting point (180.5^oC and 231.9^oC). Concerning the primary substrate material, Tin is compatible with tungsten but incompatible with other choices like steel and molybdenum (above $1073K$). Tin's operational range is significantly broader due to its lower vapor pressure at a given temperature, enabling higher heat loads on the surface. However, the primary appeal of liquid tin lies in its low hydrogen retention. Despite its advantages, tin has lower wettability compared to lithium and it has been observed that oxide reduction is necessary to enhance the wetting characteristics of tin when integrated into CPS systems. Nevertheless, lithium displays higher reactivity and a higher vapor pressure, making tin the superior choice for this case.
The use of a liquid metal presents several complications, including the risk of excessive tin deposition rates on plasma-facing surfaces in AUG. To mitigate the consequences of liquid

metal layer formation, the amount of tin used during the experiment is minimized while ensuring that the dimensions of the Plasma-Facing Component (PFC) are sufficiently large. Overall, the PFC design has been optimized to reduce splashing.

The text demonstrates a potential application of future simulation with the impurities. The reference is to an experiment conducted on ASDEX Upgrade and published as "Performance of a liquid tin divertor target during ASDEX Upgrade L and H-mode operation" by J.G.A. Scholte and B. Boeswirth [11]. In this study, a tin CPS (Capillary Porous System) module is applied at a well-defined toroidal position, and a discharge is executed. The geometry and dimensions of the component are listed in tab.(3) and depicted in fig.(22):

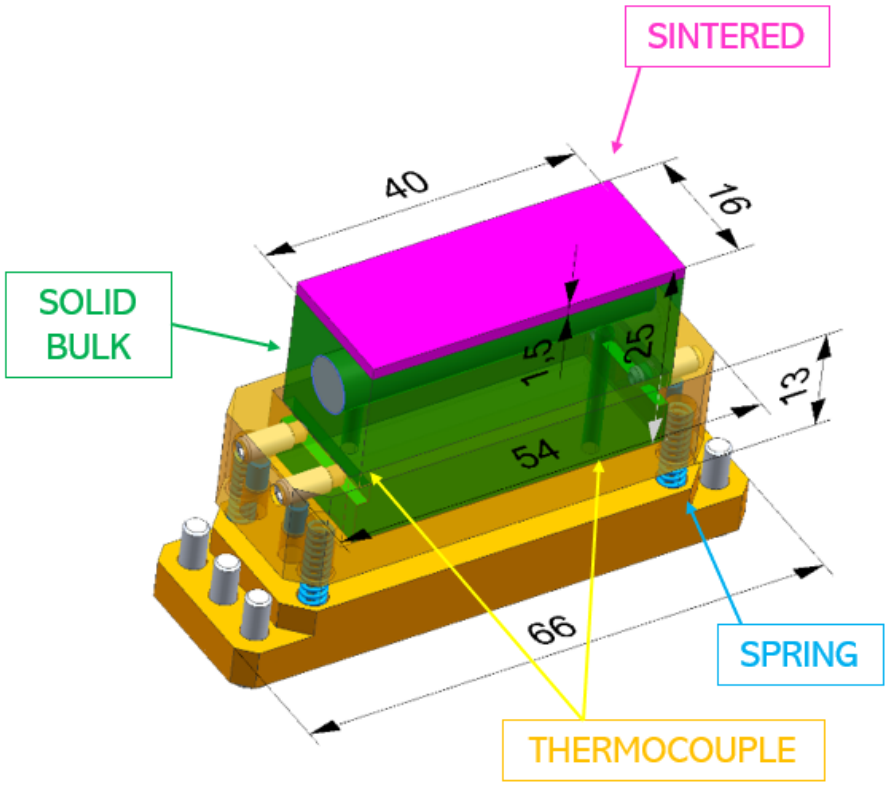

Figure 22: CPS Mockup configuration. Presentation: "Performance of a liquid tin divertor target during ASDEX Upgrade L and H-mode operation", authors: "J.G.A. Scholte, B. Boeswirth"

Mockup dimensions	**value**
Length	40 mm
Width	16 mm
FW thickness	1.5 mm
Solid bulk thickness	25 mm

Table 3: Mockup dimensions

In the course of this experimental campaign in AUG, $20mg$ of tin are introduced into the vessel through sputtering, primarily due to impurities within the plasma. The quantity of tin entering the vessel through evaporation is notably influenced by the surface temperature of the liquid tin. Indeed, to minimize substantial evaporation, during the experimental campaign in AUG has been calculated that the target temperature should not exceed $1300K$. It's important to note, however, that in order to maintain the liquid state, the metal needs to be in contact with a heater capable of keeping the metal temperature sufficiently high during the initial phases of the discharges to enable proper functionality. Additionally, it's worth mentioning that the CPS is consistently cooled by a cooling circuit with 20^oC water. Therefore, it is crucial to maintain reasonable thermal conditions for all the environments under consideration.

The CPS is secured onto a tray and spring-loaded against the plasma-facing surface. The alignment can be fine-tuned using a set of four height-adjusting screws. The system is attached to the DIM-III using a backplate and six screws. To properly fit the CPS to the target holder, a thickness of $25mm$ is required and the lower section can be constructed from non-porous tungsten to minimize the Sn accumulation within the CPS. A heater is positioned between the tray and the backplate to ensure a liquid Sn surface before the plasma discharge. Between the tray and the backplate, a heater will be positioned. Additionally, three thermocouples will be attached to the CPS: one inserted in the near-surface volume of the CPS matrix, one inserted near the bottom of the CPS matrix, and one connected to the heater.

The witness plates and divertor tiles are composed of *Molybdenum-Titanium-Zirconium-Carbon alloy* (TZM), and liquid tin is exclusively contained within the CPS. Fig.(23) is a zoom-in on the CPS location area, providing an idea of the dimensions between the bottom of the chamber and the study element.

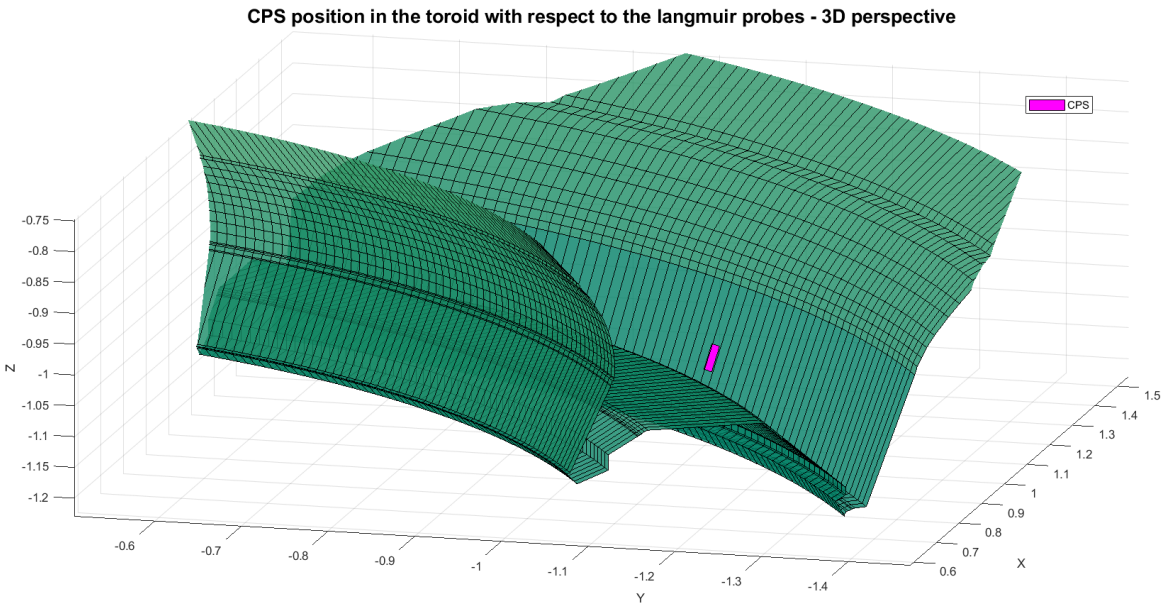

Figure 23: CPS position representation in the toroid. From "Performance of a liquid tin divertor target during ASDEX Upgrade L and H-mode operation", authors: "J.G.A. Scholte, B. Boeswirth"

3 3D Simulation Methodologies and Finite Element Grid Preparation

Direct experimentation on an experimental nuclear reactor involves numerous constraints and difficulties that make simulations a preferable choice in various contexts:

- Cost and efficiency: Constructing and operating an experimental nuclear reactor is extremely expensive and resource-intensive. Simulations, on the other hand, can be conducted on computers using mathematical models and initial data, which are much more cost-effective and efficient compared to building and operating a physical reactor;
- Safety: Managing an experimental nuclear reactor involves significant safety risks. Simulations allow for virtual experiments without any safety hazards to people or the environment. Additionally, simulations can be used to study extreme or emergency scenarios that may be dangerous or impractical to replicate in a physical reactor;
- Control and repeatability: Simulations provide a high level of control over the simulation environment, allowing for parameter variation and repeatable experiments under controlled conditions. This facilitates systematic study of phenomena and enables isolation of specific effects or variables of interest;
- Access to internal information: During a simulation, detailed information about the internal behavior of the plasma and its parameters can be obtained, which may not be directly observable in experiments. This allows for in-depth analysis of the system and a more comprehensive understanding of the underlying physical processes;
- Exploration of future scenarios: Simulations allow for the exploration of future scenarios and testing of different design or control options without having to wait for the construction and operation of a physical reactor. This enables rapid evaluation of performance, efficiency, and safety of new ideas or concepts, guiding the development of nuclear technology;

It is important to note that simulations do not completely replace physical experimentation, and simulation results need to be validated and compared with experimental data to ensure the reliability of the models. However, simulations provide an important tool for study, design, and analysis in the field of nuclear fusion, allowing for significant progress to be made before moving on to direct experimentation on experimental reactors.
Concerning the plasma simulation there are different codes used to perform simulations, such as *EMC3-EIRENE* and *SOLPS-ITER*. They are both computer codes used for simulating plasma behavior in fusion devices, specifically in the edge and scrape-off layer regions. While they serve a similar purpose, there are differences between them in terms of their underlying models and capabilities.
SOLPS-ITER is a package of computational codes used for simulating the plasma boundary region in tokamaks and it is a specialized tool developed to support the design and operation of the ITER (International Thermonuclear Experimental Reactor) project. It primarily focuses on simulating the behavior of the plasma in the boundary region of the tokamak,

aiming to predict plasma-surface interactions, particle and energy transport, plasma detachment, and the behavior of the plasma boundary. The SOLPS plasma boundary code package combines the 2D multi-fluid plasma transport code B2 or B2.5 with the 3D kinetic Monte Carlo neutral transport code EIRENE, hence it uses primarily a two-dimensional approach, simulating the plasma behavior in the poloidal plane (X-Y plane) of the tokamak [17]. While the tokamak plasma is inherently three-dimensional, the 2D approach simplifies the computational complexity and allows for efficient simulations of the plasma boundary region. However, SOLPS-ITER may incorporate simplified modeling or assumptions to account for certain toroidal effects.
SOLPS-ITER is widely preferred over EMC3 for modeling liquid metal divertors, providing a much broader knowledge base and extensive usage information. However, it presents a significant inconsistency regarding the main topic addressed in this thesis: being primarily a 2D code, it fails to capture the effects of toroidally localized Sn vapor shielding, necessitating a 3D representation and therefore the use of EMC3-EIRENE.

3.1 EMC3-EIRENE code - the Fluid & Kinetic model

EMC3-EIRENE is a computer code that combines the capabilities of two separate codes, *EMC3* and *EIRENE*, to simulate plasma behavior and plasma-surface interactions in fusion reactors.
By combining these two codes, it allows researchers to study not only the behavior of the plasma itself but also its interactions with the reactor walls and other components. It ensures to model the behavior of plasma in types of fusion reactors, including tokamaks and stellarators and allows researchers to test different reactor designs: allows modeling of the plasma edge in non-axisymmetric configurations, predict the performance of different materials used in the reactor walls, and optimize the plasma-surface interaction to improve reactor efficiency and safety.
It was originally developed to study stellarator geometries of W7-AS and W7-X[5]. Since EMC3-EIRENE is a combination of these two codes, both of them utilize *Monte Carlo methods* methods and operate on a 3D finite flux tube grid to enable rapid field line reconstruction. As a result, plasma and neutral gas data are provided for each cell. In particular:

- EMC3, or *Extended Magnetohydrodynamic Code* 3D, is a 3D computer simulation code used to study the behavior of plasma inside a nuclear fusion reactor, with a focus on analyzing the interaction between the plasma and magnetic fields. The code takes into account several key physical phenomena such as conduction, diffusion, convection, the Hall effect, current drive, particle transport, and ionization. It is defined as a fluid code, therefore it solves a set of Braginskii steady-state balance equations for particles, parallel momentum, and energy of the main plasma species (ions and electrons), and includes a reduced model for trace impurities. Along magnetic field lines, the code assumes classical transport, while "anomalous" cross-field transport is taken into account by free user parameters such the particle transport $D_\perp$ and the heat transport coefficients $X_\perp$[9][10]. EMC3 is primarily written in *FORTRAN 90*, a programming language designed for scientific and engineering applications (extension of the earlier

FORTRAN language, includes features such as array operations, dynamic memory allocation, and modular programming). It also uses the Message Passing Interface (MPI) standard for communication between different processors, allowing it to run in parallel on multiple computers. Parallelization of the code is necessary due to the large computational requirements of simulating 3D plasma behavior. Additionally, EMC3 incorporates the Python programming language for pre- and post-processing tasks such as visualization of simulation results.

- Neutral particle densities and the source terms in the plasma balance equations resulting from interactions with neutral particles, such as ionization and charge exchange, are computed by the EIRENE code and it utilizes a combinatorial discretization method for general 3D computational domains. The EIRENE neutral gas transport Monte Carlo code has been developed initially for TEXTOR since the early 1980s[6]. It is a multi-species code that solves a system of linear or nonlinear kinetic Boltzmann transport equations, of almost any complexity, simultaneously in a time-dependent (optional) or stationary (default) mode. A simplified model for ionized particle transport along externally specified magnetic field lines is also incorporated. EIRENE is linked to external databases containing atomic and molecular data, as well as surface reflection data, and calls on various user-supplied routines, such as data exchange with other (fluid) transport codes. The primary objective of code development was to create a tool for investigating neutral gas transport in magnetically confined plasmas[10][12]. EIRENE, as well as EMC3, is primarily written in Fortran 90, which is particularly well-suited for scientific applications due to its efficient handling of mathematical operations and its ability to easily work with arrays and matrices. The code also includes some elements written in C/C++.

In summary, it is possible to use two different equations for regulating particle flows in the plasma SOL, one concerning the motion of charged particles (Eq.(60)) in the plasma and the other regarding the treatment of neutrals (Eq.(61)). It is evident that, due to ionization and recombination phenomena, particle flows tend to change continuously, resulting in both negative and positive values depending on the perspective.

$$\Gamma_{Fuel.P} + \Gamma_{Ion} = \Gamma_{Target} + \Gamma_{Vol.Rec.} \tag{60}$$

$$\Gamma_{Recy.} + \Gamma_{Fuel.N} + \Gamma_{Vol.Rec.} = \Gamma_{Pump} + \Gamma_{Ion} \tag{61}$$

With $\Gamma_{Fuel.P}$ the particle flux of fuel, Γ_{Ion} the particle flux of other ions, Γ_{Target} the particle flux directed towards the target or plasma-facing components, $\Gamma_{Vol.Rec.}$ the volumetric recombination particle flux, $\Gamma_{Recy.}$ particle flux of recycled neutrals, $\Gamma_{Fuel.N}$ the particle flux of fuel neutrals and Γ_{Pump} particle flux pumped out of the system.

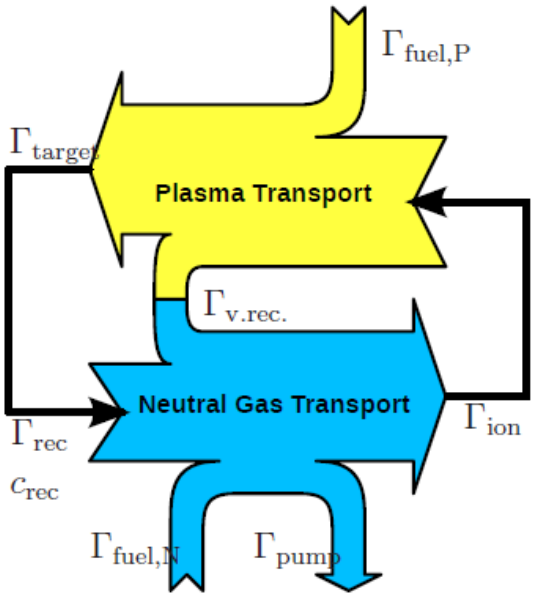

Figure 24: Representation of the involved fluxes shown in Eq.(60) and Eq.(61) of EMC3-EIRENE.

Considering what has already been mentioned, EMC3 and EIRENE refer to problems of different nature, and therefore, they approach simulations with different models: the *fluid model* and the *kinetic model*. The difference between a fluid model and a kinetic model lies in the approach used to describe the behavior of a physical system, such as a plasma. Fig.(25) schematically illustrates how EMC3-EIRENE operates and the type of domain it performs on concerning a poloidal section of the tokamak.

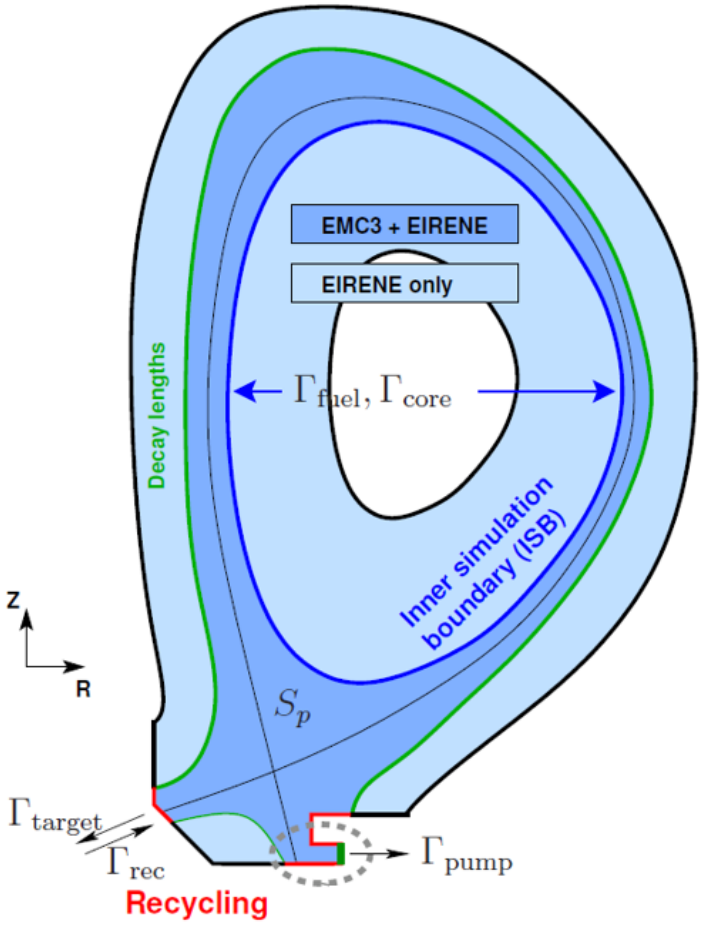

Figure 25: Representation of the operating domain of EMC3-EIRENE.

A fluid model considers the plasma as a continuous medium, approximating the collective behavior of the particles within it. In a fluid model, macroscopic quantities such as density, velocity, and temperature of the plasma are defined, and balance equations are applied to describe the conservation of mass, momentum, and energy. These equations, such as the Navier-Stokes equations for classical fluids, allow us to study the evolution of the plasma (with the Braginskii fluid equations form) in time and space. Fluid models are generally simpler and computationally less intensive compared to kinetic models, but they may overlook certain microscopic details of the plasma.

On the other hand, a kinetic model describes the plasma by considering the individual behavior of the constituent particles. This type of model is based on the velocity distribution of the particles and takes into account the effects of collisions and interactions between particles. In a kinetic model, the Boltzmann equation or a similar kinetic equation is solved to determine the evolution of the particle distribution function in time and space. This allows for more detailed information on the microscopic properties of the plasma but requires more calculations and higher computational complexity.

Both approaches, fluid models and kinetic models, are used in plasma physics depending on the context and objectives of the simulation. Fluid models are often employed for large-scale studies where the average properties of the plasma are important, while kinetic models are used to investigate specific details such as velocity distributions and collisional interactions between particles.

The EMC3 code primarily utilizes a fluid model to simulate the behavior of plasma in fusion reactors. The set of time-independent Braginskii fluid equations for the plasma edge it solves is based on the fluid approximation and describes the **macroscopic properties** of the plasma such as density, temperature, and velocity. However, it's worth noting that EMC3 also includes a reduced model for trace impurities, which can introduce some elements of kinetic effects related to impurity transport. Overall, while EMC3 is predominantly based on a fluid model, it may incorporate certain aspects of kinetic behavior depending on the specific features being simulated.

The EIRENE code primarily utilizes a kinetic model to simulate the behavior of plasma in fusion edge and divertor regions. It solves a system of time-dependent or stationary linear or nonlinear kinetic transport equations. These equations describe the behavior of **individual particles** in the plasma, taking into account collisional interactions and various physical processes such as ionization and charge exchange. EIRENE considers the distribution of particle velocities and includes detailed calculations for particle transport and interactions. It is important to note that it also includes certain fluid approximations for ionized particle transport along externally specified magnetic field lines. Additionally, EIRENE can be coupled with other transport codes and databases, this enables a comprehensive analysis of neutral gas transport in magnetically confined plasmas.
As described in Eq.(39), the equations of the fluid model can be derived from the kinetic equations through the local equilibrium distribution approximation and other simplifications. It's possible to claim that the fluid model conceptually derives from the kinetic model but involves simplifications that make the system of equations more manageable and suitable for large-scale simulations. The fluid model is capable of providing an accurate description of the plasma in many situations but may not fully capture the microscopic details of individual particles. On the other hand, the kinetic model is more detailed and precise but requires more computational resources and can be more complex to implement. The choice between the kinetic model and the fluid model depends on the specific requirements of the simulation and the scale of interest.

EMC3 adopts a finite-volume method to discretize the computational domain. This approach involves dividing the three-dimensional space into a grid of cells, where each cell represents a small volume element. The grid is typically structured, meaning that it follows a regular pattern, such as a Cartesian or cylindrical coordinate system.
In the case of EMC3, the computational domain is discretized using a 3D finite flux tube grid. This grid is constructed by tracing field lines starting from a 2D base grid at a fixed toroidal position. The determination of the toroidal range for the computational domain is crucial and depends on the symmetry of the machine and the plasma scenario. It is worth noting that, typically, to reduce computation times and save computational costs, the

toroidal angle set to construct the entire three-dimensional figure is never set at 360°. Instead, a smaller angle (e.g., 120^o) is chosen. To maintain consistency with the phenomenon, boundary conditions are imposed, ensuring that the last poloidal section created exhibits the exact conditions and physics as the first one, such as the density and the temperature (whatever exits toroidally from the last surface enters in the first and viceversa). Fig.(26) displays an example of the 2D grid set at a toroidal angle of 20^o.

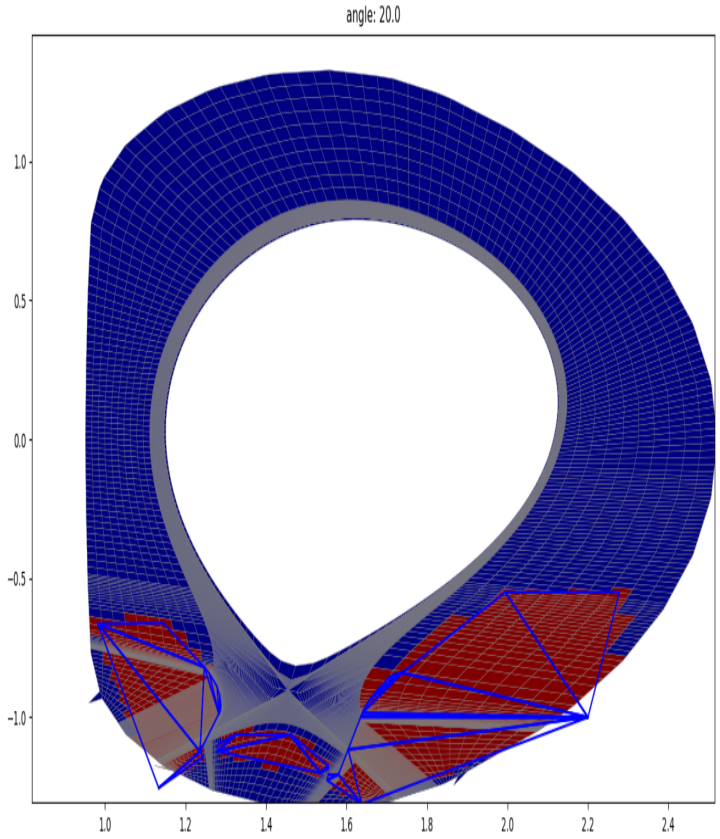

Figure 26: Representation of the 2D base grid at 20^o. Blue lines are used to highlight roughly the inner and outer target and the central dome.

The domain is then divided into several toroidal blocks, each with a size of $\Delta\Phi_{region} = \Delta\Phi_{tot.}/N_{tor.}$, where $\Delta\Phi_{tot.}$ represents the total poloidal area and $N_{tor.}$ is the number of toroidal blocks. Within each toroidal block, there is a block-structured decomposition of the 2D base toroidal grid which allows for varying resolutions in the radial ($N_{rad.}$) and poloidal ($N_{pol.}$) directions.
To ensure a smooth transition between blocks, a condition known as $N_{pol.}^{SOL} = N_{pol.}^{CORE} + N_{pol.}^{PFR}$ must be satisfied, ensuring a continuous transition between the SOL, core, and private flux regions.
Once the grid is established, EMC3 proceeds with the simulation by solving the fluid equations within each cell of the grid. The fluid equations describe the transport and behavior

of plasma quantities, such as density, temperature, and velocity, in a continuum approximation. These equations are solved numerically using iterative methods, taking into account the relevant physical processes and boundary conditions.
By discretizing the domain in this manner, EMC3 is able to capture the spatial variations of plasma properties and simulate the complex behavior of the plasma in a fusion reactor.

3.2 The Monte Carlo method

As explained in the previous section 3.1, EMC3 and EIRENE utilize the Monte Carlo method. This is a computational technique used to simulate a wide range of phenomena in various fields, including physics, engineering, finance, and more. The method involves the use of random sampling and statistical analysis to solve complex problems or estimate numerical solutions. It involves generating a large number of random samples to simulate a problem, then using statistical analysis to draw conclusions about the problem's behavior or characteristics. For example, in a physics simulation, the method could be used to calculate the behavior of particles in a system, such as the interactions between particles in a plasma. It is a versatile and powerful tool, capable of solving a wide range of complex problems and is often used in situations where analytical solutions are not feasible or where approximations are required. It is based on the principle of statistical sampling, which involves repeatedly generating random sample (iterative process) from a probability distribution and using them to estimate the behavior of a system, the results of the simulation can then be analyzed statistically to draw conclusions. The process typically involves the following steps:

- Define the problem and identify the relevant parameters and variables;
- Define a probability distribution for each parameter or variable, which specifies the likelihood of different values occurring;
- Generate a large number of random samples from these probability distributions;
- Use these samples to estimate the solution of the problem, by simulating the behavior of the system under each set of sample values;
- Analyze the results to estimate the expected value and variability of the solution;
- Repeat the process with a larger number of samples, or with refined probability distributions, until the desired level of accuracy is achieved;

The iterative process of the Monte Carlo method is based on the law of large numbers, which states that as the number of samples increases, the estimates will converge towards the true solution of the problem.
When using a program like EMC3-EIRENE, designed to model the edge of the plasma and its interactions with the walls of a tokamak, the Monte Carlo method in EMC3 (Edge Monte Carlo 3D) is integrated to enhance the precision of simulations. In particular it's useful to for:

- Transport of Neutral Particles through the Plasma Edge. In the plasma edge of a tokamak, understanding the transport of neutral particles is crucial. These neutrals may be generated through nuclear fusion reactions or ionization processes at the plasma edge and the Monte Carlo method can be applied to track the transport of these neutral particles through the plasma edge. By using it, it's possible to simulate the interactions of neutral particles with the plasma, including processes like scattering, ionization, and energy loss. This provides a detailed insight into the behavior of neutral particles and their interaction with the plasma edge and tokamak walls;

- Interactions Between Charged Particles and Tokamak Walls. Charged particles in the plasma edge can interact with the tokamak walls and these interactions involve impact, reflection, or absorption of particles on the walls. The Monte Carlo method can be utilized to model these interactions, simulating the motion of charged particles through the plasma edge and their interaction with the walls allows obtaining information on energy distributions, particle loss to the walls, and other crucial aspects for the design and optimization of the tokamak;

- Optimization of Model Parameters. The use of the Monte Carlo method provides flexibility in optimizing model parameters, such as parameters related to particle collisions, tokamak geometry and wall characteristics;

Taking into account the extended form of the Fokker-Planck equation Eq.(39), a more general version, used for simplicity by EMC3-EIRENE in the model, is proposed:

$$\frac{\partial}{\partial t}F + \nabla \cdot [VF + \nabla \cdot DF] = S \tag{62}$$

With F is the distribution function of particles in the plasma, V is the drift term, accounting for the mean motion of particles under the influence of magnetic fields and forces. D is the diffusion term, describing the scattering and diffusion processes of particles in the plasma. S is the source/sink term, representing any processes of particle generation or loss. This equation is related to the stochastic process and specifically, it is considered the motion of fluid particles along field lines from a source to a sink. The motion of simulation particles is determined by the coefficients V and D and by a numerical time step τ, through an equation along field lines:

$$\Delta I_{\parallel} = V_{\parallel}\tau + \sqrt{2D_{\parallel}\tau\xi} \tag{63}$$

Where $\Delta I_{\parallel}$ represents the change in the parallel action of the particles along the field lines. $V_{\parallel}$ is the parallel component of the drift term. $D_{\parallel}$ is the parallel component of the diffusion term. ξ is a random variable with the properties $\langle\xi\rangle = 0$ and $\langle\xi^2\rangle = 1$, indicating that it follows a Gaussian distribution. This equation suggests that the change in the parallel action is influenced by the deterministic drift term ($V_{\parallel}\tau$) and a stochastic term ($\sqrt{2D_{\parallel}\tau\xi}$), which introduces randomness in the particle motion along the field lines. These equations are uses to iteratively update the position of simulation particles, considering both deterministic and stochastic components, following these particles from the source to the sink.

3.3 Simulation Set-Up

The use of mesh in computational models for plasma studies, particularly in areas such as the Scrape-Off Layer (SOL), the private zone, and partially in the core, is crucial for understanding and predicting plasma behavior in these regions within fusion devices like tokamaks or stellarator fusion reactors. These meshes, or grids, allow for the discretization of the plasma domain into smaller elements over which physical equations can be applied, thus facilitating numerical analysis.
The SOL is the region of the plasma that directly borders the walls of the fusion device. In this area, heat and particle management is critical for the longevity and efficiency of the reactor. Using a mesh in this area allows for precise modeling of temperature and density gradients, as well as particle flows towards the walls. The mesh can help predict heat accumulation and potential areas of wall damage, enabling engineers to design more effective cooling systems and more resistant wall materials.
The private zone is the area located behind the limiters or divertors, separated from the main plasma core. It is a critical region for impurity control and for exhausting heat and particles from the plasma. Using a mesh here allows for the study of complex particle transport and recombination phenomena, providing crucial data for optimizing divertor design and improving the efficiency of impurity capture and heat exhaust.
Implementing a mesh in these domains requires careful design to balance the necessary resolution with available computational resources. Finer meshes are desirable for capturing fine details of physical phenomena but significantly increase computational cost. Techniques like adaptive mesh refinement, where the mesh is automatically made finer in regions with high gradients of physical properties and coarser where the plasma is more homogeneous, are often used to optimize this trade-off.
In the following images, the method for constructing the two-dimensional EMC3 mesh associated with the poloidal section will be shown:

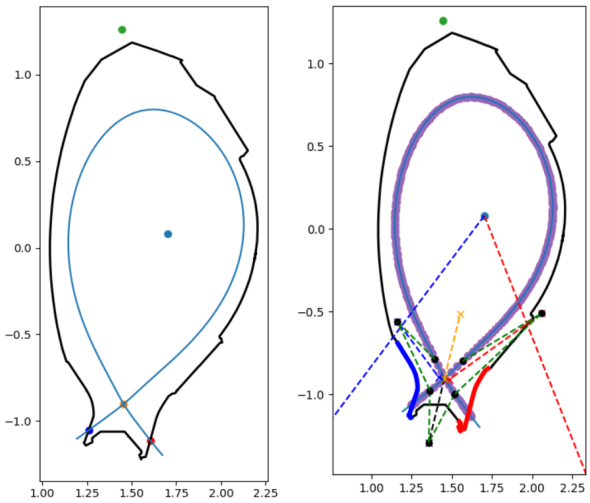

Figure 27: Representation of the progressive construction of the two-dimensional mesh.

Starting from the main points (Null points, X points, and the contact points with the

target), the process continues with the tracing of some lines to define the contour areas of the core, SOL, and PFR. Once the boundaries are defined, the mesh is compiled by defining a network of elements, distinguished by color according to the region (red for the CORE, blue for the SOL, green for the PFR).

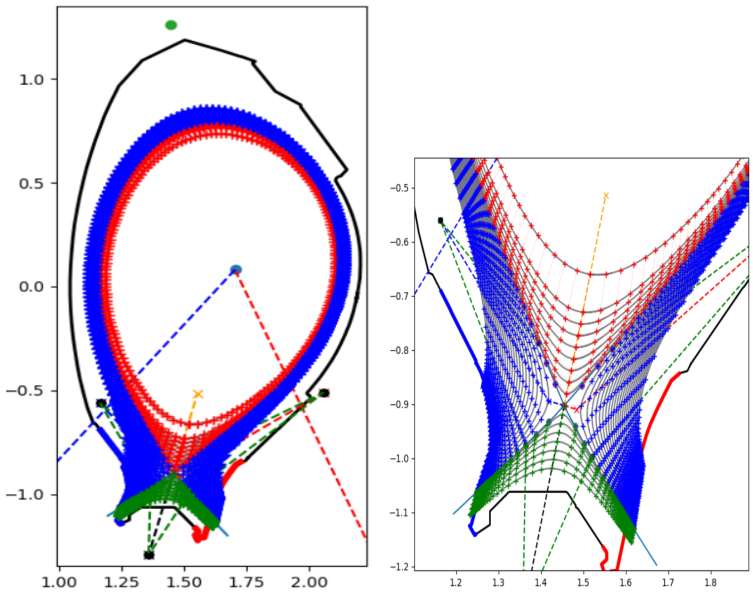

Figure 28: Representation of the final two-dimensional grid for EMC3, with a closer sight on the X-point.

Fig.(29) proposes the mesh associated with the calculation performed by EIRENE, the EIRENE grid is comprised of triangles aligned to the EMC3 grid.

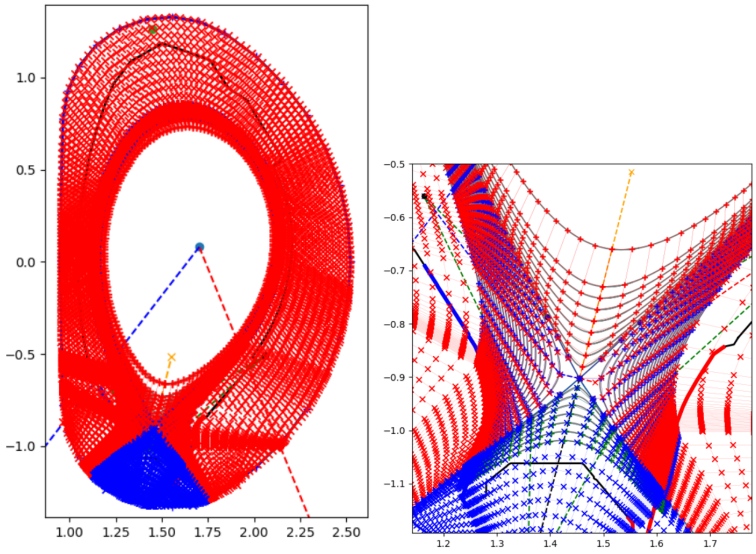

Figure 29: Representation of the final two-dimensional grid for EIRENE, with a closer sight on the X-point.

4 Data Organization for Simulation

To ensure that the simulations accurately capture the plasma behavior, it is necessary to initialize the code with the appropriate experimental data. Proper utilization of this data allows the simulation to provide a representation that closely aligns with the physics of the phenomenon, ensuring the development of a useful predictive model for analysis. The spatial and temporal profiles used were obtained from the IPP Garching databases, associated with ASDEX Upgrade diagnostics, incorporating tools as *ISIS*, *cview*, *Diaggeom*, *Augped*, *Lang*).

The reference situation considered was discharge #41273, which occurred on Tuesday, June 28, 2022, at 11:03:21 AM in ASDEX Upgrade. This was one of the key shots of the experimental campaign developed by J.G.A. Scholte and the geometrical configuration and purposes were already described in Chapter 2.5.3. Although the situation described by the experiment presents impurities and thus paints a scenario different from the one intended in our simulation, the technical characteristics of the discharge can be maintained even in the pure deuterium simulation. This is due to the fact that the technical characteristics are inherent to the machine's configuration and are independent of how the impurities spread by the individual module interact with the plasma. Therefore, they can be considered as parameters for our simulation. A summary table of the main characteristics is presented in Tab.(4).

# shot	$B_t[T]$	$I_P[Ma]$	$q95$	$P_{aux.}[MW]$	gas	Behaviour
41273	-2.504	0966	4.146	NI 2.638 - EC 4.334	D	plasma

Table 4: : Shot 41273 characteristics

4.1 Correlation CECE diagnostic

Correlation Electron Cyclotron Emission (CECE) is a diagnostic technique based on radiometry that is routinely employed to assess long-wavelength, wide-spectrum turbulent fluctuations in electron temperature within the core plasma at ASDEX Upgrade. Developed and installed through a collaborative effort with MIT, the CECE diagnostics in AUG are capable of measuring second harmonic X-mode polarized electron cyclotron emission. In the context of fusion experiments, X-mode polarized electron cyclotron emission is a specific type of radiation produced by the motion of electrons in a magnetic field: the "second harmonic" indicates that the diagnostic system is tuned to a specific frequency or energy level of this radiation, while the polarization describes the orientation of the electromagnetic waves, which can be important for measurements.
In cases where the plasma is optically thick (when radiation produced within the plasma doesn't get absorbed or blocked by the plasma itself but can freely escape) and not cut-off (diagnostic system is not hindered by the plasma in such a way that it can still receive the radiation), the measured emission can be effectively used to determine the electron temperature.
CECE serves as a robust diagnostic tool for studying turbulence. It offers a localized assess-

ment of turbulence levels and provides an absolute measurement of the percentage fluctuation in electron temperature. However, it is crucial to exercise caution when dealing with CECE data and to interpret it diligently, much like other diagnostic systems such as CXRS (Charge Exchange Recombination Spectroscopy) and Doppler reflectometry.
In Fig.(30) is presented a block diagram showing basic layout of the CECE diagnostic:

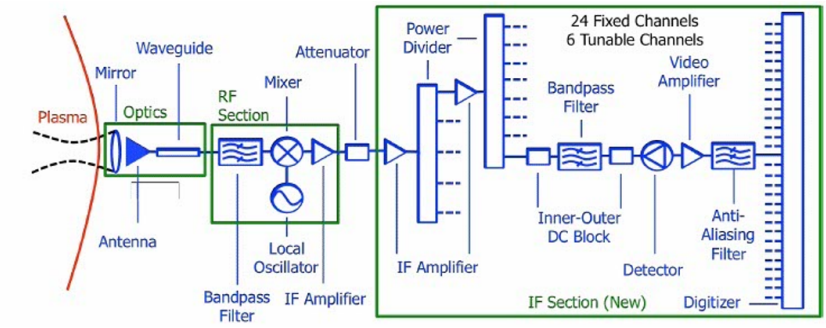

Figure 30: CECE system scheme

In summary, CECE operates by measuring electron cyclotron radiation in the plasma and analyzing correlations in these measurements to deduce electron temperature. This temperature is a key indicator for understanding plasma behavior in nuclear fusion experiments conducted at facilities like ASDEX Upgrade.

4.2 ASDEX Upgrade Doppler reflectometry

Microwave Doppler reflectometry is a diagnostic method with the ability to directly assess several critical aspects of plasma behavior in fusion experiments. This technique provides valuable insights into the radial electric field (Er) profile, the radial shear within Er, as well as the characteristics of coherent Er fluctuations and plasma properties.
The method employs a standard microwave fluctuation reflectometer, but it intentionally configures the launch and receive antennas at an angle relative to the plasma cutoff surface, rather than a normal incidence angle. This unique arrangement results in a hybrid diagnostic approach that combines the wavenumber sensitivity typical of traditional microwave scattering techniques with the precise radial localization capabilities of reflectometry. Furthermore, this diagnostic technique maintains the advantages commonly associated with reflectometry, such as simplicity of operation and minimal requirements for accessing the experimental setup. Concerning the functioning principle, a microwave system, consisting of a transmitting antenna and a receiving antenna, is used. This system sends electromagnetic waves (radio waves) into the plasma. The electromagnetic waves interact with the plasma and may undergo scattering, which means they can be deviated from their trajectory due to the presence of charged particles, if particles in the plasma are in motion, such as due to turbulent fluctuations or radial motion, the Doppler effect can affect the electromagnetic waves. This event means that the reflected waves will have a different frequency compared to the ones sent and the receiving antennas capture the reflected waves and measure the frequency differences compared to the original waves. These differences are due to the relative velocities of the plasma particles compared to the electromagnetic waves. From the detected

frequency discrepancy, it is possible to deduce information about the motion of particles in the plasma, which can include the radial velocity of the particles and the turbulent fluctuations that cause frequency variations. In essence, Microwave Doppler reflectometry offers a comprehensive view of the radial electric field and its variations.

4.3 ICRF Multichannel Reflectometry

To start, radio waves designed to interact with the ions in the plasma are generated at frequencies within the ICRF range. The generated radio waves are transmitted into the plasma through a specially designed antenna for this application which can be referred to as a "wave launcher". In the plasma, the radio waves interact with the ions, responding to these waves in a specific manner depending on their properties such as mass and charge. Hence, some of the radio waves are reflected by the ions in the plasma. The frequency and amplitude of the reflected waves depend on the characteristics of the ions and the plasma conditions. The reflected waves are received by a dedicated antenna or receiving system, able to measure the frequencies and amplitudes. The collected data is then analyzed to obtain information about the plasma's properties, including ion density, ion temperature, ion composition, and other plasma characteristics. This technique involves the use of multiple frequencies or channels and each channel is tuned to a specific frequency to interact with a particular ion population. This allows for more detailed information about the plasma. The locations and line of sights of these antennas and the position can be seen in Fig.(**??**). The reflectometry antennas in ASDEX Upgrade are embedded in the ICRF antenna 4 in Sector 12 of ASDEX Upgrade. From the 10 available antennas, 7 are accessible from outside the vessel and of these only antennas 1, 4 and 8 are instrumented.

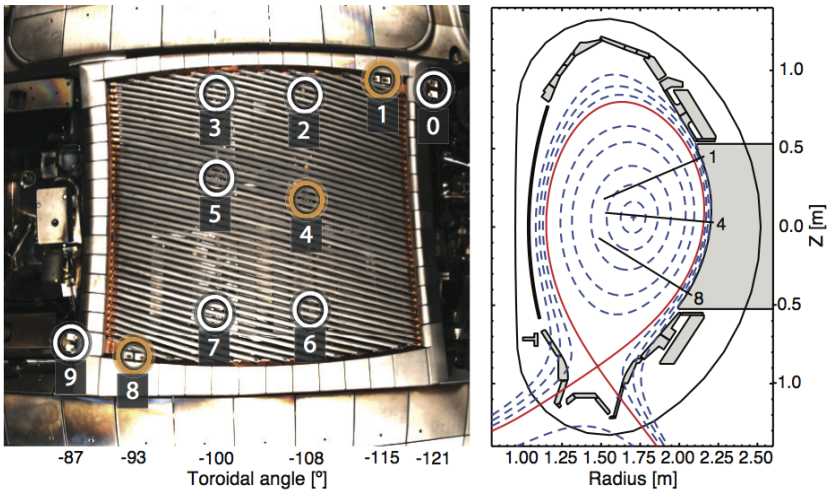

Figure 31: Reflectometry antennas positions in the toroid.

4.4 Ionization Pressure Gauges

Ionization pressure gauges are instruments used to measure the pressure of gases by exploiting the ionization of gas molecules within a confined space. They operate based on

the principles of ionization and electron motion. The ionization pressure gauge consists of a chamber filled with the gas of interest. When pressure is applied to the gas within the chamber, the gas molecules become more closely packed and as the pressure increases, the gas molecules experience greater collisions with each other. To measure this pressure, a filament or electrode is placed within the chamber and when an electric current is passed through the filament, it heats up, and electrons are emitted from its surface through a process called thermionic emission. Then, these electrons are accelerated by an electric field within the gauge and collide with the gas molecules within the chamber, in this way these collisions can result in the ionization of gas molecules. In fact, in this process, an electron collides with a gas molecule, transferring enough energy to remove an electron from the gas molecule, creating positive ions and free electrons. The positively charged ions created by the ionization process are attracted to a positively charged collector electrode, while the free electrons move toward a separate electrode with a negative charge. The movement of these ions and electrons results in an electric current, which the magnitude is directly proportional to the number of ionized gas molecules, which, in turn, is related to the gas pressure within the chamber.
In particular for AUG, ionization pressure gauges are used to evaluate the flux density of neutrals at different poloidal and toroidal positions in the vacuum vessel. From this quantity the gas pressure or the neutral particle density may be derived if the temperature of the neutrals is known. With Eq.(64), the flux density F is:

$$F = n \cdot v_{ave} \; [atoms/(m^2 \cdot s)] \tag{64}$$

With the volume density $n = p/(k_B \cdot T)$ $[atoms/m^3]$ and the mean velocity of the particles v_{ave}.
In Fig.(32) are presented the locations of the 25 ASDEX Upgrade manometers in a poloidal section projection and in the toroid:

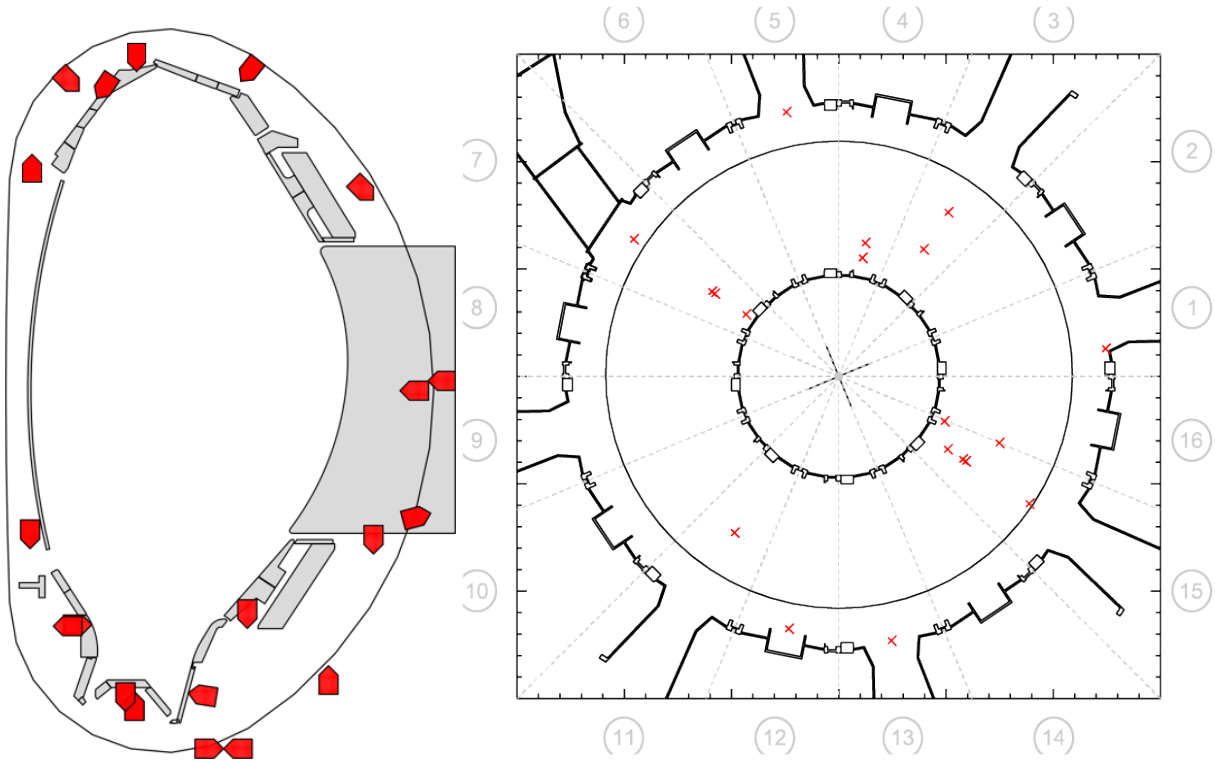

Figure 32: Picture of the position and orientation of the manometers along the R, Z and ϕ dimensions.

4.5 Thomson Scattering

Thomson scattering is a diagnostic technique used to measure plasma properties, including electron temperature and ion density and enables non-perturbative local measurements of both electron density n_e and electron temperature T_e, providing unique insights into divertor physics. A high-density plasma is probed with a laser beam which interacts with the plasma's electrons, causing the photons to scatter due to variations in electron density and temperature. During scattering, the laser photons change frequency and this change, known as the Thomson scattering frequency shift, is directly related to the electron temperature of the plasma. A detection system collects the scattered photons and measures the frequency shift, using these data to determine the electron temperature. Indeed, the width and shape of the scattering spectrum can be used to determine the temperature of electrons within the plasma Moreover, by examining the width of the Thomson spectral line, it's possibile to measure the ion density in the plasma.

A *Divertor Thomson Scattering (DTS)* system has been recently implemented. The ASDEX Upgrade DTS system comprises 26 channels spanning from the inner divertor to the outer divertor, passing through the X-point. It is equipped with a four-channel filter set to measure T_e ranging from approximately $1eV$ to $50eV$ and n_e from $10^{19} part./m^3$ to $10^{21} part./m^3$.
A new DTS system, featuring a separate laser, was installed with scattering volumes along a poloidal cord. This cord initiates at the outer divertor plate, traverses the X-point, and

terminates on the high field side. This TS system allows for obtaining local quantitative information about electron density and temperature in the divertor volume, which is not achievable with alternative methods such as Langmuir probes or spectroscopy. Due to the lack of direct access to these regions from outside the vacuum vessel, critical components of the laser beam line and the light collection system had to be installed inside the vacuum vessel.

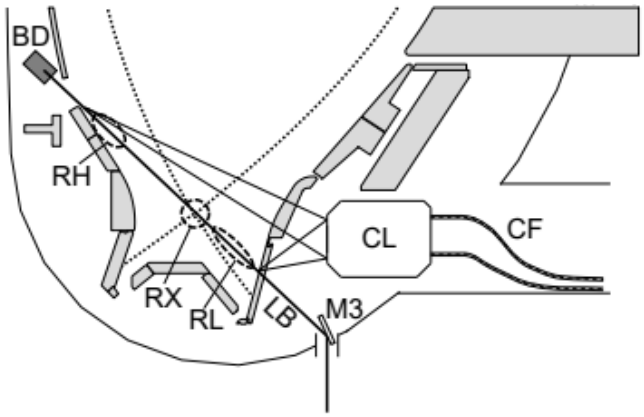

Figure 33: Poloidal cross section of the scattering geometry. The laser beam (LB) runs over a mirror (M3) to the three ROIs (i.e, regions of interest RL, RX, RH) for a dedicated magnetic reference equilibrium, and finally to the beam dump (BD). The scattered light is coupled to optical fibers (CF) by the collection lens (CL).

The Regions of Interest in the lower divertor, targeted for coverage by the divertor thomson scattering system, include the areas above and along the outer divertor leg (RL), the x-point (RX), and the high-density front region in the far scrape-off layer on the high field side (RH). To reach these regions, the laser beam path (LB in Fig.(33)) is defined inside the vacuum vessel. Both a laser mirror, the laser beam dump, and the collection lens, which couples the Thomson scattered light to fiber guides, must be installed inside the vacuum vessel, which complicated the realisation of DTS.

4.6 Langmuire probes

One of the measurement tools considered in this type of experimental reactors are the Langmuir probes. It is a diagnostic tool invented by Irving Langmuir in the 1920s, used in plasma physics and fusion research to measure various properties of plasma, such as electron temperature, electron density, and plasma potential. The probe consists of a small metallic electrode, typically made of tungsten or other heat-resistant materials, which is inserted into the plasma chamber. When the probe is biased with a voltage, it attracts charged particles from the plasma towards its surface. Langmuir probes operate based on the principle of plasma sheath formation: when the charged particles approach the probe, they are slowed down by the electric field surrounding the probe, creating a plasma sheath, which acts as a barrier, preventing further movement of charged particles towards the probe surface. The sheath thickness depends on the plasma density and temperature.

By measuring the current flowing to or from the probe surface, the Langmuir probe can provide information about the plasma properties. The current-voltage characteristic, known as the Langmuir curve, is used to extract data: the probe is typically swept through a range of voltages, and the resulting current is measured at each voltage point. The electron temperature can be determined by analyzing the slope of the Langmuir curve, while the electron density is obtained from the current at a certain voltage. In the context of a fusion reactor's plasma chamber, Langmuir probes are essential for monitoring and controlling the plasma conditions. They help scientists understand and optimize the fusion process by providing real-time data on electron temperature and density, which is a crucial information for maintaining stable and efficient plasma conditions, as well as validating theoretical models of fusion reactions.
In tab.(5) and tab.(6), the positions for the Langmuir probes in the inner and outer divertor plates (*Langmuir Inner Divertor LID*, *Langmuir Outer Divertor LOD*) are listed, represented by radial, vertical, and toroidal coordinates:

LID probes			
probe	$R[m]$	$Z[m]$	$\phi[^o]$
uic	1.266	-0.857	21.89
uib	1.281	-0.903	24.36
ui9	1.288	-0.962	33.75
ui8	1.28	-0.995	29.01
ui7	1.274	-1.013	33.91
ui6	1.268	-1.031	37.84
ui5	1.262	-1.049	41.13
ui4	1.255	-1.067	43.96
ui3	1.249	-1.085	46.34
ui2	1.243	-1.103	48.39
ui1	1.237	-1.121	50.11

Table 5: : LID probes position

LOD probes			
probe	$R[m]$	$Z[m]$	$\phi[^o]$
ua1	1.602	-1.212	-53.62
ua2	1.606	-1.187	-50.86
ua3	1.61	-1.164	-47.87
ua4	1.615	-1.132	-44.67
ua5	1.62	-1.1	-41.23
ua6	1.625	-1.07	-37.57
ua7	1.628	-1.046	-32.59
ua8	1.634	-1.013	-27.38
ua9	1.64	-0.984	-12.67
uaa	1.658	-0.938	-16.54
uab	1.672	-0.911	-13.73
uac	1.688	-0.885	-9.89

Table 6: : LOD probes position

In the absence of a tin source, the plasma conditions are expected to exhibit toroidal symmetry. However, in close proximity to the Sn target, it's possible to encounter localized variations in plasma properties. To address this, two Langmuir probes were affixed to the tile, with one positioned upstream and the other downstream of the CPS, in this way the probes were able to detect local disparities in electron temperature and density attributed to the presence of a Sn source. Furthermore, additional tiles situated further toroidally around the divertor were also equipped with Langmuir probes and the data collected from these sensors can serve as a reference measurement. These measurements are valuable for pinpointing the radial position at which Sn influences the plasma conditions.
Fig.(34) depicts the positions of the probes relative to their projections on the poloidal section of the machine. On the other hand, fig.(35) illustrates their spatial arrangement with respect to the entire toroid:

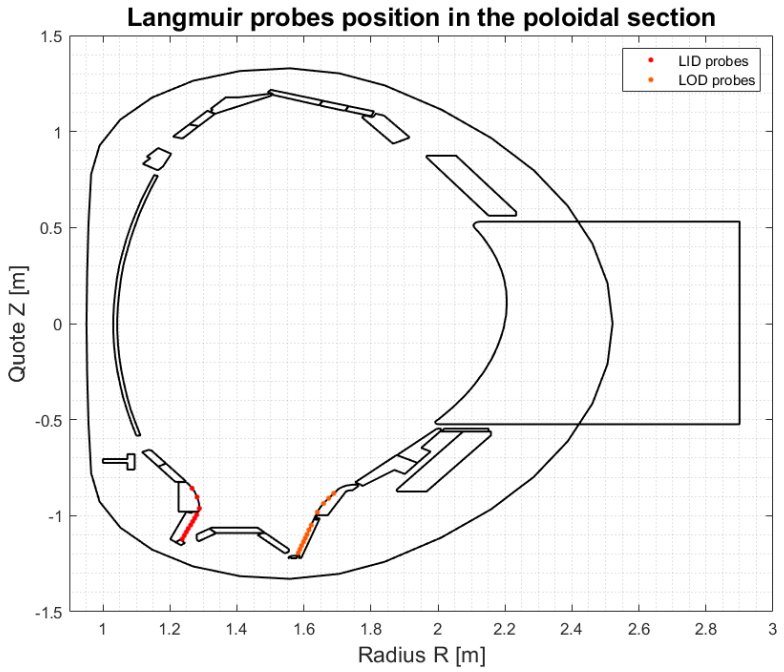

Figure 34: Langmuir probes - poloidal section representation

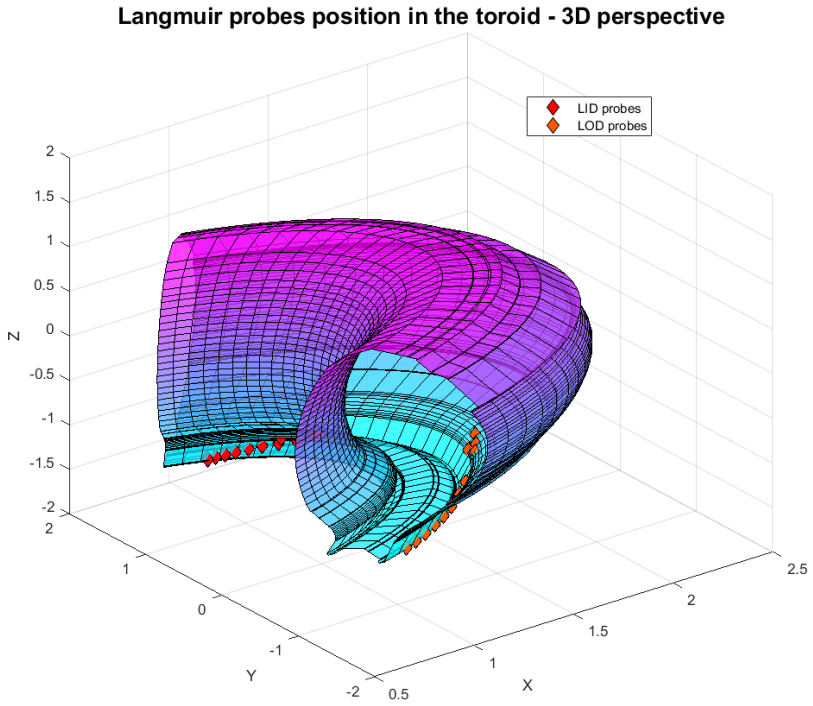

Figure 35: Langmuir probes - 3D representation

4.7 Simulated Data as Integration of Experimental Data

To ensure a proper initialization of the simulation and obtain a comprehensive dataset, the decision was made to use, alongside experimental data related to discharges (as discussed in 4), a series of data derived from simulations representing the same context and physics as those discussed in this thesis.
As a result, some simulation outcomes conducted in SOLPS on ASDEX SOL are proposed as initialization values. Specifically, these results refer to a study of discharges carried out in pure deuterium with no impurities, with the outputs shown in the following figures:

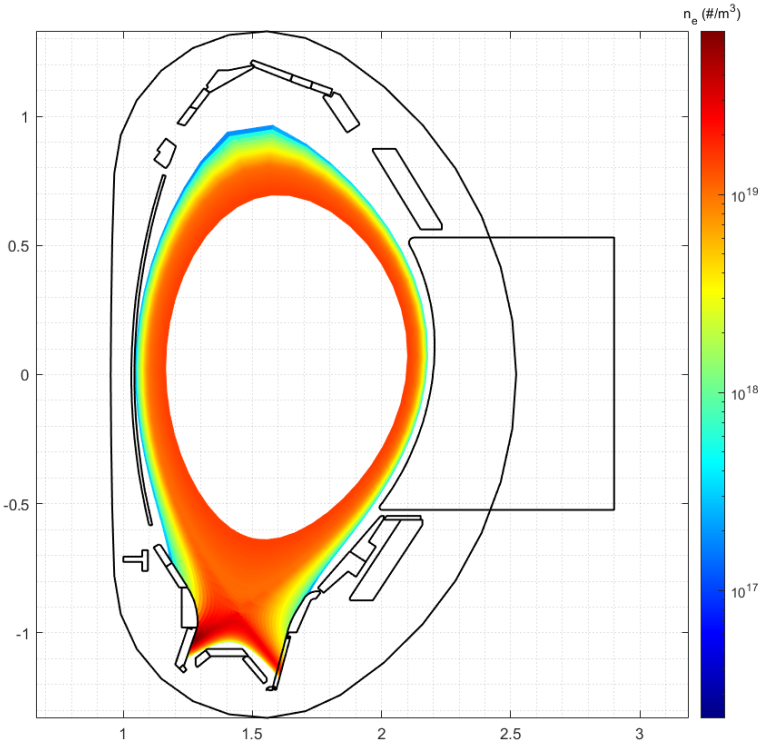

Figure 36: Electron density representation.

There is a noticeable rarefaction near the walls of the blanket compared to the more central part of the SOL, while there is an increase in density close to the targets, along the portion between the X-point and the two target plates. Fig.(37) provides a zoomed-in view of the region related to the divertor just discussed.

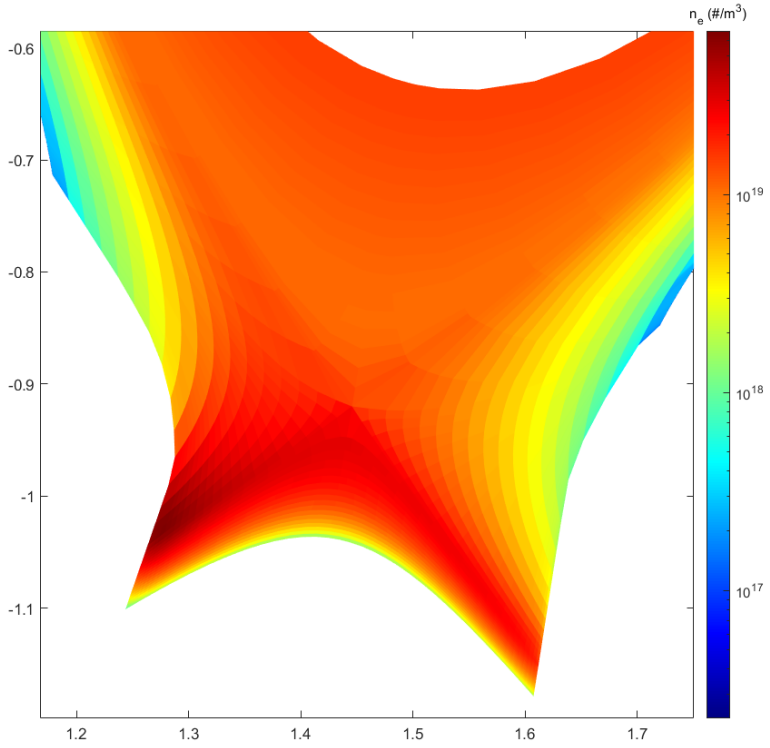

Figure 37: Representation of a closer POV of electron density.

As shown, this region is characterized by a higher density and temperature gradient compared to the other portions of the SOL, especially close to the strike points. In particular this can be done because *Poloidal Recycling*. Plasma in the SOL can undergo recycling processes, where charged particles follow trajectories determined by the magnetic field lines that bring them back into the SOL, towards the divertor. This phenomenon can lead to an accumulation of particles in the lower part of the SOL, helped by the magnetic field lines web configuration. Ionization and recombination are very important in this region, creating a higher density region. In Fig.(38), zoomed-in views of the profiles of ionic and electronic temperatures near the divertor are presented. In particular, it is observed that the SOL plasma tends to be cooler near the inner and outer targets, respecting the detachment principle, while the temperatures are higher close to the core region, as shown in Fig.(39).

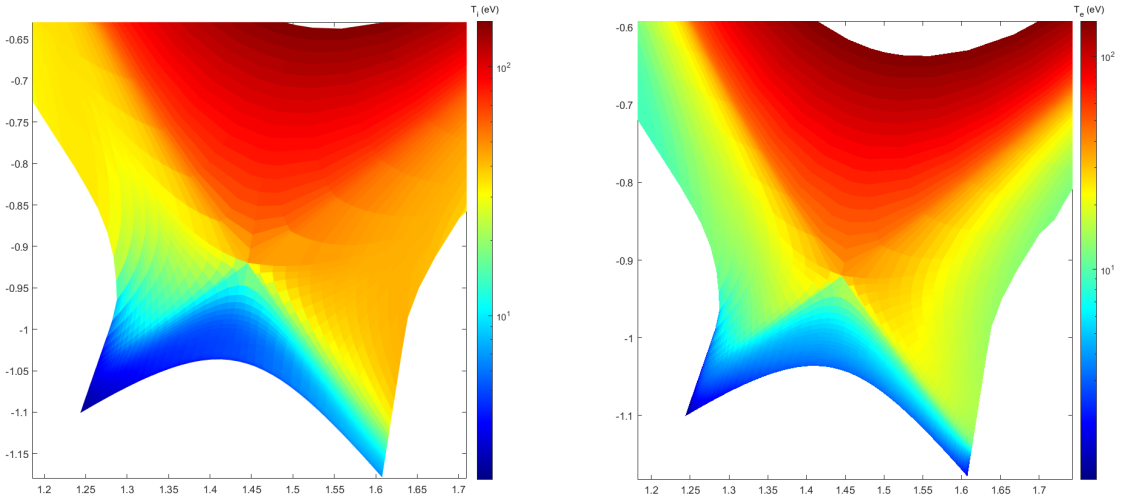

Figure 38: Representation of a closer POV of ion and electron temperature.

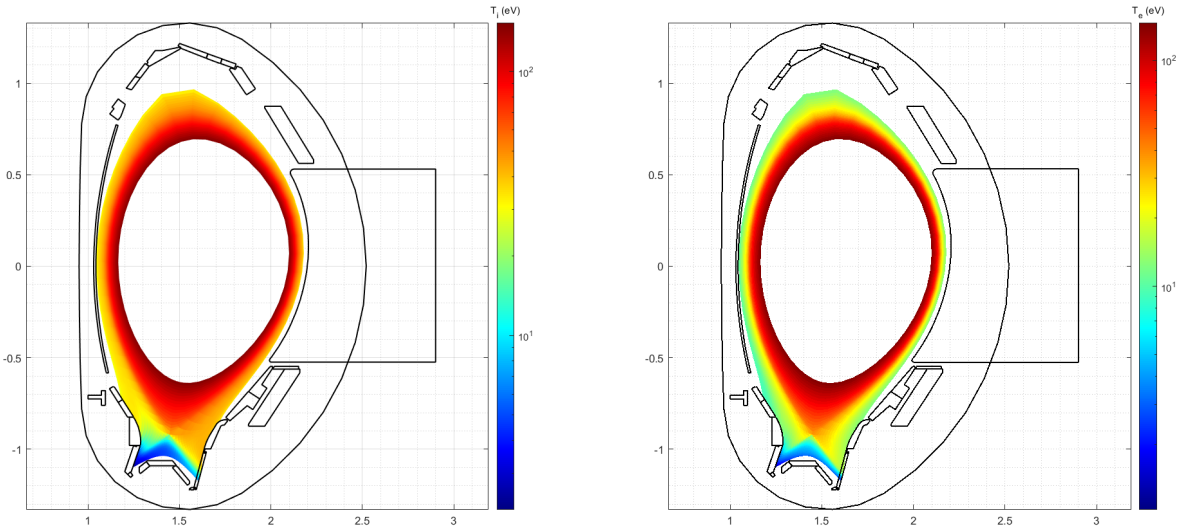

Figure 39: Ion and electron temperature representation.

Fig.(40) and Fig.(41) represents the temperature and density profiles related to the outer and inner targets of the divertor. The strike points position are highlighted in the plots:

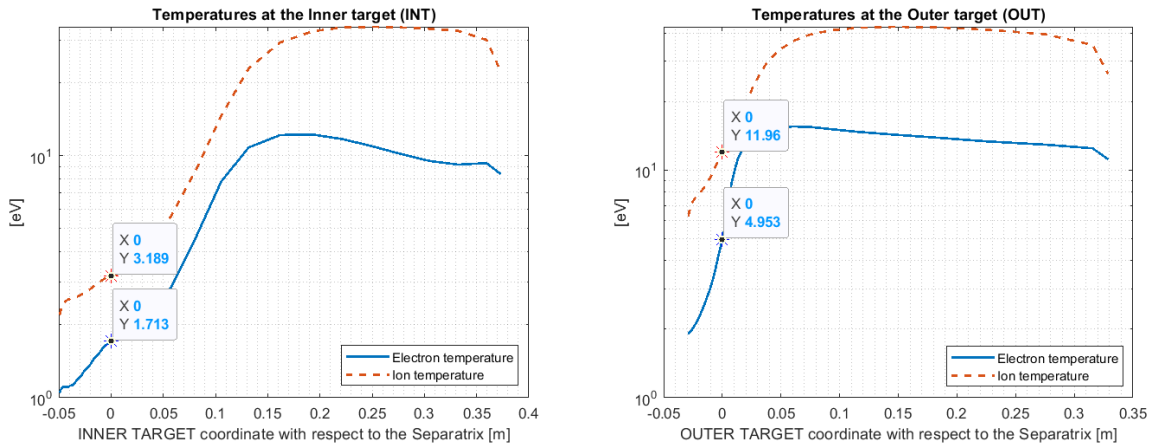

Figure 40: Ion and electron temperature trend along the inner and outer target.

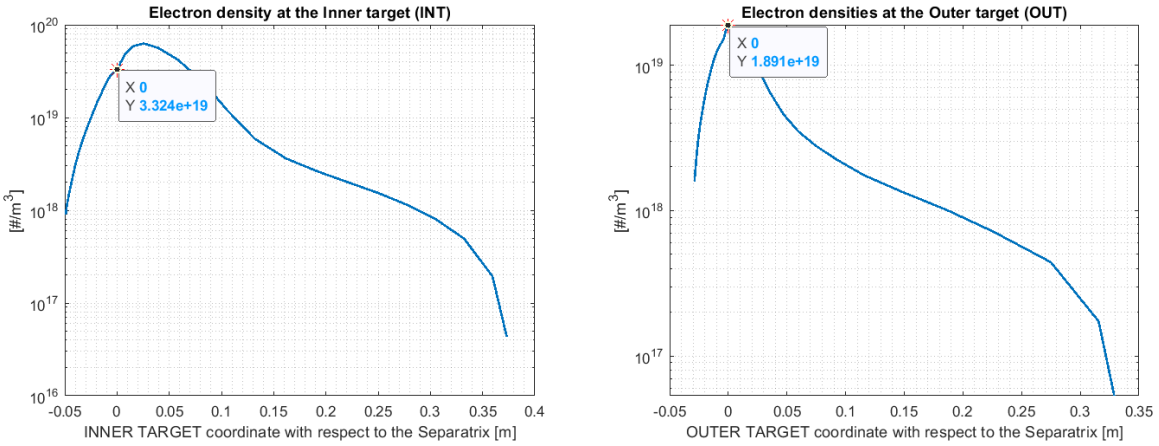

Figure 41: Electron density trend along the inner and outer target.

As already done with the inner and outer targets, Fig.(42) represents the temperature and density profiles at the *Outboard Midplane (OMP)*. The profiles shown are associated with the density and temperature values of the SOL plasma at the separatrix (at coordinate 0), displaying higher values in the regions closer to the plasma core and decreasing near the walls:

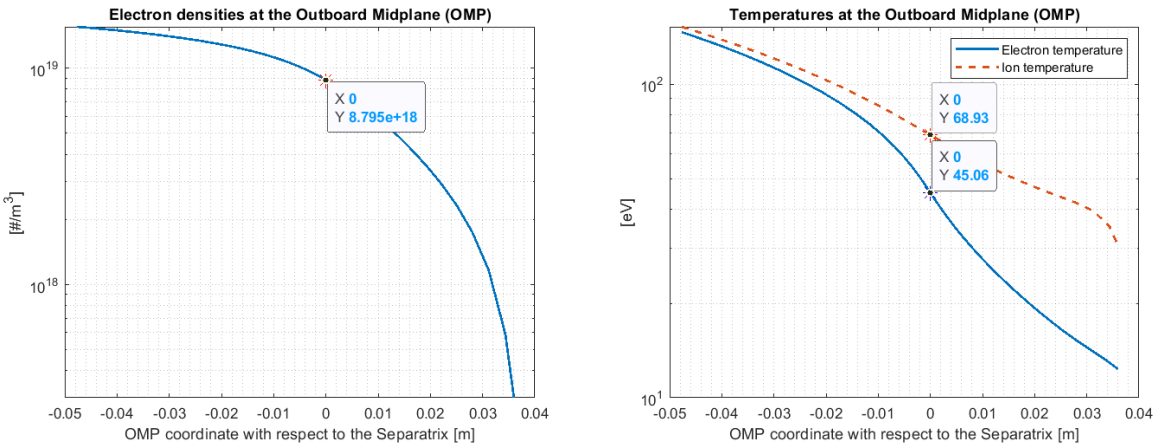

Figure 42: Electron density trend along the inner and outer target.

4.8 Data Analysis and Application for Liquid Metal Divertor Simulation

To facilitate the study of future cases with impurities, some data related to the experiment on the CPS module described in paragraph 2.5.3 and already mentioned in [11] have also been collected.

It is noteworthy that the approach to studying cases with impurities tends to be quite lenient. Indeed, the Liquid Metal Divertor does not continuously exist throughout the entire toroid but remains localized in a very specific position. Consequently, the cloud of impurities that forms will be localized near the CPS module. This situation definitely outlines a specific case in which the three-dimensionality offered by EMC3-EIRENE is a strong point, providing a highly accurate view of plasma-impurity interactions. The discharge under investigation exhibits a configuration in which the strike-point tends to move, reaching the center of the target plate within 2.5 seconds. Fig.(43) illustrates the situation under examination:

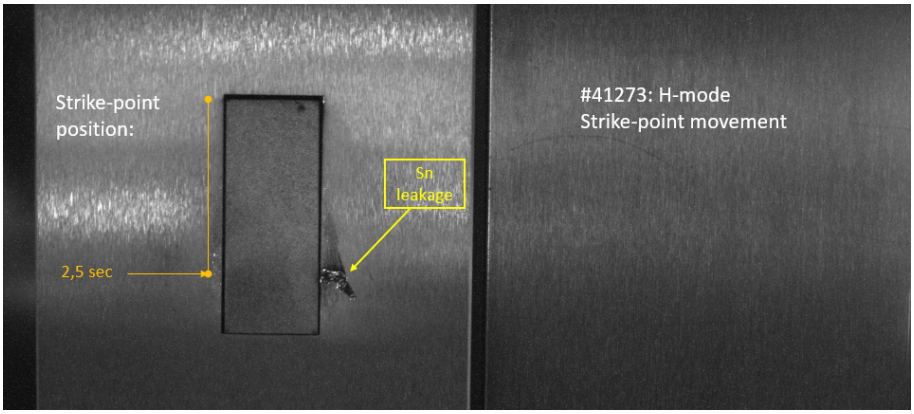

Figure 43: CPS image #41273 discharge strike-point. Presentation: "Performance of a liquid tin divertor target during ASDEX Upgrade L and H-mode operation", authors: "J.G.A. Scholte, B. Boeswirth"

Just as in the case with pure deuterium, the data were collected from the IPP Garching database (ISIS, cview, Diaggeom, ...). It is important to observe various time windows from which to extract key data. In particular, the following time points have been considered relevant:

- At 2 seconds, the moment when the strike-point effectively enters the machine's surface, exhibiting a reduced and fluctuating erosion profile.
- At 2.5 seconds, a peak in irradiation occurs, resulting in the detachment of substantial portions of tin from the divertor, as shown in the fig.(43).
- At 5.5 seconds, maximum erosion is reached, and the conditions remain stable and consistent.

The discharge experiences temporal variations, causing the separatrix to exhibit different geometric configurations depending on the analyzed time instance. Consequently, the null-points and strike point undergo displacement over time. Fig.(44) displays the correlating separatrix configurations, considering the dimensions of the PFCs and the vacuum vessel.

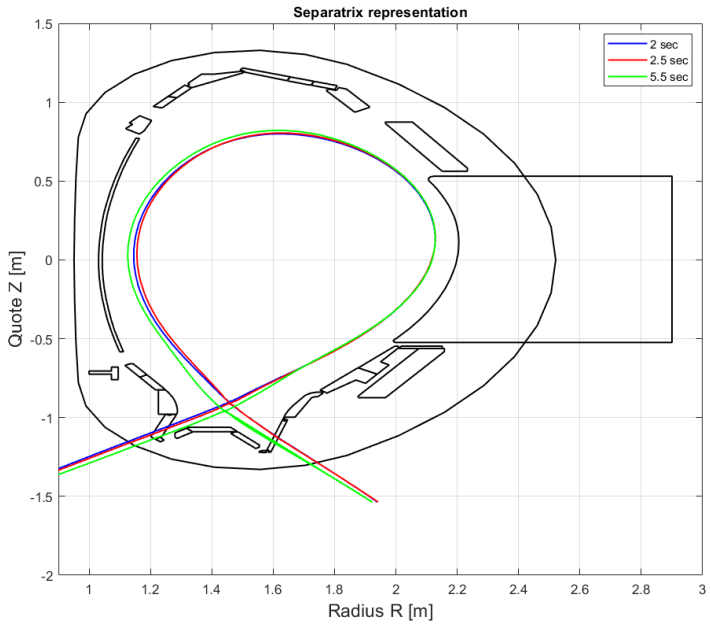

Figure 44: Separatrix representation

With reference to the considered time instants, the magnetic field flux equilibria inside the plasma are extrapolated from the database and plotted in Fig.(45), Fig.(46) and Fig.(47).

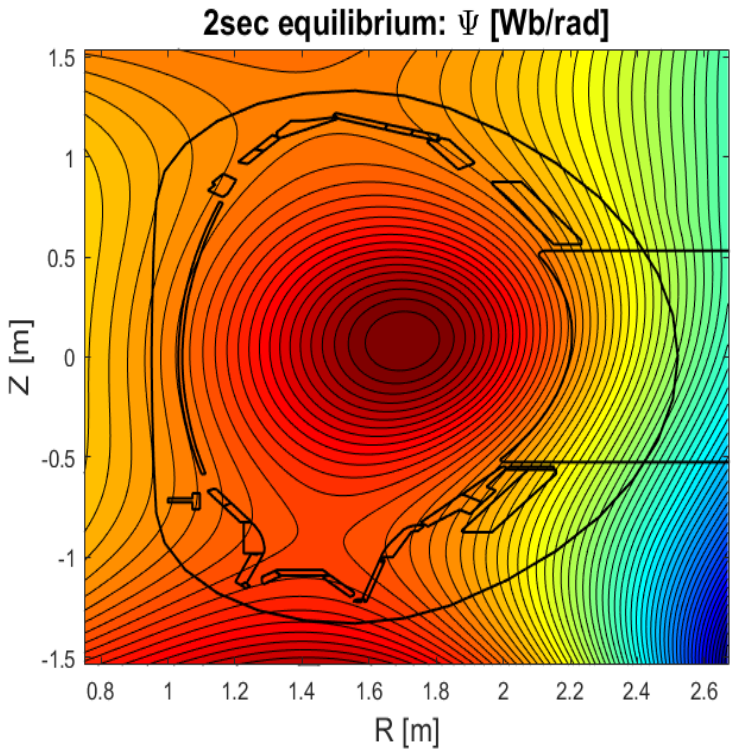

Figure 45: Magnetic flux equilibrium - 2sec

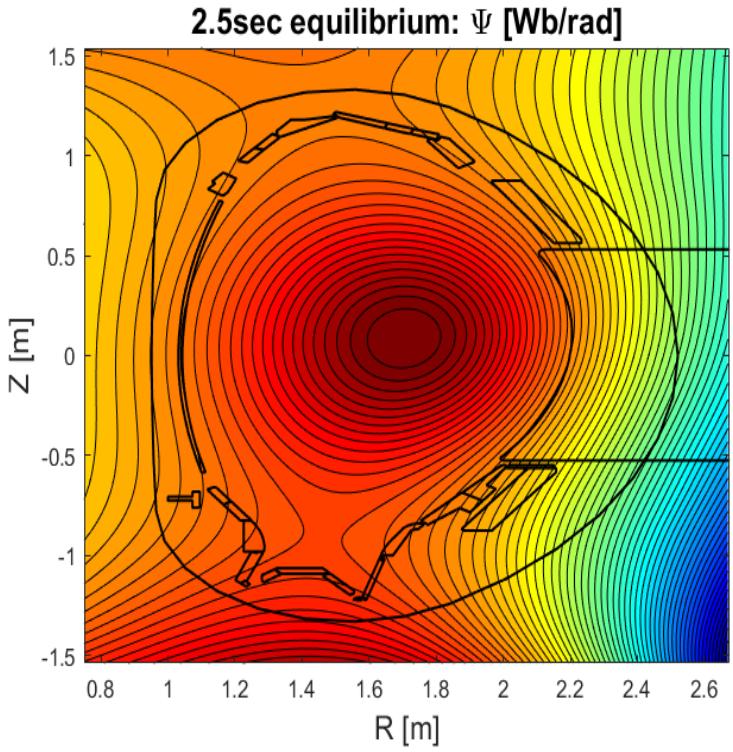

Figure 46: Magnetic flux equilibrium - 2.5sec

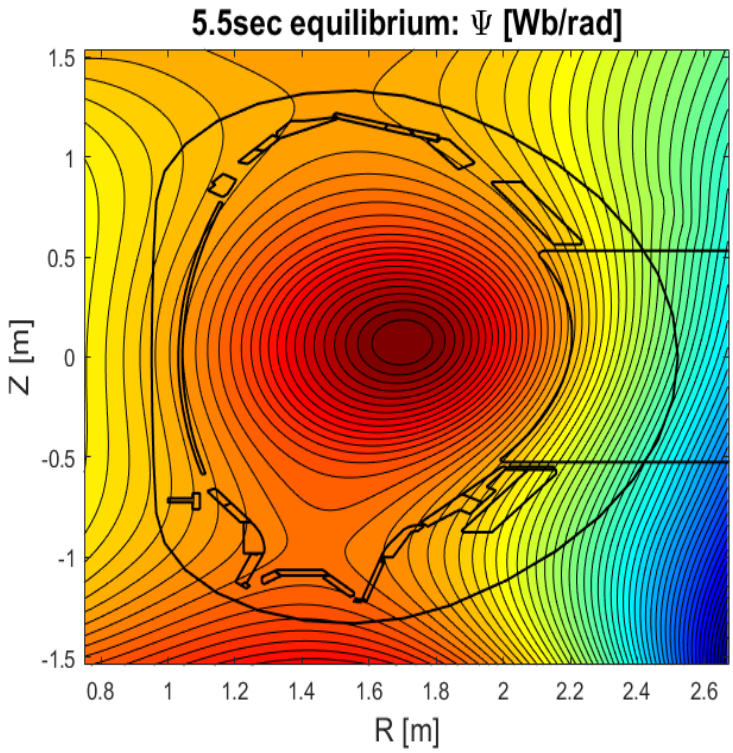

Figure 47: Magnetic flux equilibrium - 5.5sec

The experimental data indicate strong confinement of the flux at the center, denoted by denser flux lines and more intense coloring towards the plasma core. This suggests a robust and well-confined magnetic field around the plasma core, which is essential for maintaining stable plasma and optimizing fusion conditions. As the discharge reaches 5.5 seconds, the confinement slightly weakens in the plasma zone, and the magnetic field flux tends to decrease considerably in the areas surrounding the chamber.

5 Results discussion & Conclusions

Once the data is set, the simulation will yield slightly different results upon reaching convergence. Fig.(48) displays the X-point and the O-point resulting from the simulation, while Tab.(7) presents the data related to the simulated discharge.

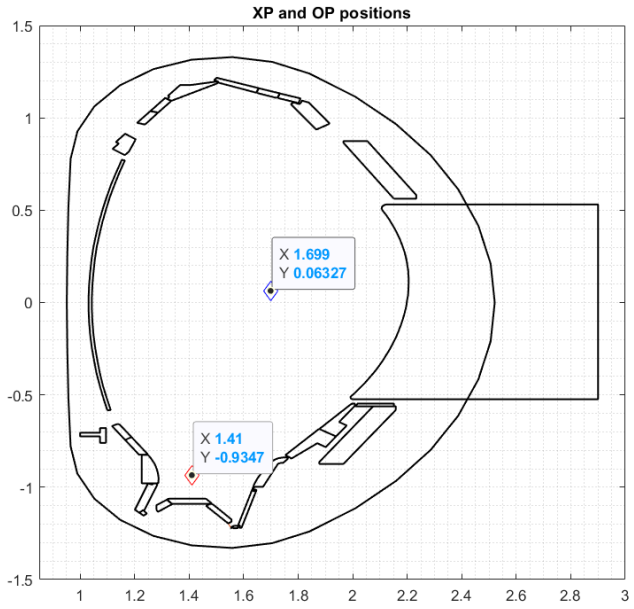

Figure 48: Simulation results of the X-point and O-point positions.

Main charge characteristics		
$L_c[m]$	$B_t[T]$	$I_p[MA]$
40.96	1.902	0.998

Table 7: : Key data resulting from the simulation.

The following figures will show the profiles of various quantities on a poloidal section of the tokamak, reminding that the results to be discussed are not related to a complete description of the plasma zone, but are exclusively confined to the SOL. The graph in Fig.(49) and Fig.(50) show a cross-sectional view of the tokamak focusing on the electron density. The density is expressed in units of 10^{19} electrons per cubic meter. The plasma appears to be denser at the center of the tokamak while lower densities are found near the tokamak wall and in the divertor regions, this is expected since the core of the plasma tends to have a higher electron density. It is interesting to note that there are regions of relatively high density extending downward towards the divertors, suggesting that the plasma in these areas is potentially influenced by edge processes, such as the recirculation or pumping of electrons from the core to the edge. The shape of the plasma is well confined, which is essential for

maintaining efficient fusion reactions. The position and shape of the divertor are clearly visible, indicating that the simulation includes the effects of the plasma edge and the configuration of the reaction chamber.

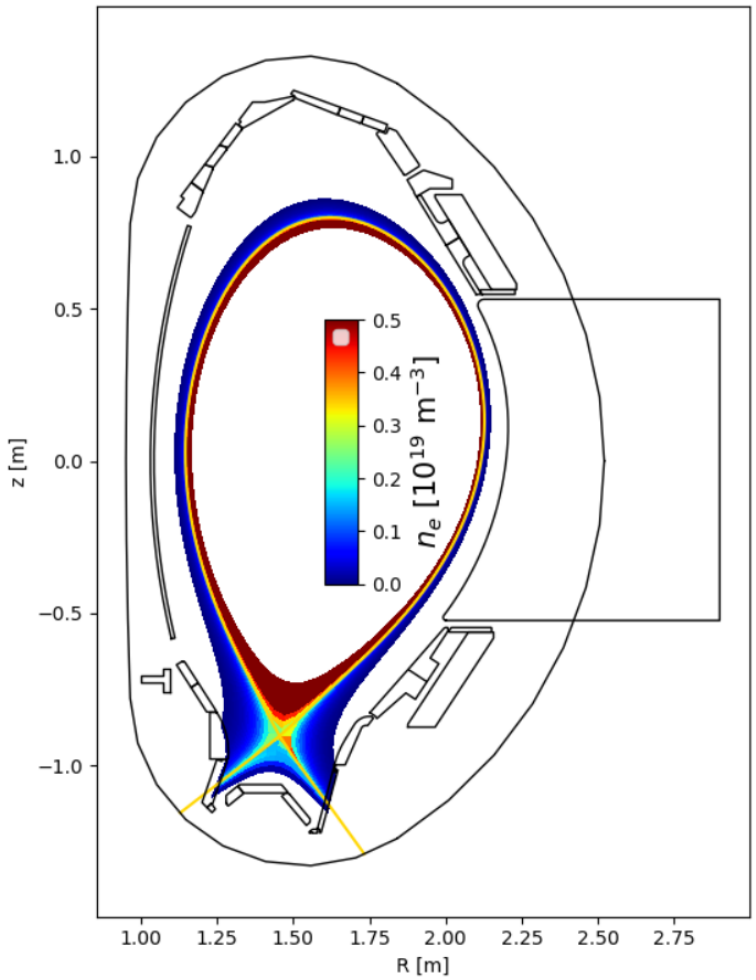

Figure 49: Electron density (n_e) depiction: General overview.

The picture on the bottom is a zoom-in on the X-point area in a tokamak, focusing on a detailed representation of the electron density in the divertor. This area is particularly critical in magnetic confinement devices like tokamaks because it is the point where magnetic field lines cross before heading towards the divertor plates. It is worth noting that the density is higher along the divertor arms, which is typical since these are the areas where the plasma interacts with solid material and can be influenced by phenomena such as particle deposition and cooling. In particular this is verified when considering that charged particles, such as electrons, tend to follow the trajectories dictated by the magnetic field lines, which results in a concentration of these charges along the lines themselves, consistently with the physics and the configuration adopted for the plasma confinement explained in chapters 1 and 2.

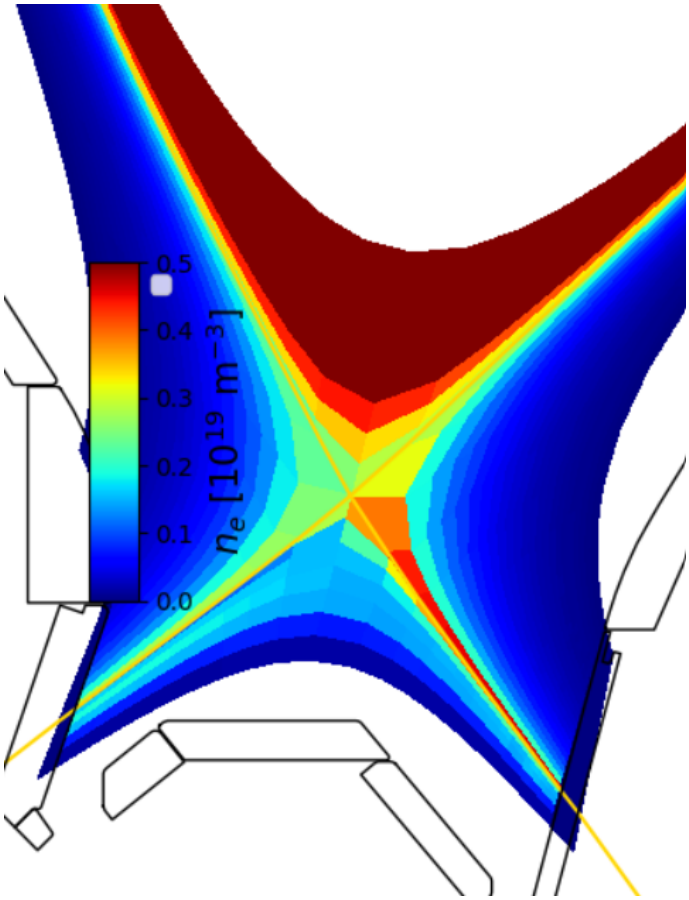

Figure 50: Electron density (n_e) depiction: Zoom on the X-point.

In Fig.(51), it is possible to observe a significant variation in the density of deuterium within the plasma, where the deuterium density is higher in the lower part of the reactor. This suggests an accumulation of deuterium in this area, due to recirculation processes or confinement in the divertor region.

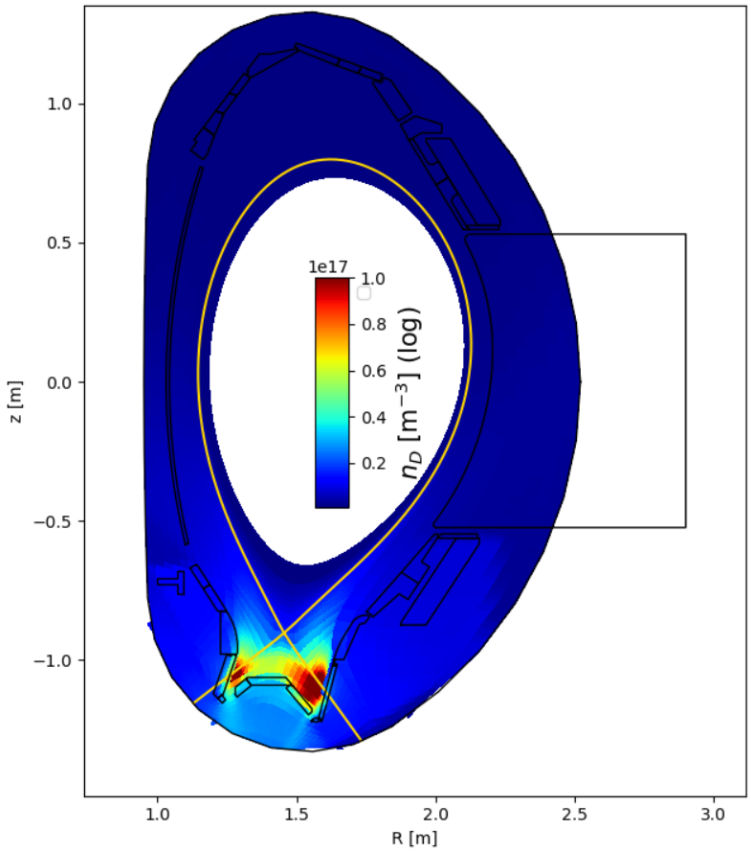

Figure 51: Deuterium density (n_D) depiction: General overview.

In Fig.(52), which is a zoom-in on the divertor, the interactions of deuterium with the divertor structures and the established density gradients are detailed. The areas with higher density (red and yellow) near the divertor plates indicate zones of high interaction between the deuterium and solid surfaces. In particular, phenomena such as recombination reactions improve the local density of neutrals since the vicinity with the divertor targets.

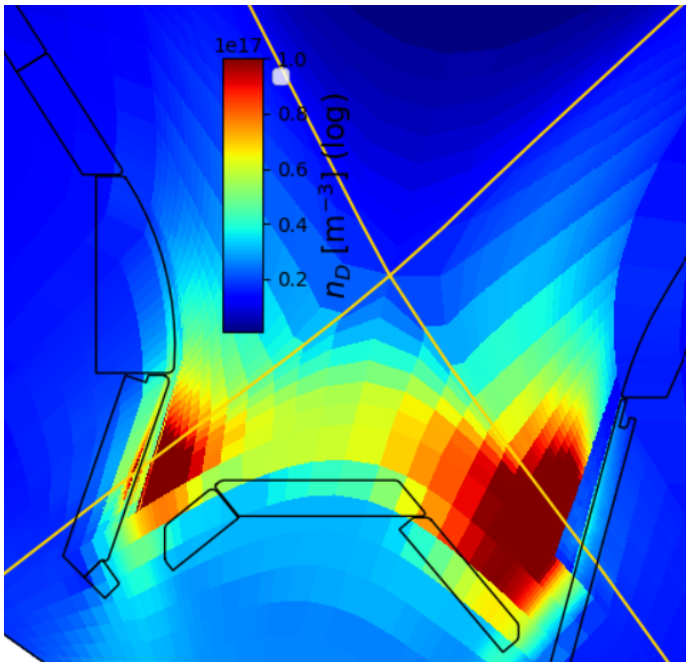

Figure 52: Deuterium density (n_D) depiction: Zoom on the X-point.

The total pressure is a key indicator of the plasma operating conditions and helps to determine the confinement regime, which is essential for achieving efficient and sustainable fusion reactions. The following images provide a detailed view of how the plasma pressure varies within the tokamak, giving insight into plasma confinement and stability.
It can be observed that the highest pressure is concentrated at the center of the plasma, decreasing towards the edge and the divertor. This is typical of pressure profiles in tokamaks, where the pressure is maximal at the center and drops towards the edge, helping to keep the plasma stable and confined. The pressure profile is a good indicator of plasma equilibrium and its confinement.

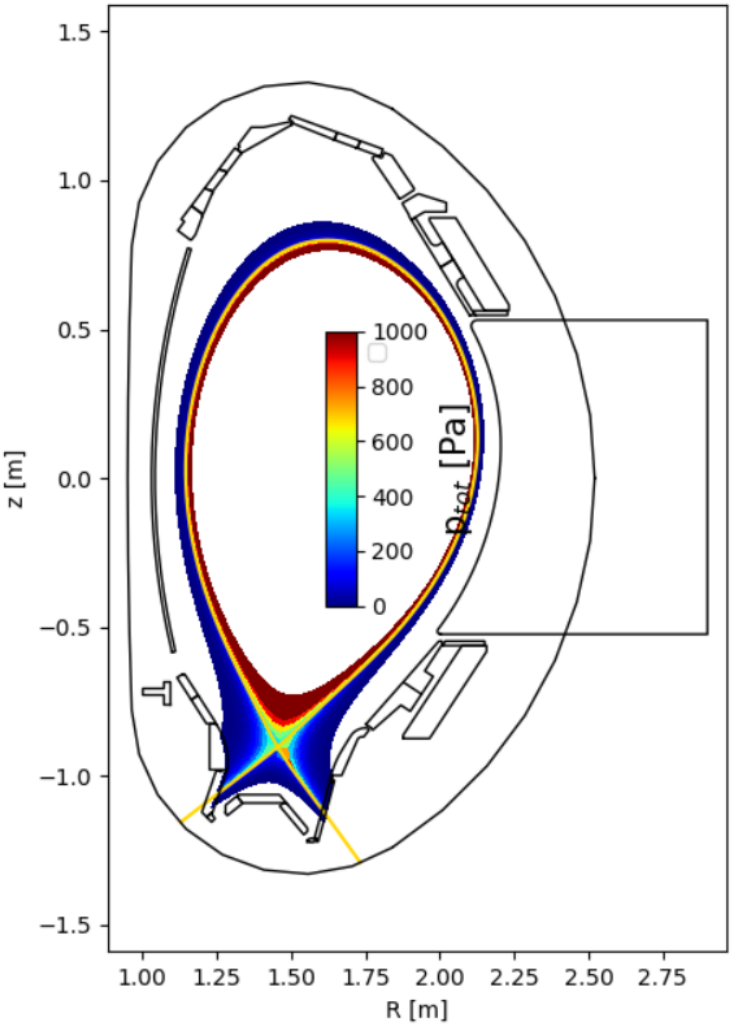

Figure 53: Plasma pressure ($p_{tot]}$) depiction: Zoom on the X-point

The Fig.(54) is a zoom on the divertor area and shows the pressure distribution in this critical region. The highest pressure is found away from the divertor, indicating that the plasma in that position is relatively cool and rarefied compared to the core of the plasma. Pressure gradients are important because they can drive plasma flows and instabilities, thus influencing the transport of particles and heat towards the surfaces of the divertor.

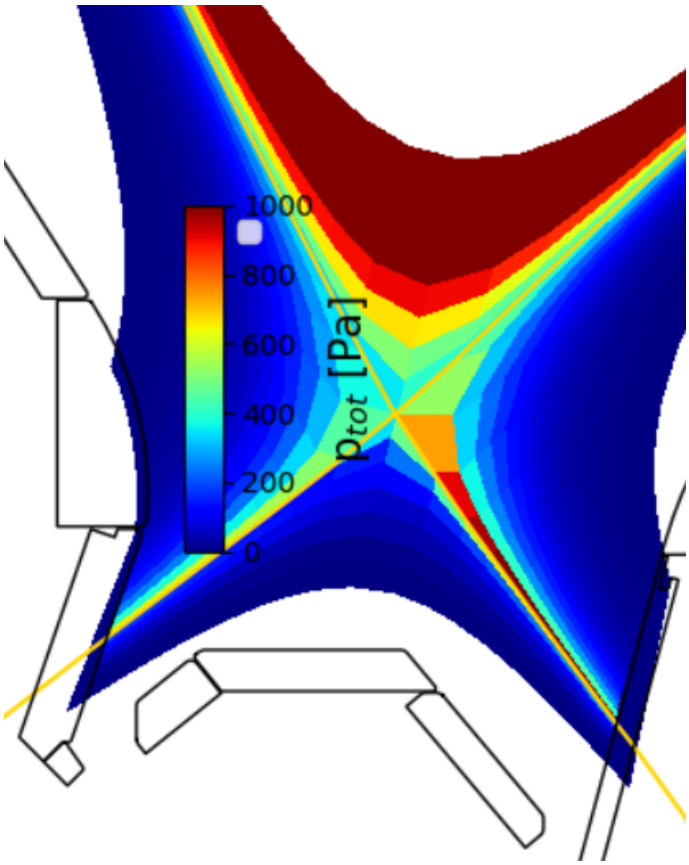

Figure 54: Plasma pressure (p_{tot}) depiction: Zoom on the X-point

In Fig.(55) can be observed that the highest temperature is concentrated at the center of the plasma, which is typical since the core of the plasma is the point where the temperature reaches the peak necessary for fusion processes. The temperature decreases as one moves towards the edge and the divertor, where interactions with the walls and structures of the tokamak can cool the plasma. This distribution is consistent with that of the electron temperature, suggesting that ions and electrons are relatively well thermalized in the core of the plasma. In fact, significant differences between T_i and T_e can indicate areas of instability or regions where heating or cooling processes are out of balance. Good thermalization between electrons and ions is essential for maintaining plasma pressure and for optimizing the rate of fusion reactions.

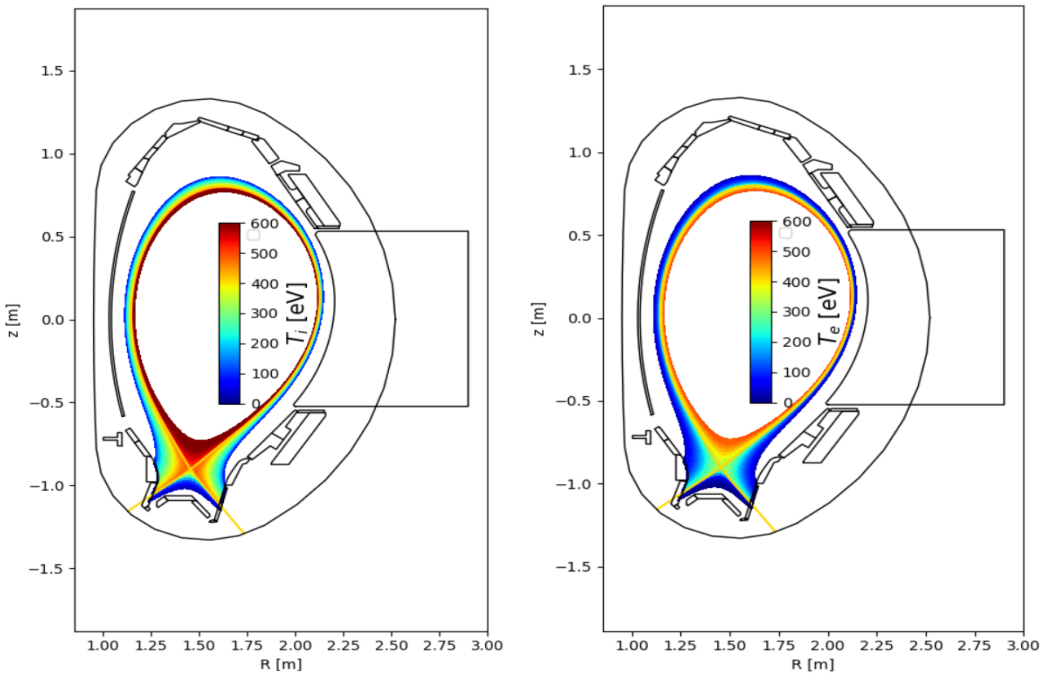

Figure 55: Ion end Electron temperatures (T_i e T_e) depiction: General overview

The zoomed images provide a detailed representation of the temperature profiles. Both the images reveal that there are significant temperature gradients in the plasma near the divertor: the warmer areas are closer to the plasma core and close to the X-point, while the cooler regions (blue) are located near the divertor structures. This is consistent with the expectation that the plasma cools significantly as it moves from the hot center of the tokamak towards the cold walls of the divertor, where heat exchange with solid structures occurs. It is essential to highlight that both in the private zone and in the immediate vicinity of the inner and outer targets, the temperatures are significantly low (dark blue), indicating that the profiles to be evaluated along the targets exhibit extremely small values in comparison to the surrounding context, as can be observed in Fig.(58).

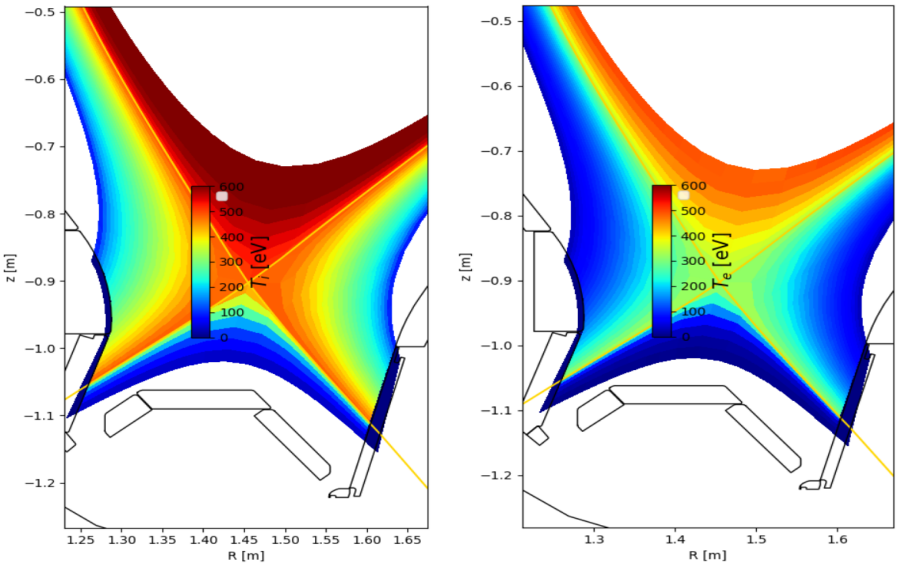

Figure 56: Ion (T_i) end Electron temperatures (T_e) depiction: Zoom on the X-point

In Fig.(57), the thermal flux parallel to the flow lines is represented; notably, it tends to be stronger near the core. Outside the plasma column, the flux becomes null, except along the separatrix, where the transport of high-energy particles is significant, and thus the flux tends to assume high values.

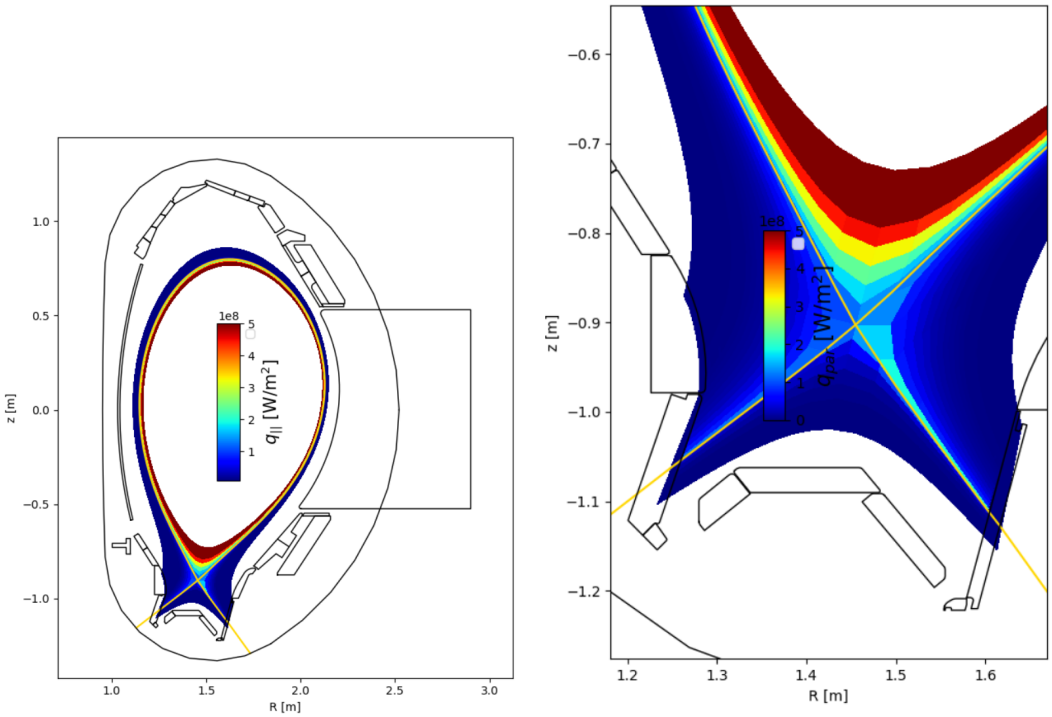

Figure 57: Parallel Heat flux q_{par} depiction.

The following set of figures illustrate a variety of trends related to plasma characteristics already discussed, in the vicinity of the inner and outer target, as well as near the roof baffle. Specifically, these trends will be detailed according to the poloidal flow coordinate, ρ_{pol}, defined as follows:

$$\rho_{pol} = \sqrt{\frac{\Psi - \Psi_a}{\Psi_s - \Psi_a}} \tag{65}$$

Equation 65: Definition of the poloidal flux coordinate ρ_{pol}

With Ψ the poloidal flux, the index s referring to the separatrix, and the index a to the magnetic axis. ρ_{pol} is scaled so that it becomes $\rho_{pol} = 0$ on the magnetic axis $\rho_{pol} = 1$ at the separatrix.

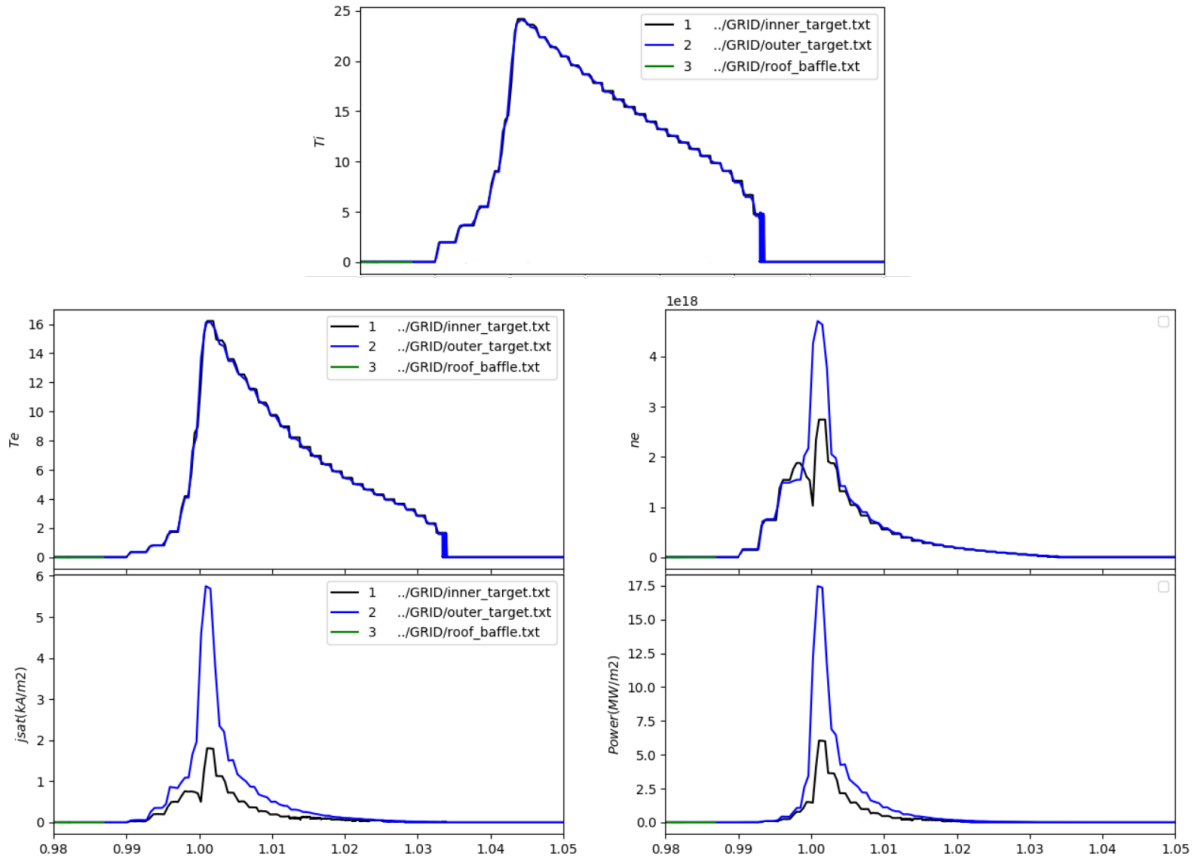

Figure 58: T_i, T_e, n_e, j_{sat} and Pow target profiles.

It can be observed that the graphs are consistent with the physics of the model and tend to show their peaks exactly where the strike point is located. As previously explained, charged particles tend to follow magnetic field lines, reaching the divertor and thus exhibiting a higher concentration of electrons, increased deposited power, and consequently higher

temperatures.
The term j_{sat} is referred to the *Ion Saturation Current*, a critical parameter in plasma diagnostics and which values are closely related to local particle flows and plasma density, specifically for the ions. Commonly, is evaluated as:

$$j^i_{sat} = en^i_{se}c_s$$

With e the simple charge of electron, n_{se} the density at the sheath edge and c_s the sound speed.
To better understand the transport phenomena within the SOL plasma, it is necessary to find the transport coefficients D and χ, used to calculate the particle and thermal diffusion in Eq.(66).

$$\Gamma_{part} = -D\nabla n \qquad q_{\parallel} = -\chi_{th}\nabla T \tag{66}$$

The values of the two coefficients at the convergence of the simulation, for both the inner and outer target, are:

$$D_{part} = 0.1m^2/s \quad \chi_{th} = 3m^2/s \tag{67}$$

Considering the thermal transport coefficient and the high temperatures shown in Fig.(58), it is evident that the energy transport towards the target is excessively high. Taking into account the relation:

$$\chi_{th} = K \cdot T^{5/2} \tag{68}$$

It is understood how heat conduction close to the target is directly proportional to the target temperature T_t, and how the higher this is, the greater the energy transport from the core to the target will be.
In accordance with all this, it can be observed how the temperatures at the target are significantly higher compared to the required conditions for detachment (over $10eV$), and that the peaks of thermal flux at the strike point tend to reach $17MW/m^2$. This does not ensure the preservation of the divertor integrity nor allow for the proper functioning of the machine. Under these circumstances, the conditions for detachment cannot be maintained.

By examining the results of the simulations, it becomes clear that it is necessary to reduce the thermal load to which the divertor is subjected, and thus, to increase the energy dissipation through radiative phenomena along the SOL plasma. Paragraph 2.2 analyzed the various phenomena of plasma-impurity interactions, and how these, in a controlled manner, can play an important role in controlling thermal loads. Specifically, referring to the concept of the Liquid Metal Divertor (paragraph 2.5.3), it explains how impurities emitted through evaporation from this type of model can be of great help in mitigating the energy stress to which the divertor is subjected.

A first attempt at this type of evaluation can be made by drawing inspiration from the experiment already mentioned [11] in section 2.5.3, entitled *'Performance of a liquid tin divertor target during ASDEX Upgrade L and H-mode operation'*. As already described, in this type of experiment, a CPS module is located on the outer plate of the ASDEX Upgrade divertor. The tin impurities emitted by the module induce plasma-impurity interactions that increase the rate of radiated energy loss, thereby reducing the temperature and thermal flux values at the target. In Fig.(59), the temperature and flux profiles computed from the

simulation are compared with the actual profiles at the instant $t = 2s$ (moment of minimum erosion of the PFCs in the real experiment) of the cited discharge, which values were obtained using Langmuir probes placed near the module.

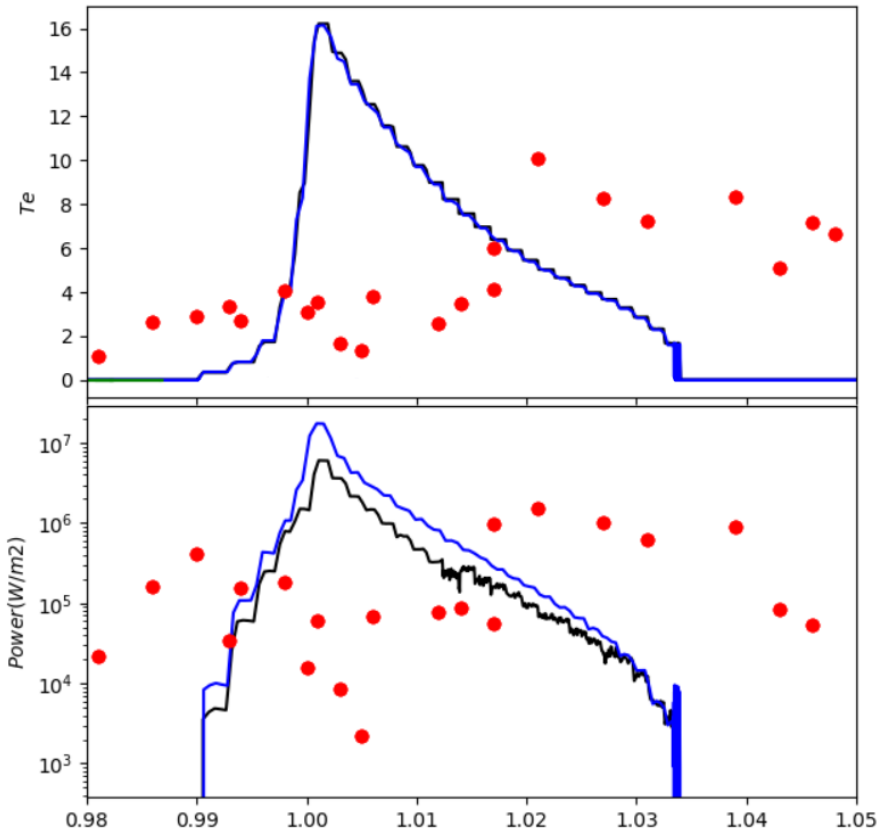

Figure 59: T_e and Pow target profiles comparison beteween simulation and CPS module case. The experimental values were obtained at the time instant $t = 2s$ of discharge #41273 under consideration. The power plot is set in a logarithmic scale to better show the magnitude difference between the results and the experimental data.

It is noted that the electronic temperatures recorded in the experiment tend to be significantly lower than those derived from the simulation, reaching peaks at most half of those computed. It should be pointed out that, as mentioned in Chapter 3, the Langmuir probes are not located in the same position; specifically, those closer to the CPS module are situated at $\rho_{pol} \simeq 1$, where the values of thermal flux and temperature are lower. The Langmuir probes that are further away exhibit higher temperature and flux values, as they are less affected by the effects of the tin impurities dispersed by the module. The values near the module are significantly lower than those computed in the same position, confirming the importance of impurities in mitigating thermal loads towards the divertor and how the Liquid Metal Divertor can be useful in preserving structural integrity. Further analysis in this field is necessary to understand how the LMD can be utilized and which type of liquid metal might be most compatible with the reactor requirements.

References

[1] M. Keilhacker. "H-mode confinement in tokamaks". In: *Plasma Physics and Controlled Fusion* (1987). DOI: https://iopscience.iop.org/article/10.1088/0741-3335/29/10A/320.

[2] G.F. Matthews. "Plasma detachment from divertor targets and limiters". In: *Journal of Nuclear Materials* (1995). DOI: https://doi.org/10.1016/0022-3115(94)00450-1.

[3] K.S. Riedel P.N. Yushmanov T. Takizuka. "SCALINGS FOR TOKAMAK ENERGY CONFINEMENT". In: *Nuclear Fusion* (1999). DOI: https://doi.org/10.1088/0029-5515/30/10/001.

[4] Peter C. Stangeby. *The Plasma Boundary of Magnetic Fusion Devices*. Series in Plasma Physics and Fluid Dynamics. Nicki Dennis, 2000. ISBN: 0750305592, 9780750305594.

[5] Y. Feng. "Recent Improvements in the EMC3-Eirene Code". In: *Contributions to Plasma Physics* (2004). DOI: https://doi.org/10.1002/ctpp.201410092.

[6] Boerner P. Reiter D. Baelmans M. "The EIRENE and B2-EIRENE Codes". In: *Fusion Science and Technology* (2005). DOI: https://doi.org/10.13182/FST47-172.

[7] F. Wagner. "A quarter-century of H-mode studies". In: *Plasma Physics and Controlled Fusion* (2007). DOI: https://iopscience.iop.org/article/10.1088/0741-3335/49/12B/S01.

[8] R.J.Goldston. "Heuristic drift-based model of the power scrape-off width in low-gas-puff H-mode tokamaks". In: *Nuclear Fusion* (2011). DOI: https://doi.org/10.1088/0029-5515/52/1/013009.

[9] O. Schmitz H. Frerichs F. Effenberg. "Synthetic plasma edge diagnostics for EMC3-EIRENE, highlighted for Wendelstein 7-X". In: *REVIEW OF SCIENTIFIC INSTRUMENTS* (2016). DOI: https://doi.org/10.1063/1.4959910.

[10] G.Z. Zuo T. Xie S.Y. Dai. "EMC3-EIRENE modelling of edge plasma and impurity emissions compared with the liquid lithium limiter experiment on EAST". In: *Nuclear Fusion* (2018). DOI: https://iopscience.iop.org/article/10.1088/1741-4326/aad42f/meta.

[11] J. Horacek J.G.A. Scholte J. Cecrdle. "Predictive and interpretative modelling of ASDEX-upgrade liquid metal divertor experiment". In: *Fusion Engineering and Design* (2023). DOI: https://doi.org/10.1016/j.fusengdes.2023.113886.

[12] D. Reiter. *The EIRENE Code User Manual*. Institut fur Energie- und Klimaforschung – Plasmaphysik ¨ Forschungszentrum Julich GmbH, 2023.

[13] Max Planck Institute. *ASDEX Upgrade*. URL: https://www.ipp.mpg.de/16195/asdex.

[14] Max Planck Institute. *ASDEX Upgrade*. URL: https://www.aug.ipp.mpg.de/wwwaug/documentation/physics/physics.shtml.

[15] J. Roth C. García-Rosales W. Eckstein. "Revised formulae for sputtering data". In: *Journal of Nuclear Materials* (August 1994). DOI: https://doi.org/10.1016/0022-3115(94)00376-9.

[16] J. Roth C. García-Rosales W. Eckstein. "Revised formulae for sputtering data". In: *Journal of Nuclear Materials* (August 1994). DOI: https://doi.org/10.1016/0022-3115(94)00376-9.

[17] V. Kotov S. Wiesen D. Reiter. "The new SOLPS-ITER code package". In: *Journal of Nuclear Materials* (August 2015). DOI: https://doi.org/10.1016/j.jnucmat.2014.10.012.